

Molecular Gas in HII Regions of M101

by

Jean Giannakopoulou Creighton

A thesis

presented to the University of Waterloo

in fulfilment of the

thesis requirement for the degree of

Doctor of Philosophy

in

Physics

Waterloo, Ontario, Canada. 1998

©Jean Giannakopoulou Creighton 1998



**National Library
of Canada**

**Acquisitions and
Bibliographic Services**

**395 Wellington Street
Ottawa ON K1A 0N4
Canada**

**Bibliothèque nationale
du Canada**

**Acquisitions et
services bibliographiques**

**395, rue Wellington
Ottawa ON K1A 0N4
Canada**

Your file Votre référence

Our file Notre référence

The author has granted a non-exclusive licence allowing the National Library of Canada to reproduce, loan, distribute or sell copies of this thesis in microform, paper or electronic formats.

The author retains ownership of the copyright in this thesis. Neither the thesis nor substantial extracts from it may be printed or otherwise reproduced without the author's permission.

L'auteur a accordé une licence non exclusive permettant à la Bibliothèque nationale du Canada de reproduire, prêter, distribuer ou vendre des copies de cette thèse sous la forme de microfiche/film, de reproduction sur papier ou sur format électronique.

L'auteur conserve la propriété du droit d'auteur qui protège cette thèse. Ni la thèse ni des extraits substantiels de celle-ci ne doivent être imprimés ou autrement reproduits sans son autorisation.

0-612-30597-X

The University of Waterloo requires the signatures of all persons using or photocopying this thesis. Please sign below, and give address and date.

Abstract

The molecular component of three giant H II regions (NGC 5461, NGC 5462, NGC 5471) and one normal H II region (H660) in the galaxy M101 are investigated with new observations from single dish telescopes (JCMT and NRAO 12-meter) and from the Owens Valley millimeter array. The data are analyzed using three independent methods to calculate the mass of the molecular gas in the H II regions.

The molecular mass for the *association* of clouds in NGC 5461 is approximately $10^8 \mathcal{M}_{\odot}$ and is accompanied by a few times more atomic mass. The observed CO emission in NGC 5461 was stronger than in NGC 5462 while it was not possible to detect molecular gas toward NGC 5471 with the JCMT. The fairly large ratio of atomic to molecular gas in NGC 5471 might be attributed to inefficient conversion of the atomic gas to giant molecular clouds.

The masses of the *individual* giant molecular clouds in NGC 5461, which are gravitationally bound, cover a range of $(10 - 40) \times 10^5 \mathcal{M}_{\odot}$ —an order of magnitude larger than Galactic giant molecular clouds. Massive clouds might be a prerequisite for the formation of the large number of stars whose radiation produces the giant H II regions. Furthermore, the giant molecular clouds in NGC 5461 are larger in size than expected given their small velocity dispersions. These small velocity dispersions indicate that collisions of smaller clouds are important for the formation of the large giant molecular clouds in NGC 5461.

Acknowledgements

I would like to thank my supervisor, Mike Fich, for his support and enthusiasm, and my external examiner Bill McCutcheon, who read my thesis with great care. All members of my committee have contributed in one way or another, but one person needs to be mentioned in particular: Gretchen Harris has been a wonderful mentor and a good friend.

It is my pleasure to thank Christine Wilson for her valuable input on all aspects of the observations, Robert Kennicutt for giving me his $H\alpha$ image of NGC 5461, Robert Braun for sending me his HI maps of M101, Jeff Kenney for sharing his unpublished CO map of M101, and Lorne Avery for encouraging me to use his large velocity gradient code.

I am grateful both to the National Research Council of Canada for supporting my several observing trips and to the Astronomy Department of the California Institute of Technology for providing the resources I needed to complete this thesis.

This work would not have been possible without the encouragement of my friends Anne Fullerton, Pat and George Moir and my family—especially my parents Judy and Βαγγελης and my husband Jolien.

Contents

1	Introduction	1
1.1	Giant H II Regions	4
1.2	Molecular Gas in Galaxies	8
1.2.1	Studies of Molecular Gas in the Milky Way	8
1.2.2	Studies of Molecular Gas in the Magellanic Clouds	13
1.2.3	Studies of Molecular Gas in M31	16
1.2.4	Studies of Molecular Gas in M33	17
1.3	The Spiral Galaxy M101	19
1.3.1	Distance to M101	19
1.3.2	Stars and Ionized Gas in M101	21
1.3.3	Atomic Gas in M101	24

1.3.4	Metallicities and Abundances	25
1.3.5	Molecular Gas in M101	26
1.4	Outline	28
2	Observations	30
2.1	Single Dish Line-Emission Data	31
2.1.1	James Clerk Maxwell Telescope (JCMT)	31
2.1.2	National Radio Observatory (NRAO) 12-meter	57
2.2	Interferometer Emission Data	60
2.2.1	Owens Valley Millimeter Array	60
2.3	Summary of Observations	89
3	Analysis	90
3.1	Calculating the Radiation Temperature	93
3.2	LTE Analysis	97
3.2.1	Optical Depth from LTE Method	97
3.2.2	Column Density from LTE Method	103
3.2.3	Mass from LTE Method	109

3.2.4	Results from LTE Method	110
3.3	Molecular Mass from the Empirical Method	119
3.3.1	Results from the Empirical Method	122
3.4	LVG analysis	127
3.4.1	Results from the LVG Method	130
3.5	Summary of Physical Properties	142
4	Discussion	145
4.1	Properties of the Molecular Gas	146
4.1.1	Masses and Temperatures	146
4.1.2	Size:line-width Relationship	151
4.1.3	Stability of the GMCs in NGC 5461	154
4.2	Star Formation	158
4.2.1	Role of the Cloud's Mass in Star-formation	158
4.2.2	CO Map Compared with the High-resolution H α Image	159
4.2.3	Molecular Gas Compared with Atomic Gas	161
4.2.4	Masses Derived from the IRAS Catalog	164
4.2.5	Star-formation Efficiency	166

5	Conclusions	168
5.1	Conclusions about the Molecular Associations in M101	170
5.2	Conclusions about the GMCs in NGC 5461	173
5.3	Future Directions	175
A	How to Calibrate Emission Line Observations	177

List of Figures

1.1	Map of nearby galaxies	3
1.2	Optical map of M101	20
2.1	Spectra of $^{12}\text{CO } J = 2 \rightarrow 1$ toward the first six positions in NGC 5461	39
2.2	Spectra of $^{12}\text{CO } J = 2 \rightarrow 1$ toward the remaining five positions in NGC 5461	40
2.3	Spectra of $^{12}\text{CO } J = 3 \rightarrow 2$ toward five positions in NGC 5461	42
2.4	Spectra of $^{12}\text{CO } J = 3 \rightarrow 2$ toward five positions in H660	44
2.5	Spectra of $^{12}\text{CO } J = 2 \rightarrow 1$ toward six positions in H660	47
2.6	Spectra of $^{12}\text{CO } J = 2 \rightarrow 1$ toward the first four positions in NGC 5462	51
2.7	Spectra of $^{12}\text{CO } J = 2 \rightarrow 1$ toward the remaining three positions in NGC 5462	52
2.8	Spectra of $^{12}\text{CO } J = 3 \rightarrow 2$ toward the first five positions in NGC 5462	53

2.9 Spectra of $^{12}\text{CO } J = 3 \rightarrow 2$ toward the remaining four positions in NGC 5462	54
2.10 Spectra of $^{13}\text{CO } J = 2 \rightarrow 1$ toward NGC 5461, NGC 5462, and H660	56
2.11 NRAO spectra of $^{12}\text{CO } J = 1 \rightarrow 0$ toward three giant H II regions .	58
2.12 The primary beam at Owens Valley during the observations of NGC 5461	62
2.13 The primary beam at Owens Valley during the observations of NGC 5462	63
2.14 Integrated Owens Valley map of NGC 5461 over 52 km s^{-1}	70
2.15 First four channel maps of NGC 5461	71
2.16 More channel maps of NGC 5461	72
2.17 More channel maps of NGC 5461	73
2.18 More channel maps of NGC 5461	74
2.19 Last four channel maps of NGC 5461	75
2.20 Optimum map of GMC 1 in NGC 5461	77
2.21 Optimum map of GMC 2 in NGC 5461	78
2.22 Optimum map of GMC 3 in NGC 5461	79
2.23 Optimum map of GMC 4 in NGC 5461	80
2.24 Optimum map of GMC 5 in NGC 5461	81

2.25	Optimum map of GMC 6 in NGC 5461	82
2.26	Optimum map of GMC 7 in NGC 5461	83
2.27	Optimum map of GMC 8 and GMC 9 in NGC 5461	84
2.28	Optimum map of GMC 10 in NGC 5461	85
2.29	Integrated map of NGC 5462 over 52 km s ⁻¹	88
3.1	The best kinetic temperature for NGC 5461 with $\psi = 20$	134
3.2	The best number density for NGC 5461 with $\psi = 20$	136
3.3	The best abundance, ζ , for NGC 5461 with $\psi = 20$	137
3.4	Density and abundance versus kinetic temperature for the gas in NGC 5461	141
4.1	Comparison of the molecular mass and the virial mass	157
4.2	Comparison of the CO with the H α map of NGC 5461	160
4.3	Comparison of the CO with the H I map of NGC 5461	163

List of Tables

1.1	Properties of several H II regions	5
1.2	Properties of GMCs	11
1.3	Properties of the GMCs in the LMC and the SMC	15
1.4	Positions of giant H II regions in M101	23
1.5	Masses of stars and ionized gas in the giant H II regions of M101	23
2.1	Summary of the JCMT observations	33
2.2	Positions of centres of all observed sources	34
2.3	Properties of the JCMT receivers	34
2.4	$^{12}\text{CO } J = 2 \rightarrow 1$ spectral line parameters for NGC 5461	38
2.5	$^{12}\text{CO } J = 3 \rightarrow 2$ spectral line parameters for NGC 5461	41
2.6	$^{12}\text{CO } J = 3 \rightarrow 2$ spectral line parameters for H660	45

2.7	$^{12}\text{CO } J = 2 \rightarrow 1$ spectral line parameters for H660	46
2.8	$^{12}\text{CO } J = 2 \rightarrow 1$ spectral line parameters for NGC 5462	49
2.9	$^{12}\text{CO } J = 3 \rightarrow 2$ spectral line parameters for NGC 5462	50
2.10	$^{13}\text{CO } J = 2 \rightarrow 1$ spectral line parameters of NGC 5461, NGC 5462, and H660	55
2.11	Quality of JCMT spectra	55
2.12	$^{12}\text{CO } J = 1 \rightarrow 0$ spectral line parameters for the NRAO data	57
2.13	Positions of the six Owens Valley antennas in the A configuration	61
2.14	Positions of the six Owens Valley antennas in the C configuration	61
2.15	Physical properties of GMCs in NGC 5461	86
3.1	Coupling efficiencies and uncertainties	95
3.2	LTE results for NGC 5461	112
3.3	LTE results for NGC 5462	113
3.4	LTE results for H660	114
3.5	LTE column densities and masses	117
3.6	Masses from empirical method	125

3.7	Molecular masses of individual GMCs in NGC 5461 calculated empirically	126
3.8	Radiation temperature ratios	132
3.9	The allowed physical parameters for NGC 5461 from the LVG analysis	140
3.10	Summary of masses obtained from the three methods in the analysis	144
4.1	Comparison of $^{12}\text{CO } J = 1 \rightarrow 0$ measurements in this thesis with those by Kenney et al. (1991)	148
4.2	Sizes and masses of GMCs in NGC 5461	153
4.3	Virial masses of GMCs	156
4.4	The infrared fluxes from the IRAS Point Source Catalog	165
4.5	Star-formation efficiencies for NGC 5461 and NGC 5471	167

Chapter 1

Introduction

The birth of a new star has a significant impact on the surrounding interstellar medium—for massive stars, the impact is even more pronounced. A massive young star is very hot, typically more than 20 000 K; therefore, most of its radiation is emitted in the ultraviolet part of the spectrum. Some of these photons will have wavelengths of less than the 91.2 nm required to ionize hydrogen from its ground state; these photons will be absorbed by the surrounding gas—primarily hydrogen—out to a considerable distance. This ionized region is called an H II region (the II indicates that the gas is ionized while H I denotes neutral atomic gas).

Because H II regions have different properties and morphologies, astronomers classify H II regions in six groups: ultra-compact, compact, dense, classical, giant, and supergiant (Habing and Israel, 1979). In recent years, ‘giant’ H II regions are called ‘diffuse’ (such as W49) while ‘supergiant’ regions are called simply ‘giant’:

this convention is followed in the present thesis.

Giant H II regions are the most spectacular star-forming regions in normal galaxies and have been the object of many studies. Especially impressive are the H II regions observed in the galaxy M101, which is a relatively nearby spiral galaxy (see Figure 1.1). What is special about the galaxy M101 that produces such bright H II regions? One hypothesis is that these regions result from the unusual properties of the molecular gas from which the stars that ionize the gas originate.

The purpose of this thesis is to collect data on the physical properties of the molecular gas in the giant H II regions of M101 and to find clues about the formation of giant H II regions.

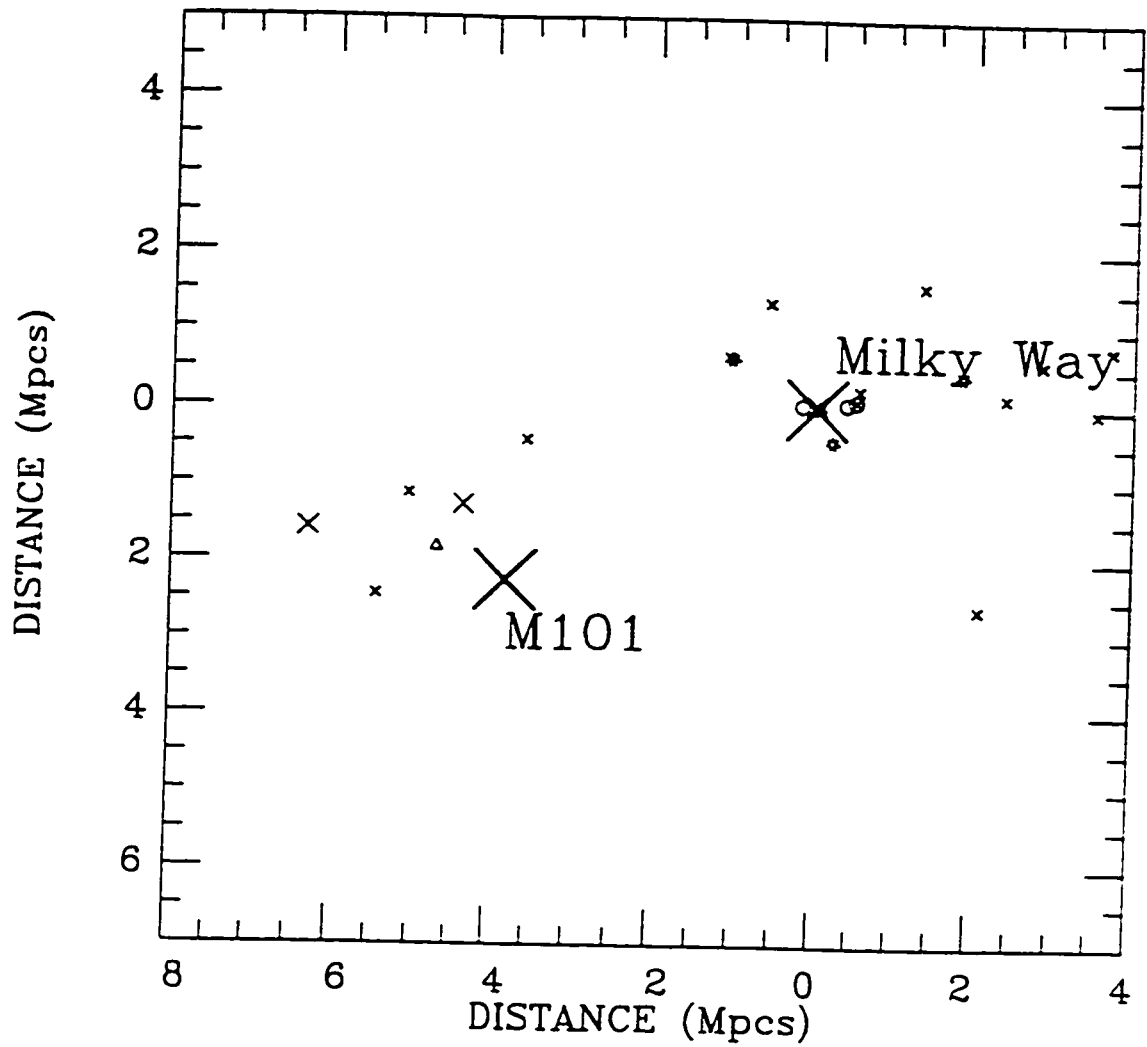


Figure 1.1: Map of nearby galaxies: the spiral galaxies are plotted as \times —the Milky Way is the large \times at the origin, and M101 is the large \times below it to the left. Elliptical galaxies are circles. S0 galaxies are indicated with open triangles and irregular galaxies with seven-pointed small stars.

1.1 Giant H II Regions

The class of giant H II regions consists of a very heterogeneous group of objects in terms of size and brightness. For comparison, Table 1.1 includes two H II regions in the Milky Way: Orion, which is a fairly ordinary H II region close to the Sun, and W49, the largest H II region in our Galaxy.¹ Even W49, however, pales in comparison to the giant H II regions in M101: W49 is two orders of magnitude smaller in area and two orders of magnitude fainter in absolute magnitude than NGC 5471, one of the giant H II regions in M101.² It is intriguing that the spiral galaxy M101, which is quite similar to the Milky Way, has H II regions that are so much larger and brighter than the largest one in our Galaxy.

The typical size of a giant H II region ranges from 100 parsecs (pc) to more than 500 pc.³ These objects are impressive not only due to their size: they are also extremely bright: the observed luminosity of the $n = 3 \rightarrow 2$ Balmer line of hydrogen ($H\alpha$ at 6563 \AA) is on the order of $10^{39} \text{ erg s}^{-1}$, which requires 10^{51} ionizing photons per second. Such an influx of ionizing photons suggests that hundreds of early type stars (O and B) must be nested in each giant H II region.

Over the past twenty years, the brightness of giant H II regions has facilitated

¹To distinguish objects in the Milky Way from objects in other galaxies, astronomers use the following convention: objects in the Milky Way are called *Galactic* whereas objects or issues that refer to other galaxies are named *galactic*.

²NGC stands for New General Catalogue of Nebulae and Star Clusters, which is a compilation of 7840 non-stellar objects.

³One parsec, $3.08 \times 10^{13} \text{ km}$, is the distance at which one Astronomical Unit, the distance between the Earth and the Sun, has a parallax of $1''$.

Object	Galaxy	Distance (kpc)	Diameter (pc)	N (O5V)
Orion	Milky Way	0.5	5	0.2
W49	Milky Way	15	150	27
30 Dor	Large Magellanic Cloud	50	370	230
N19	Small Magellanic Cloud	70	220	3
NGC 604	M33	800	400	65
NGC 5471	M101	7400	1000	750

Table 1.1: Properties of several H II regions from Shields (1990). The diameters listed were determined by visual inspection of optical images, so the values of the diameters might not be accurate—they are presented for comparison purposes. $N(O5V)$ is the number of main-sequence (V) bright stars of O5 type needed to produce the appropriate number of ionizing photons to reproduce the observed luminosity.

their study despite their great distances. Thus, giant H II regions have become important as: (i) signposts of star-formation, (ii) distance indicators, (iii) metallicity⁴ tracers, and (iv) tools to study the dynamics and spiral structure of galaxies. These four points are discussed in turn.

(i) Because giant H II regions are sites of extensive star formation, they are used to study large groups of massive young stars such as OB associations and star clusters. Typically, the observed total energy distribution of the stars is compared with theoretical energy distributions that depend to first order on the age and the mass distribution of the cluster [e.g., Rosa and Benvenuti (1994); Wilson and Matthews (1996); Bresolin et al. (1996)]. From the comparison, one can estimate the age and stellar mass distribution for a given cluster of stars.

(ii) Giant H II regions have been used as a standard candle (Sandage and Tammann, 1974) to determine distances (and ultimately, the Hubble constant) for objects farther than 4 Mpc, which was the observational cutoff for Cepheid variables⁵ until recently. Sandage and Tammann estimated extragalactic distances by measuring the size of the H II region and using their conclusion that the size depends on the type of galaxy. Since their study, there have been refinements of the method [see Shields (1990) and references therein]. However, the family of giant regions is probably more complicated than originally thought, and now there are better ways of determining extragalactic distances.

⁴The ratio of any element heavier than helium to hydrogen; some of these elements are not metals according to the chemical definition. The term might have originated from the fact that the lines of metals such as iron tend to dominate stellar spectra.

⁵Luminous pulsating variable stars that radiate ten thousand times as much energy as the Sun.

(iii) Giant H II regions are still used to measure abundances of various elements through their emission lines. These emission lines can be used to determine some of the physical properties of the ionized gas and how the metallicity changes within a galaxy and between galaxies (McCall et al., 1985). Such tracers of metallicity give clues for models of the chemical evolution of galaxies (Matteucci, 1986; Pagel, 1986).

(iv) Furthermore, the line-width of these emission lines yields kinematic information about the gas in the galaxy [see, e.g., Mihalas and Binney (1981)]. These data can be used to study the dynamics of galaxies.

Despite the importance of giant H II regions, astronomers still do not know how they form. What is special about the host galaxies of these regions? Kennicutt (1984), after an extensive study of the ionized gas, suggested that the *properties of the molecular component* of giant H II regions should be investigated because they might be a critical piece of the puzzle.

Molecular gas—as observed from carbon monoxide (CO) emission—has been found to be associated with H II region peaks in the Milky Way (Israel, 1980; Harris, 1980). During the past fifteen years, it has been possible to investigate the molecular gas in other galaxies as well. In the next section, I present a summary of the results of these investigations.

1.2 Molecular Gas in Galaxies

By far, the most abundant molecule in the universe is hydrogen. However, we cannot directly observe cold molecular hydrogen gas at large distances (Scoville and Sanders, 1987). Fortunately, CO—although 10 000 times less abundant than hydrogen—is easily excited by collisions with hydrogen and is readily observed through its rotational emission lines.

Some CO studies involve observations of individual molecular clouds that are known to be associated with star-forming regions (such as H II regions). These studies, however, could introduce biases in the properties of the molecular clouds because the results are based on particularly active regions. To avoid this bias, a number of investigators have been surveying large areas of the sky for CO emission in order to carry out unbiased statistical studies of molecular clouds.

1.2.1 Studies of Molecular Gas in the Milky Way

There have been several Galactic surveys of CO emission [for example, Dame et al. (1986), Scoville et al. (1987), Solomon et al. (1987), and Clemens et al. (1988)]. The mass of molecular gas in the Galaxy is comparable with that of atomic hydrogen (Clemens et al., 1988). Despite the fact that most molecular clouds have masses much lower than 5×10^4 solar masses⁶ (Blitz, 1993), 85% of the Galactic molecular gas is contained in a few massive molecular clouds that have masses larger than

⁶The mass of the Sun is 2×10^{33} g and is denoted by \mathcal{M}_{\odot} .

$10^5 \mathcal{M}_\odot$ and radii larger than 22 pc (Sanders et al., 1985). These massive molecular clouds are called giant molecular clouds (GMCs) and have well defined boundaries: their typical size is 45 pc (Blitz, 1993).

GMCs have pronounced boundaries (Blitz and Thaddeus, 1980; Dame et al., 1986), but their mass range is less well defined: their masses are typically defined as being larger than $10^5 \mathcal{M}_\odot$ (Stark and Blitz, 1978; Evans, 1986; Blitz, 1993). In order to calculate the mass of a GMC from just one CO emission line, one typically measures the integrated intensity of the CO line because there is a very consistent empirical correlation between the luminosity of CO emission and the mass of the molecular gas (Scoville et al., 1987; Solomon et al., 1987). This correlation reinforces the idea that CO emission is a good tracer of molecular gas: that is, the CO luminosity can be used directly to calculate the mass of molecular hydrogen. In particular, the integrated observed CO radiation temperature over the appropriate velocity range is multiplied by a single number called the X factor.

To calculate this factor, it is necessary to establish other ways of estimating the mass of the molecular gas. One method is to assume that the cloud is in virial equilibrium⁷ and determine the appropriate X factor that equates the mass from the CO luminosity and the virial mass. The reliability of the CO estimates of mass is questioned in areas of the galaxy with physical properties and metallicity different from the GMCs in the solar neighbourhood (for further discussions, see pages 15 and 119).

⁷The virial theorem states that the gravitational potential energy of a self-gravitating system is twice as much as the kinetic energy of the members of the system. From this theorem, one can calculate the mass of the system from its size and the average velocity of each member.

Despite the uncertainty in the X factor, it is still interesting to study the way the GMCs are distributed, by mass, in the Galaxy. The distribution of the masses of the Galactic GMCs can be expressed in terms of a truncated power law: the number of GMCs per mass interval decreases as the mass increases and, based on several CO surveys, there seems to be a real upper limit of $6 \times 10^6 \mathcal{M}_\odot$ in the masses of the GMCs, which might reflect some underlying physical limit imposed by a formation or a destruction mechanism (Williams and McKee, 1997).

There is also an intriguing feature of the *radial* distribution of the molecular gas in our Galaxy: a molecular ring is discernible between 4 and 7 kpc from the centre of the Milky Way (Sanders et al., 1985; Scoville et al., 1987). The radial distribution of the molecular gas in other Sc galaxies lacks this characteristic: other galaxies have column densities that decrease more uniformly with increasing galactocentric distance (Young and Scoville, 1991). The H I radial distribution in galaxies (including the Milky Way) does not show any increase at the position of the molecular ring either (Scoville and Sanders, 1987).

Although GMCs follow the same radial distribution, they do not necessarily delineate the spiral arms of a Galaxy equally well (Sanders et al., 1985; Dame et al., 1986; Scoville et al., 1987). For example, GMCs associated with H II regions follow the spiral pattern closely. Such behaviour is observed in M101 also.

Now that the distribution of GMCs has been discussed, the physical characteristics of an average GMC in the solar neighbourhood can be summarized (Table 1.2). These properties are similar to those found in the GMCs of the inner Galaxy. The

Property	Value
Mass	$(1 - 2) \times 10^5 \mathcal{M}_\odot$
Mean Diameter	45 pc
Projected surface area	$2.1 \times 10^3 \text{ pc}^2$
Volume	$9.6 \times 10^4 \text{ pc}^3$
Volume averaged $n(\text{H}_2)$	50 cm^{-3}
Mean column density $N(\text{H}_2)$	$(3 - 6) \times 10^{21} \text{ cm}^{-2}$
Local surface density	4 kpc^{-2}
Mean separation	500 pc

Table 1.2: Properties of GMCs in the solar neighbourhood (Blitz, 1993).

volume density quoted in Table 1.2 is an average value. Values for the density range from 10 cm^{-3} to 300 cm^{-3} —the latter value being the critical density necessary to observe the CO emission. Therefore, there must be regions with higher density within a sea of lower density gas. Many studies have shown that GMCs are not uniform objects: they display filamentary and clumpy structure, so locally the density will be several orders of magnitude higher than the average of a few $\times 10 \text{ cm}^{-3}$.

An interesting property of GMCs is that they display a *size:line-width relation* (Larson, 1981; Scoville et al., 1987; Solomon et al., 1987; Blitz, 1993). The line-width, ΔV , is usually defined as the full-width half-maximum (FWHM) of the emission line, and the width of the line reflects the velocity of the gas; as the internal motion of the gas increases, the width increases. It has been found that

in most galaxies as the radius, R , of the GMC increases, the width of the emission line increases according to

$$\Delta V \sim R^{0.5}. \quad (1.1)$$

In other words, the large GMCs tend to have large line widths. As will be discussed in Section 4.1.2, the molecular complexes in M101 do not conform to this tendency.

GMCs typically are gravitationally bound objects: i.e. their internal kinetic motion is not enough to overcome their gravitational potential (Scoville and Sanders, 1987; Young and Scoville, 1991). If the GMCs are bound, then the line-width ΔV will be given by

$$(\Delta V)^2 = \text{constant } M/R. \quad (1.2)$$

If equation (1.1) is replaced in equation (1.2), then the mass is proportional to R^2 : therefore, the two properties (i.e., the GMCs have a size:line-width relation and are bound) suggest that GMCs should have roughly the same column density (Larson, 1981; Blitz, 1993).

The observed velocity widths have some implications for the evolution of GMCs. Because these velocities widths do not change much with galactocentric distance, Blitz (1993) suggests that collisions of smaller clouds are probably not responsible for the formation of normal GMCs. Collisions could be important, however, in the formation of the *largest* GMCs ($10^6 \mathcal{M}_\odot$), where a correlation exists between higher velocity dispersions and smaller clouds at the same distance from the centre of the Galaxy. This correlation is found in the GMCs of NGC 5461 also (see Section 4.1.2) and is used to confirm that collisions are important in the formation of large GMCs.

Once the cloud is formed, star-formation starts rapidly. Of the many hundreds of GMCs observed, only the Maddalena-Thaddeus cloud does not show signs of star-forming activity (Blitz, 1993). Essentially, then, all GMCs are cradles of young stars. In fact, as the mass of the cloud increases, so does the probability of the presence of a O9.5 star in the cloud (Williams and McKee, 1997). Interestingly, the mass needed for a cloud to have a 50% chance of containing at least one O9.5 star is $10^5 \mathcal{M}_{\odot}$.

The young stars that form H II regions produce winds and shocks that disrupt the interstellar medium and that will, eventually, destroy the cloud. The lifetime of a cloud is $1 - 10 \times 10^7$ years (Larson, 1981; Blitz and Shu, 1980; Blitz, 1993; Williams and McKee, 1997). One example of a very old GMC in our Galaxy is the remnant GMCs near the Lac OB1 association (Blitz, 1993). Although many embedded sources have been found in the cloud, very little molecular gas has been detected. It is possible that the cloud is in the final stage of its evolution. Unlike this region, most H II regions that are discussed below are accompanied by large amounts of molecular gas.

1.2.2 Studies of Molecular Gas in the Magellanic Clouds

As equipment has improved in sensitivity and resolution, it has been possible to observe GMCs in two of the larger satellite galaxies of the Milky Way: the Large Magellanic Cloud (LMC) at 50 kpc (Rubio, 1997) and the Small Magellanic Cloud (SMC) at 63 kpc (Rubio, 1997). These two galaxies are of particular interest

because they have, as M101, considerably lower metallicity abundances than our Galaxy. The Magellanic clouds can be used, therefore, to determine the effects of metallicity on the properties of the molecular gas. Specifically, the metal abundance estimate for the LMC is 4 times less than the Galactic value (Rubio, 1997) while the difference is even more pronounced for the SMC: the metal abundance estimate is 10 times less than the Galactic abundance (Rubio et al., 1991).

There have been many studies of the molecular component in the LMC (Cohen et al., 1988; Johansson, 1991; Garay et al., 1993; Poglitsch et al., 1995; Rubio, 1997) and in the SMC (Rubio et al., 1991; Rubio et al., 1993a; Rubio et al., 1993b; Rubio, 1997). Table 1.3 summarizes the properties of the GMCs in the satellite galaxies of the Milky Way. The sizes of the GMCs are similar although the ones in the SMC tend to be smaller. Despite the fact that overall these structures are slightly smaller than GMCs seen in the Milky Way, the size:line-width relation is very similar among the GMCs in the three galaxies (Rubio, 1997; Johansson, 1991; Rubio, 1991). That is where the similarities end.

The CO emission from the Magellanic Clouds is significantly less than might be expected if one merely extrapolated from the GMCs in our Galaxy. For example, the peak antenna temperature for GMCs in the SMC is $T_A^* = 0.04K$, which is fifty times less than what would have been observed from an average Galactic cloud at the distance of the SMC (Rubio, 1991).

This apparent deficiency of CO is particularly intriguing when the presence of massive star-forming regions is taken into account. The LMC is the parent galaxy to

Property	SMC	LMC
Number of GMCs	12	86
Mean Diameter	(10 - 20) pc	(10 - 40) pc
Line widths	(1.6 - 4.9) km s ⁻¹	(2.5 - 10) km s ⁻¹
Mass	(2 - 9) × 10 ⁴ M _⊙	(0.1 - 70) × 10 ⁴ M _⊙

Table 1.3: Properties of the GMCs in the LMC and SMC (Rubio, 1997).

30 Doradus—the brightest, most impressive giant H II region in the Local Group of galaxies (see Table 1.1). The lack of substantial amounts of observed CO might be a sign that there is a true deficiency in the amount of molecular gas, which in turn could indicate that the rate at which stars are formed from the gas is particularly high. Alternatively, the small amounts of observed CO could be a result of the decreased metallicity and not an indicator of deficiency of molecular gas: the total molecular gas would be underestimated if it is calculated on the basis of the CO emission (Poglitsch et al., 1995). In this scenario, star-formation is not intense enough to cause the depletion of the molecular gas.

If the latter scenario is the correct one, then the value of the X factor would not be universal. Some unpublished Galactic data were used by Rubio (1991) to compare the X factor between the Magellanic Clouds and the Galaxy, where a canonical value for the Galaxy is assumed: $X_{Gal} = 2.3 \times 10^{20} \text{ cm}^{-2} (\text{K km s}^{-1})^{-1}$.

The spread of X values for the Magellanic Clouds spans a whole order of magnitude (Rubio, 1997). The SMC, for example, has an average value of $X = 4X_{Gal}$. Rubio suggests that these discrepancies among GMCs of the same approximate metallicity are probably due to differences in local properties.

Another important consideration is that the GMCs in our satellite galaxies appear to be highly fragmented (Rubio et al., 1993a; Poglitsch et al., 1995). The picture that emerges shows very small, dense, molecular clumps (1 pc) in otherwise mainly atomic gas. The UV radiation is very strong—especially in the vicinity of the giant H II region 30 Doradus in the LMC—and the molecular gas dissociates unless it is shielded in small dense clumps. It is believed that the deficiency in CO (over and above the decreased metallicity) in the Magellanic Clouds indicates that *there is a true deficiency in molecular hydrogen also*. The same conclusion is reached for the farthest giant H II region from the centre of M101, NGC 5471 (see page 149).

1.2.3 Studies of Molecular Gas in M31

M31, at a distance of 690 kpc (Dame et al., 1991), is another large spiral galaxy in our local group of galaxies. Observations of molecular gas in M31 are challenging because the surface density of the gas is very low; however, several individual GMCs in this galaxy have been investigated [Wilson and Rudolph (1993), Allen et al. (1995) and references therein]. These studies find that the GMCs in M31 are very similar in size to those in our Galaxy as regards the size:line-width relation.

An interesting point is that the virial masses of the GMCs in M31 are similar to the molecular masses, which indicates the conversion factor X of the molecular gas from the integrated intensity there is similar to that in the Milky Way.

There is one important difference between the GMCs in M31 and those of the Milky Way: the ratios of different transitions of CO in the latter have much lower values than in the former. Allen et al. (1995) explain this discrepancy by the fact that the GMCs in M31 are exposed to very low levels of UV radiation and, therefore, are probably extremely cold (≤ 5 K). The same authors also argue that the properties of the GMCs are probably more strongly connected to external parameters (such as UV radiation and cosmic rays) than to properties inherent to the galaxy (such as metallicity).

1.2.4 Studies of Molecular Gas in M33

M33 is a spiral galaxy at a distance of 840 kpc: this local group galaxy contains giant H II regions. Within the central 1 kpc of M33, there are large structures with a diameter of 200 to 400 pc and masses between $3 - 6 \times 10^6 \mathcal{M}_{\odot}$ (Wilson and Scoville, 1989). With high resolution observations, Wilson and Scoville (1990) identified 38 GMCs, 9 of which are resolved. The size:line-width relation of these GMCs agrees with that prevailing in the Milky Way (Wilson and Scoville, 1990).

Of particular interest in M33 are six GMCs (20 - 60 pc) identified near the giant H II regions NGC 604 and NGC 595 (Wilson and Scoville, 1992). The masses for these GMCs range between $0.5 - 4 \times 10^5 \mathcal{M}_{\odot}$, which is comparable to the masses of

Galactic GMCs. Other similarities that the GMCs in M33 and the Milky Way share are that they are gravitationally bound and that they have a similar X factor. The GMCs near the giant H II regions in M33, however, have *enhanced* star-formation efficiency (see Section 4.2.5), which could be the reason why giant H II regions can form from GMCs that are similar to those found in the Milky Way.

In addition to information about the masses and the star-forming efficiencies of the GMCs in M33, molecular studies provide information about the temperature of the GMCs also (Wilson et al., 1997): the GMCs that are not associated with an H II region are colder (10 – 20 K) while the ones nearest a giant H II region are hotter (> 100 K). Such hot GMCs are found in NGC 5461 also (page 130).

A specific cloud (NGC 604-2) near the giant H II region is particularly hot and it has a higher molecular-to-atomic ratio than NGC 595. Wilson and Matthews (1996) explain the differences between the GMCs near NGC 604 and those near NGC 595 using the hypothesis that NGC 595 is an older H II region in which there has been more photodissociation and, therefore, more molecular gas has been converted to atomic gas.

1.3 The Spiral Galaxy M101

The galaxy M101 is a large spiral galaxy that is quite impressive in optical images. Figure 1.2 shows the spiral structure of the galaxy. The bright giant H II regions are presented in more detail in the inserts.

1.3.1 Distance to M101

There have been many attempts to determine the distance to M101, because M101 is used to find the distance scale to even more remote galaxies and, ultimately, to estimate the Hubble constant [see for example Sandage and Tammann (1974), Sandage and Tammann (1976), and Kelson et al. (1996)]. Ideally, Cepheid variables would be used to establish the distance to M101 because they show a strong correlation between their absolute luminosity and their period of variability, which makes them reliable distance indicators. Until fairly recently (Cook et al., 1986), however, Cepheid stars could not be observed in a galaxy as distant as M101. Other methods had to be used.

These methods include group membership (Sandage and Tammann, 1974), the blue and red supergiants, which are the brightest stars of a galaxy (Humphreys and Strom, 1983; Sandage, 1983), the Tully-Fisher relationship (Pierce, 1994), and supernovae (Schmidt et al., 1992). The results have varied between 5 and 8 Mpc [de Vaucouleurs (1993), Kelson et al. (1996) and references therein]. The discrepancy can be resolved by fairly recent Hubble Space Telescope data, which revealed 29

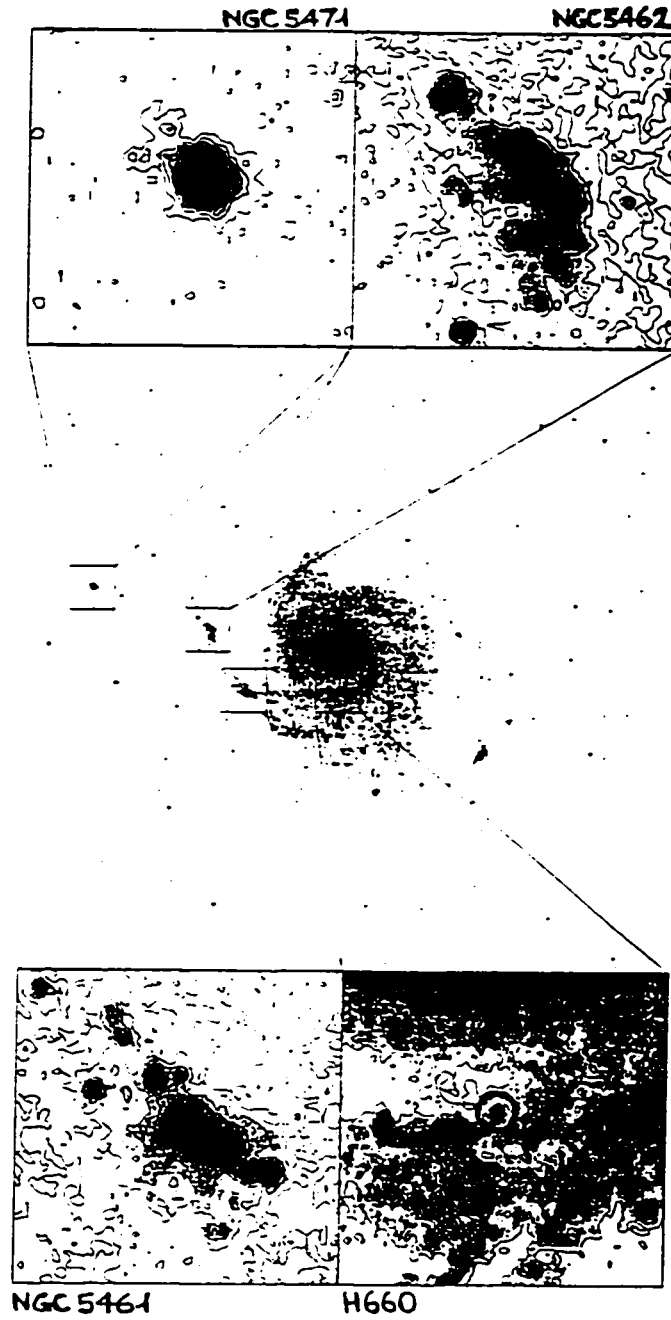


Figure 1.2: Large scale optical map of M101 with inserts of three giant H II regions and one normal H II region. The upper left insert is NGC 5471; the upper right insert is NGC 5462; and the lower left insert is NGC 5461. Because the lower right insert is crowded, a circle indicates H660. The squares are 2 kpc (1') on a side.

Cepheid variables in M101 (Kelson et al., 1996). In this recent study, a distance to M101 of 7.4 ± 0.6 Mpc is found, which is the distance adopted for this thesis.

1.3.2 Stars and Ionized Gas in M101

In the last 15 years, there have been many $H\alpha$ surveys of the H II regions in M101 [Hodge and Kennicutt (1983), Kennicutt (1984); Kennicutt (1988) to name but a few]. The latest, most comprehensive study (Hodge et al., 1990) suggests that there are 1264 H II regions in M101. Of these regions, five are considered giant H II regions: NGC 5447, NGC 5455, NGC 5461, NGC 5462, and NGC 5471, the positions of which are presented in Table 1.4.

For three of these giant H II regions, the mass of the ionized gas has been presented in Table 1.5: the uncertainties are a factor of a few because the mass of the ionized gas depends on the model adopted for the morphology of the H II region (Israel et al., 1975; Skillman, 1984). The ionized gas results from the interaction of the energetic photons that escape young massive stars with the interstellar medium. From recent studies of the spectra of the stars in NGC 5461 and NGC 5471, one can calculate that the stars occur in short bursts at 3 Myr intervals (Rosa and Benvenuti, 1994), and one can estimate the stellar mass in these H II regions (presented in Table 1.5). The stellar mass is important to calculate the star-forming efficiency of the region (see page 166).

To explain the presence of massive star-formation in the GMCs associated with the giant H II regions, Kenney et al. (1991) propose that either the initial mass

function⁸ is enhanced for massive stars, or the gas is consumed more efficiently in these regions. The first idea has been investigated (Rosa and Benvenuti, 1994): a study of four giant H II regions in M101 with a faint-object spectrometer on the Hubble Space Telescope concluded that the initial mass function for stars with masses larger than $2 M_{\odot}$ is similar to that in the Solar Neighbourhood. This result is consistent with more recent studies of OB associations in inner part of M101 (Bresolin et al., 1996). So there are indications that the first idea presented by Kenney et al. is not the answer to the brightness of the giant H II regions.

There has been no *conclusive* evidence yet that the gas consumption is enhanced either. There was an indication that the star-formation efficiency of massive stars in NGC 5461 is higher than the typical total star-formation efficiencies observed in our Galaxy (Blitz et al., 1981): however, the calculations of the stellar masses were rather crude and probably led to overestimating the masses of the stars. In Section 4.2.5, the star-formation efficiency is found to be *relatively small* compared to the efficiencies in star-forming regions of the Galaxy. The conclusion in this thesis is that higher star-formation efficiency is not the key to the formation of numerous massive stars—the key probably is that the masses of the GMCs in NGC 5461 are large (Section 4.2.1).

⁸The initial mass function describes the stellar distribution per unit mass per unit volume at the time of the formation of a cluster of stars. The initial mass function is often approximated by a power law of the form

$$\xi = \xi_0 m^{\Gamma}, \quad (1.3)$$

where Γ is the slope or index of the initial mass function.

Name	$\alpha(1950.0)$	$\delta(1950.0)$
NGC 5447	14 ^h 00 ^m 42 ^s .7	54°30'37"
NGC 5455	14 00 16.4	54 28 50
NGC 5461	14 01 56.0	54 33 26
NGC 5462	14 02 06.8	54 36 14
NGC 5471	14 02 43.5	54 38 09

Table 1.4: Optical positions of giant H II regions in M101 from Israel et al. (1975).

Name	Ionized mass ($\times 10^6 \mathcal{M}_{\odot}$)	Stellar mass ($\times 10^4 \mathcal{M}_{\odot}$)
NGC 5461	30	10
NGC 5462	58	N/A
NGC 5471	14	0.8

Table 1.5: Masses of the stars and the ionized gas in giant H II regions of M101: the mass of the ionized gas is from Israel et al. (1975), and the stellar mass is from Rosa and Benvenuti (1994).

1.3.3 Atomic Gas in M101

The atomic gas (H I), which is detected by the spin-spin transition at 1420 MHz, shows very similar morphology to that observed in H α images (Allen and Goss, 1979), but the H I emission is much more extended than the optical image (Huchtmeier and Witzler, 1979; Kamphuis, 1993). In particular, the surface density of H I increases for increasing galactocentric radius of up to 4' (9 kpc) from the centre of M101; between 4' and 12' (26 kpc) there is a plateau, the detailed structure of which depends on the azimuth of the position; finally, the surface density drops monotonically after 12' to become essentially zero at a distance of 24', which corresponds to a radius of approximately 53 kpc (Kamphuis, 1993).

The emission from the atomic gas is distributed almost equally between two components: first, the high brightness filamentary network of GMCs; and second, the diffuse interarm and outer disk component (Braun, 1995; Braun, 1997). Braun (1997) identifies the former component as the cool neutral medium (density $> 1 \text{ cm}^{-3}$ and temperature in the range of 50 – 250 K). A global characteristic of the H I is that the kinetic temperature rises from 80 K near the centre of M101 to 200 K near the edge of the H I distribution (Braun, 1995; Braun, 1997).

The atomic hydrogen is far from static. Kamphuis (1993) finds 52 'holes' in his H I map [see also Allen and Goss (1979)]—many of which are associated with H II regions. The most spectacular of these bubbles has a diameter of 1.5 kpc and an expansion velocity of 50 km s^{-1} (Kamphuis et al., 1991): no wonder these authors called the feature a 'superbubble'. The mass of its shell is $3 \times 10^7 \mathcal{M}_{\odot}$ while the

mass of the gas in the ‘hole’ is $2.5 \times 10^6 \mathcal{M}_\odot$. The energy required for the expansion to take place at its current rate is over 10^{53} ergs, which would be the energy from 1000 supernovae or from the merger of two neutron stars. This energy requirement is not unreasonable given the proximity of the superbubble to one of M101’s giant H II regions, NGC 5462. It is possible that there are enough young massive stars in the region to pour vast amounts of energy into the neighbouring interstellar medium.

Other giant H II regions have greater atomic masses. NGC 5461 and NGC 5471 have been measured with high resolution data: their atomic masses in a $6''$ beam are $5 \times 10^7 \mathcal{M}_\odot$ and $4 \times 10^7 \mathcal{M}_\odot$ respectively (Braun, 1995). The measurement of the atomic mass of NGC 5471 is consistent with an older measurement for the entire region: $(60 \pm 14) \times 10^6 \mathcal{M}_\odot$ of atomic gas (Skillman, 1984). A comparison between the atomic gas and the new map of the molecular gas is presented in Section 4.2.3.

1.3.4 Metallicities and Abundances

The electron density, He/H, O/H, and N/H abundances decrease with galactocentric distance (Rayo et al., 1982; Torres-Peimbert et al., 1989; Garnett and Kennicutt, 1994). Such gradients are found in our Galaxy too (Shaver et al., 1983). Evans (1986) finds that different elements have different slopes and suggests that these dissimilarities are due to differences in the evolution of the disk of the Galaxy. Garnett and Kennicutt (1994) find that the O/H ratio of an H II region in the outer disk of M101 is 10 times lower than that in the solar system. The difference

in metallicity might be important in calculating the molecular mass correctly (see page 119).

1.3.5 Molecular Gas in M101

The total mass of the molecular gas in M101 is $3.8 \times 10^9 \mathcal{M}_{\odot}$ (Kenney et al., 1991), which is consistent with an earlier estimate of $3 \times 10^9 \mathcal{M}_{\odot}$ for M101 up to a galactocentric radius of 12 kpc (Solomon et al., 1983). The first published CO survey of M101 (Solomon et al., 1983) suggested that the intensity of the CO emission decreases with increasing radius; again this conclusion is in agreement with a more recent survey of higher quality (Kenney et al., 1991). The azimuthally averaged CO intensity can be accurately described as an exponential fall-off with a scale length of $1'.95$ or 4.2 kpc (Kenney et al., 1991). This distribution can be contrasted with the distribution of the atomic gas: H I is scarce within the inner 6 kpc of the galaxy, rises to a plateau, and then declines with galactocentric distance (see page 24). Therefore, the molecular surface density peaks where there is very little atomic gas.

Another result of these gas distribution surveys is that the GMCs in the outer part of M101 have a high fraction of their mass in atomic form [see also Kenney et al. (1991)]. These authors also noted that the sum of the atomic and molecular gas is better correlated with $H\alpha$ —a tracer of massive star formation—than molecular hydrogen gas alone.

Although the azimuthally averaged CO intensity closely follows an exponential

decay with increasing distance from the centre of M101, the intensity of CO at a given distance but at different *azimuthal* directions can vary by a factor of 3. Kenney et al. (1991) find that there is a bar of molecular gas—2' in length—in the central region of M101. These authors note a 25° offset between the gas bar and the stellar bar. From the end of the CO bar, there is a weak spiral pattern seen in CO that meets the optical spiral pattern.

1.4 Outline

Chapter 2 contains the observations. I observed three giant H II regions and one normal H II region in M101. NGC 5461 is the protagonist: the molecular gas of this giant H II region was studied in most detail. Just to the north of NGC 5461 lies NGC 5462, which is not as bright in CO as NGC 5461. NGC 5471 is the farthest H II region from the center that was examined, and it is very dim in CO. Finally, I observed toward H660, a normal H II region⁹ very near the center of the galaxy. The observations are presented in three parts: the data from single-dish observatories in Section 2.1; in Section 2.2, the interferometric data, which have a higher resolution than the single-dish observations; finally, a summary of all the data can be found on page 89.

After the observations are presented, the analysis follows in Chapter 3. There are three methods used to find the masses of the thoroughly studied NGC 5461. The first involves the single dish data from the JCMT and is based on the LTE (local thermodynamic equilibrium) assumption (Section 3.2); the second assumes an empirical result for the relationship between the observed CO emission and the mass of the molecular gas (Section 3.3) and uses the $^{12}\text{CO } J = 1 \rightarrow 0$ line from the NRAO 12-meter telescope and the Owens Valley millimeter array; and the third involves using all the available data and the LVG (large velocity gradient) assumption (Section 3.4). These three methods are compared and summarized at the end of Chapter 3.

⁹The name used for the normal region reflects the fact that it is the 660th entry in the Hodge et al. (1990) catalog of H II regions in M101.

In Chapter 4, both the physical properties of the *associations* of GMCs in the H II regions of M101 and the characteristics of the *individual* GMCs in NGC 5461 are discussed. After the properties of the molecular gas have been presented, the effect of the star-forming process on the interstellar medium in M101 is discussed based on comparisons of the molecular gas with other investigators' studies of the atomic and ionized component of NGC 5461.

The conclusions are summarized in Chapter 5 and, finally, a detailed discussion of the calibration of single-dish millimeter data is contained in an Appendix to the thesis that begins on page 177.

Chapter 2

Observations

The data for this work are presented in two sections. Section 2.1 describes the single-dish data from the James Clerk Maxwell Telescope¹ (JCMT) and the National Radio Observatory (NRAO) 12-meter telescope. With these telescopes, I obtained low resolution data of three rotational transitions of ^{12}CO and one of ^{13}CO . Higher resolution data of the $^{12}\text{CO } J = 1 \rightarrow 0$ emission line from the Owens Valley millimeter array are presented in section 2.2. Because the chapter includes a large amount of detail, an overview of the observations is presented in section 2.3.

¹The JCMT is operated by the Joint Astronomy Centre in Hilo, Hawaii on behalf of the parent organizations Particle Physics and Astronomy Research Council in the United Kingdom, the National Research Council of Canada, and The Netherlands Organization for Scientific Research.

2.1 Single Dish Line-Emission Data

2.1.1 James Clerk Maxwell Telescope (JCMT)

Table 2.1 lists the observing runs at the 15-meter JCMT in a two-year period between January 1995 and February 1997 that were necessary to obtain all the required data for three giant H II regions and one isolated normal H II region in M101. The three giant H II regions—NGC 5461, NGC 5471, and NGC 5462—were chosen because they are the brightest regions in M101 while the normal H II region—H660—was chosen for comparison to the giants because it is isolated and has been detected in a recent CO map (unpublished, Kenney et al.). Each region was observed in several frequencies—in some cases, toward more than one position.

Table 2.2 lists the co-ordinates of each region's centre in terms of right ascension and declination (1950 co-ordinates). In addition to the positions of the H II regions, Table 2.2 contains the radial velocities of the observed regions in M101. All velocities in this thesis are given in the Local Standard of Rest (LSR) reference frame in which the average velocity of the stars in the vicinity of the Sun is zero. This frame of reference, which is commonly used, is assumed to be moving in a circular orbit on the plane of the Galaxy around the Galactic centre (Mihalas and Binney, 1981).

Since the position and velocity of the sources have been listed, the characteristics of the receivers will be discussed. Three receivers were used at the JCMT: A2, B3i and B3. These receivers have different resolutions, which are measured

by the full-width at half-maximum (FWHM) of the beam in Table 2.3. Among the characteristics that appear in Table 2.3 is the typical *system temperature*, T_{sys} , which can vary according to the weather and condition of the receiver. The system temperature is the effective noise temperature of the receiver when losses in the receiver, the atmosphere, and the telescope are taken into account. Another characteristic quantity that is presented in Table 2.3 is the *forward spillover and scattering efficiency*, η_{fss} , which is a correction for the radiation lost due to forward scattering and spillover (this efficiency is defined in the Appendix on page 183).

All observations were done in a position-switching mode in which the telescope is alternatively switched between the source and a nearby reference position with no emission. For these observations, it was necessary to use a position 3' away from the sources (and away from the centre of M101 to avoid possible contamination from other sources of CO) because M101 is an extended galaxy. The observations were obtained with the Dutch Autocorrelation Spectrometer (DAS).

Before the discussion of the JCMT observations of each H II region, there are some general remarks that apply for all of these observations. The observations consist of spectral lines, which are plotted in Figures 2.1 to 2.10, and plot a measure of the intensity of the line over velocity. The intensities are measured in corrected antenna temperatures, T_A^* (see page 180).

The central positions of the giant H II regions are labelled *a* to distinguish them from offset positions from the centre, which will be called *b*, *c* etc; similarly, the central position of the normal H II region H660 is labelled H1 to distinguish it from

Date	Source	Transition	Number of positions	Comments
Jan 1995	NGC 5461	$^{12}\text{CO } J = 2 \rightarrow 1$	11	Strong signal
	NGC 5461	$^{12}\text{CO } J = 3 \rightarrow 2$	5	Strong signal
	NGC 5461	$^{13}\text{CO } J = 2 \rightarrow 1$	1	Weak signal
	NGC 5461	$^{13}\text{CO } J = 3 \rightarrow 2$	1	No signal
Jan 1996				No data
April 1996	H660	$^{12}\text{CO } J = 3 \rightarrow 2$	5	Strong signal
May 1996	NGC 5461	$^{12}\text{CO } J = 2 \rightarrow 1$	1	Test for consistency
	NGC 5471	$^{12}\text{CO } J = 2 \rightarrow 1$	5	No signal
	H660	$^{12}\text{CO } J = 2 \rightarrow 1$	5	Signal detected
Feb 1997	NGC 5461	$^{13}\text{CO } J = 2 \rightarrow 1$	1	Signal detected
	NGC 5462	$^{12}\text{CO } J = 2 \rightarrow 1$	7	Position <i>g</i> is strongest
	NGC 5462	$^{13}\text{CO } J = 2 \rightarrow 1$	1	Upper limit
	NGC 5462	$^{12}\text{CO } J = 3 \rightarrow 2$	9	Six detections
	H660	$^{13}\text{CO } J = 2 \rightarrow 1$	1	Signal detected

Table 2.1: Summary of all the observing runs for this project at the JCMT from January 1995 to February 1997: for each run, one can see the number of positions observed in each frequency for each source. The last column includes some comments about the data.

Source	α (1950)	δ (1950)	V_{LSR} (km s ⁻¹)
NGC 5461	14 ^h 01 ^m 55. ^s 6	+54°33'31".0	275
NGC 5462	14 02 07.6	+54 36 17.4	300
NGC 5471	14 02 43.5	+54 38 09.0	290
H660	14 01 26.3	+54 33 30.0	220

Table 2.2: The positions of centres of all observed sources are given in right ascension, α , and declination, δ . The velocities of the H II regions are given in the local standard of rest reference—the reference frame in which the average velocity of the stars in the solar neighbourhood is zero.

Receiver	Frequency range (GHz)	Beam size FWHM (")	Transitions	η_{fss}	Typical T_{sys} (K)
A2	208-280	20	¹² CO $J = 2 \rightarrow 1$ ¹³ CO $J = 2 \rightarrow 1$	0.80	300-400
B3i	300-380	14	¹² CO $J = 3 \rightarrow 2$ ¹³ CO $J = 3 \rightarrow 2$	0.70	800-1000
B3	328-361	13	¹² CO $J = 3 \rightarrow 2$ ¹³ CO $J = 3 \rightarrow 2$	0.75	400-600

Table 2.3: Characteristic properties of the JCMT receivers used. Note that B3i and B3 operate in the same range of frequencies approximately, but B3 has better performance and has recently replaced B3i. The forward spillover and scattering efficiency, η_{fss} , is defined in the Appendix, page 183.

offset positions from the centre of H660, which will be called H2, H3 etc. Each off-centre position is defined by the offset in right ascension (") and declination (") from the centre of the H II region, the position of which is given in the caption: positive right ascension, α , is toward the east, and positive declination, δ , is toward the north.

The spectra in Figures 2.1 to 2.10 are calibrated. To calibrate the data, I used the SPECX package, which is a spectral line data reduction package written by Rachael Padman (Cavendish Laboratory, Cambridge, U.K.) for JCMT data. Linear baselines were removed after all the scans of the same position were averaged. The data were binned to a frequency resolution of 5 MHz (which corresponds to 6.50 km s⁻¹ at 230 GHz and to 4.35 km s⁻¹ at 345 GHz) to achieve satisfactory noise levels.

Tables 2.4 to 2.10 present the observed integrated antenna temperature, $\int T_A^* dv$, where v is the velocity range of the spectrum, for the various positions of each H II region. The observation points are again given by some offset in right ascension and declination from the centre of each H II region. In addition, Tables 2.4 – 2.10 list the three parameters obtained from a Gaussian fit to each of the spectra: the parameter, V_{peak} , is the velocity for which the antenna temperature obtains its maximum value, T_{peak} ; the parameter, ΔV , is calculated as the velocity width for an antenna temperature equal to half the maximum value. These velocity widths are large as was pointed out by Skillman and Balick (1984).

Experimentation with the ranges of integration, the binning, and the baselines

showed that the final value of the measured integrated intensity, $\int T_A^* dv$, is not sensitive to any of these parameters for all but the weakest lines. The uncertainties for each measurement of the measured line strength have been included in Tables 2.4 to 2.10. These experiments also indicated that the line width and the central velocity are not uncertain to more than a few percent. In the situations where the signal-to-noise ratio is low, I estimated an upper limit for the integrated intensity by choosing a velocity interval around the central velocity that maximizes the value of the integrated intensity.

The rms measuring uncertainties for the *peak temperature*, T_{peak} , quoted in these Tables (2.4 to 2.10) are those calculated given the integration times and the system temperatures: the rms noise of the peak temperature reported in the fourth column is for the smoothed data. Typical values for the uncertainty in the peak temperature range between 7 - 25 mK for ^{12}CO and 2.5 - 4 mK for ^{13}CO .

To facilitate the evaluation of quality of the data and their uncertainties, Table 2.11 has been included: for each range of relative uncertainty of the peak antenna temperature, this table specifies the fraction of the data with the corresponding uncertainty range. For example, 25% of the observations have a relative uncertainty in the peak of the antenna temperature between 11% - 20%. Overall, the quality is considered satisfactory since 78% of the data have signals at least 3 times stronger than the rms uncertainty. This low relative uncertainty is even more impressive if the weak signals are considered.

In addition to the random uncertainties, it is possible that there are system-

atic uncertainties. To check for systematic differences among observing sessions, I compared the data from different runs for positions where there are spectra with a high signal-to-noise ratio, for example, a calibrator or NGC 5461. If there are no fluctuations of the source, then the emission line from a calibrator should be constant in time. The discrepancies in flux among observing sessions have been as high as 25%, so there could be a systematic error of 25% in some cases that is introduced from the flux calibration.

After this general overview, the individual observing runs will be described now in greater detail. During the first observing run, NGC 5461 was mapped in two transitions ($^{12}\text{CO } J = 2 \rightarrow 1$ and $^{12}\text{CO } J = 3 \rightarrow 2$), and an attempt was made to do the same for those two transitions of ^{13}CO —a rarer isotopimer. $^{13}\text{CO } J = 2 \rightarrow 1$ and $^{13}\text{CO } J = 3 \rightarrow 2$ require a combination of excellent weather conditions and receivers with low noise because the ^{13}CO signal from a source is reduced typically by almost an order of magnitude compared to transitions of ^{12}CO .

I started mapping NGC 5461 with the common-user receiver A2 in the $^{12}\text{CO } J = 2 \rightarrow 1$ (230 GHz) line because the system temperatures are lower for that frequency (typically 400 – 450 K). The spacing between observed points was half a beam—approximately $10''$. This distance was achieved by observing points on a grid, which has cells of five points: the four corners of a square with sides of $14''$, and the central point. The corner point b (7,7), for example, is $\sqrt{7^2 + 7^2} = 10''$ away for the nearest point, the centre.

Integration times were 30 minutes with the exception of the central point, a ,

Source	$\Delta\alpha$ (")	$\Delta\delta$ (")	$\int T_A^* dv$ (K km s ⁻¹)	V_{peak} (km s ⁻¹)	ΔV (km s ⁻¹)	T_{peak} (mK)	Integration time (sec)
NGC 5461a	0	0	5.79 ± 0.3	275.7	23.7	228 ± 11	3000
NGC 5461b	7	7	5.39 ± 0.3	276.8	23.8	206 ± 11	1800
NGC 5461c	-7	-7	5.29 ± 0.3	272.8	24.0	207 ± 10	1800
NGC 5461d	-7	7	4.65 ± 0.4	275.0	23.4	181 ± 11	1800
NGC 5461e	7	-7	2.06 ± 0.4	273.3	23.9	83 ± 9	1800
NGC 5461f	-14	-14	5.63 ± 0.3	272.3	24.5	212 ± 11	1650
NGC 5461g	14	14	3.54 ± 0.4	286.8	22.0	158 ± 12	1800
NGC 5461h	-14	0	5.89 ± 0.3	273.9	25.8	217 ± 9	1800
NGC 5461i	14	0	1.71 ± 0.4	277.1	24.8	68 ± 10	1800
NGC 5461j	0	14	1.47 ± 0.4	280.0	16.5	79 ± 10	1800
NGC 5461k	0	-14	5.25 ± 0.3	271.9	24.2	202 ± 11	1800

Table 2.4: ¹²CO $J = 2 \rightarrow 1$ spectral line parameters for NGC 5461. The offsets are with respect to the centre of NGC 5461: $\alpha = 14^{\text{h}}01^{\text{m}}55^{\text{s}}.6$ and $\delta = 54^{\circ}33'31''.0$. The quantity $\int T_A^* dv$ is the integrated antenna temperature. The full-width at half-maximum, ΔV , and the central velocity, V_{peak} , for which the maximum antenna temperature value, T_{peak} , occurred were calculated by fitting Gaussian lines to the spectra.

which was integrated for 50 minutes to compensate for the higher system temperatures (560 K) at the time the observation was made. CO emission was detected at the seven sigma level or better toward all eleven points around NGC 5461, the brightest H II region in M101 (Figure 2.1 and 2.2). The peak antenna temperatures ranged between 68 and 228 mK (Table 2.4).

Interestingly, the ¹²CO $J = 3 \rightarrow 2$ (345 GHz) emission from four (*a, b, c, e*) out of the five central points of NGC 5461 observed was between 65 - 100% as strong as the emission seen in the ¹²CO $J = 2 \rightarrow 1$ spectra (Table 2.5 and Figure 2.3). The integration times were 50 minutes for the *b, c, d,* and *e* positions, and for

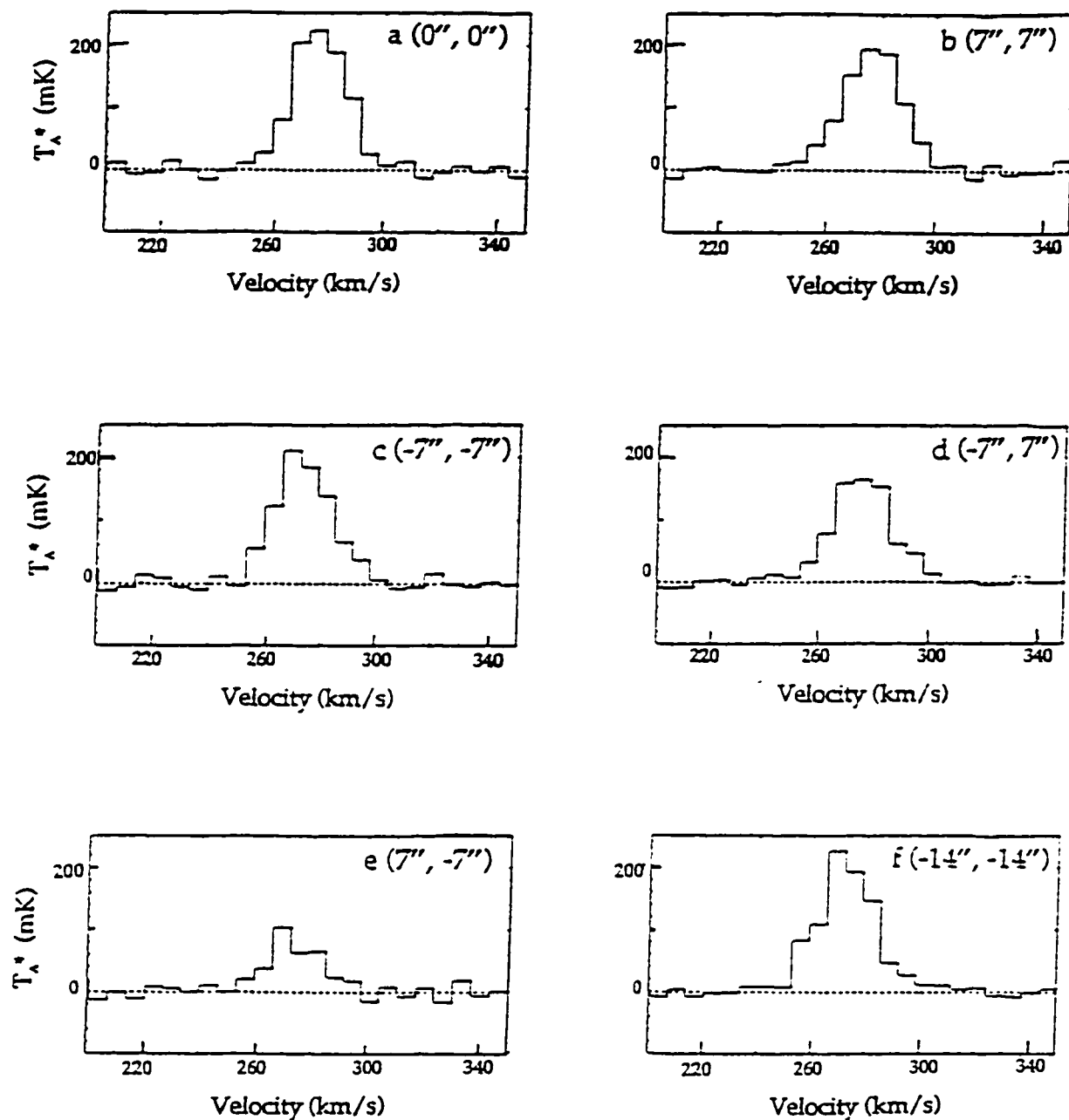


Figure 2.1: Spectra of $^{12}\text{CO } J = 2 \rightarrow 1$ toward the first six positions in NGC 5461. The offsets, which are indicated in the upper right corner of each spectrum, are with respect to the centre of NGC 5461: $\alpha = 14^{\text{h}}01^{\text{m}}55^{\text{s}}.6$ and $\delta = 54^{\circ}33'31''.0$.

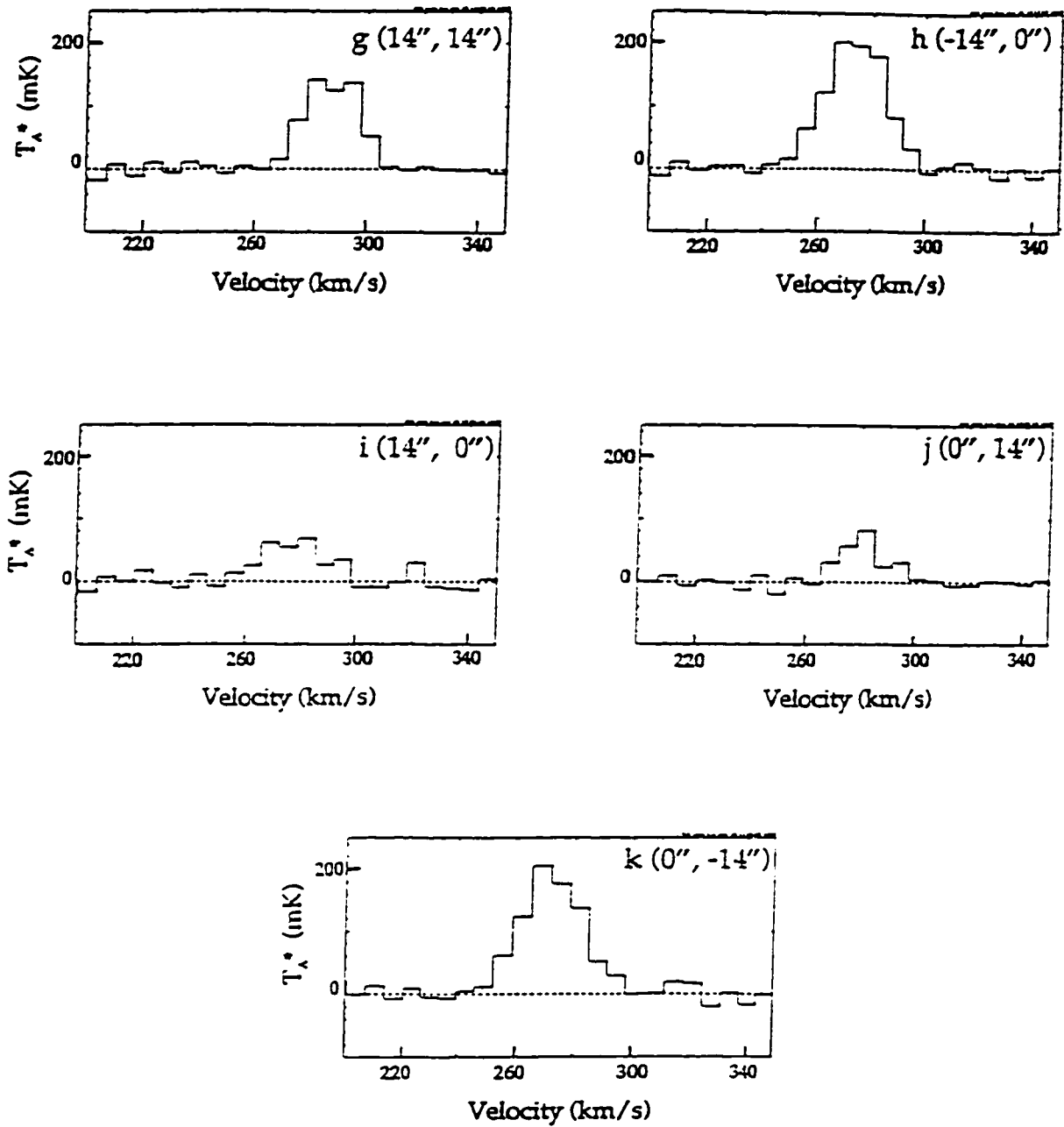


Figure 2.2: Spectra of $^{12}\text{CO } J=2 \rightarrow 1$ toward the remaining five positions in NGC 5461. The offsets, which are indicated in the upper right corner of each spectrum, are with respect to the centre of NGC 5461: $\alpha = 14^{\text{h}}01^{\text{m}}55^{\text{s}}.6$ and $\delta = 54^{\circ}33'31''.0$.

Source	$\Delta\alpha$ (")	$\Delta\delta$ (")	$\int T_A^* dv$ (K km s ⁻¹)	V_{peak} (km s ⁻¹)	ΔV (km s ⁻¹)	T_{peak} (mK)	Integration time (sec)
NGC 5461a	0	0	4.05 ± 0.2	276.52	22.59	180 ± 12	7200
NGC 5461b	7	7	3.27 ± 0.3	280.76	20.43	140 ± 15	3000
NGC 5461c	-7	-7	5.71 ± 0.2	274.62	26.93	210 ± 17	3000
NGC 5461d	-7	7	1.06 ± 0.3	276.00	17.59	51 ± 18	3000
NGC 5461e	7	-7	1.09 ± 0.3	270.61	18.30	53 ± 24	3000

Table 2.5: ¹²CO $J = 3 \rightarrow 2$ spectral line parameters for NGC 5461. The offsets are with respect to the centre of NGC 5461: $\alpha = 14^{\text{h}}01^{\text{m}}55^{\text{s}}.6$ and $\delta = 54^{\circ}33'31''.0$. The quantity $\int T_A^* dv$ is the integrated antenna temperature. The full-width at half-maximum, ΔV , and the central velocity, V_{peak} , for which the maximum antenna temperature value, T_{peak} , occurred were calculated by fitting Gaussian lines to the spectra.

the a position the integration time was 110 minutes (typical system temperatures were 850 – 1050 K). For these observations, I used the common-user receiver B3i, the characteristics of which are set out in Table 2.3. A spacing of 10" was used again. The tabulated rms noise values vary because of the fluctuations in the system temperature between 820 and 1300 K.

I also tried, with less success, to observe toward NGC 5461a two emission lines, $J = 2 \rightarrow 1$ and $J = 3 \rightarrow 2$, of the rarer isotopimer, ¹³CO. The latter transition was not detected, but I obtained a very weak detection for the former during this run. For ¹³CO $J = 2 \rightarrow 1$, the system temperature was 430 K, and I integrated for 100 minutes. The system temperature was much higher for ¹³CO $J = 3 \rightarrow 2$ (2000 – 3000 K); therefore, I could not integrate long enough within the time limitations to reduce the noise to acceptable levels. The noise level was as high as

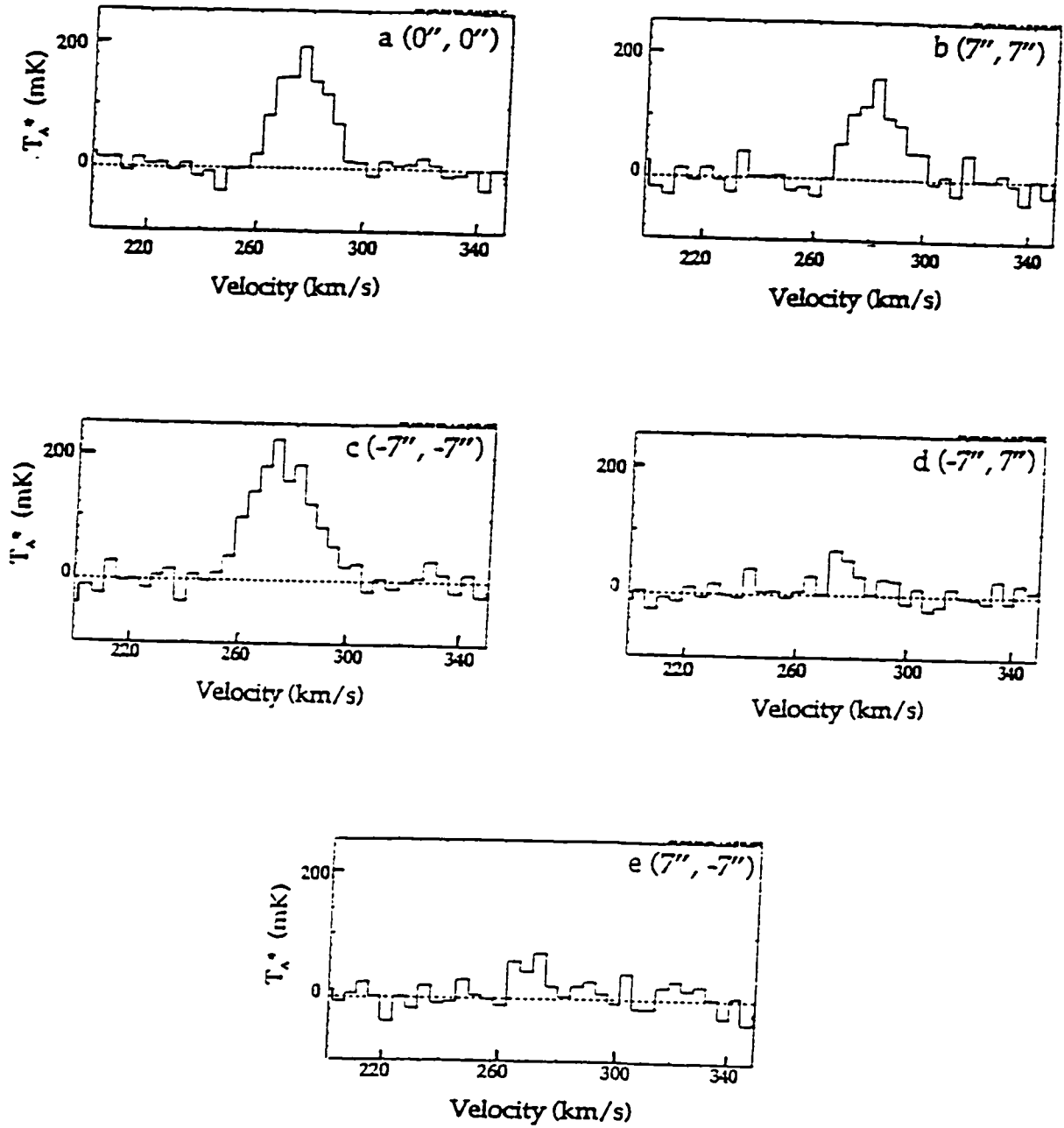


Figure 2.3: Spectra of $^{12}\text{CO } J=3 \rightarrow 2$ toward five positions in NGC 5461. The offsets, which are indicated in the upper right corner of each spectrum, are with respect to the centre of NGC 5461: $\alpha = 14^{\text{h}}01^{\text{m}}55^{\text{s}}.6$ and $\delta = 54^{\circ}33'31''.0$.

the expected signal (25 mK), so I abandoned this measurement. Although I did not get a better measurement of the $^{13}\text{CO } J = 3 \rightarrow 2$ line. I did improve the $^{13}\text{CO } J = 2 \rightarrow 1$ result during a subsequent observing run in February of 1997.

In January 1996, my allocated two-and-a-half shifts (20 hours) were unusable due to a snow storm at the observatory. Fortunately, Christine Wilson² had better luck in April 1996 when she observed $^{12}\text{CO } J = 3 \rightarrow 2$ for me toward H660, the normal H II region near the centre of M101. The system temperatures ranged over the two days between 900 - 1200 K, and the spacing used was 8"—as it was for all following JCMT observations. As can be seen from Table 2.6, the detections are real: four sigma or better (see also Figure 2.4). For the normal H II region, numbers are used to designate the offsets to distinguish them from the offsets of the giant H II regions (for which lower case roman letters are used).

During two more shifts in May 1996, I obtained $^{12}\text{CO } J = 2 \rightarrow 1$ data toward NGC 5471 and H660. To my surprise, there was no detection of CO toward NGC 5471—one of the brightest H II regions in M101. To calculate an upper limit for the integrated intensity from the five positions, I added the positive integrated intensities only and neglected the negative integrated intensities of the two positions. The upper limit derived this way for NGC 5471 is 0.70 K km s^{-1} integrated over 40 km s^{-1} .

Despite the non-detection of gas toward NGC 5471, the run was successful overall. I mapped H660 in $^{12}\text{CO } J = 2 \rightarrow 1$ emission and detected a signal toward all

²Faculty member of the Physics Department at McMaster University

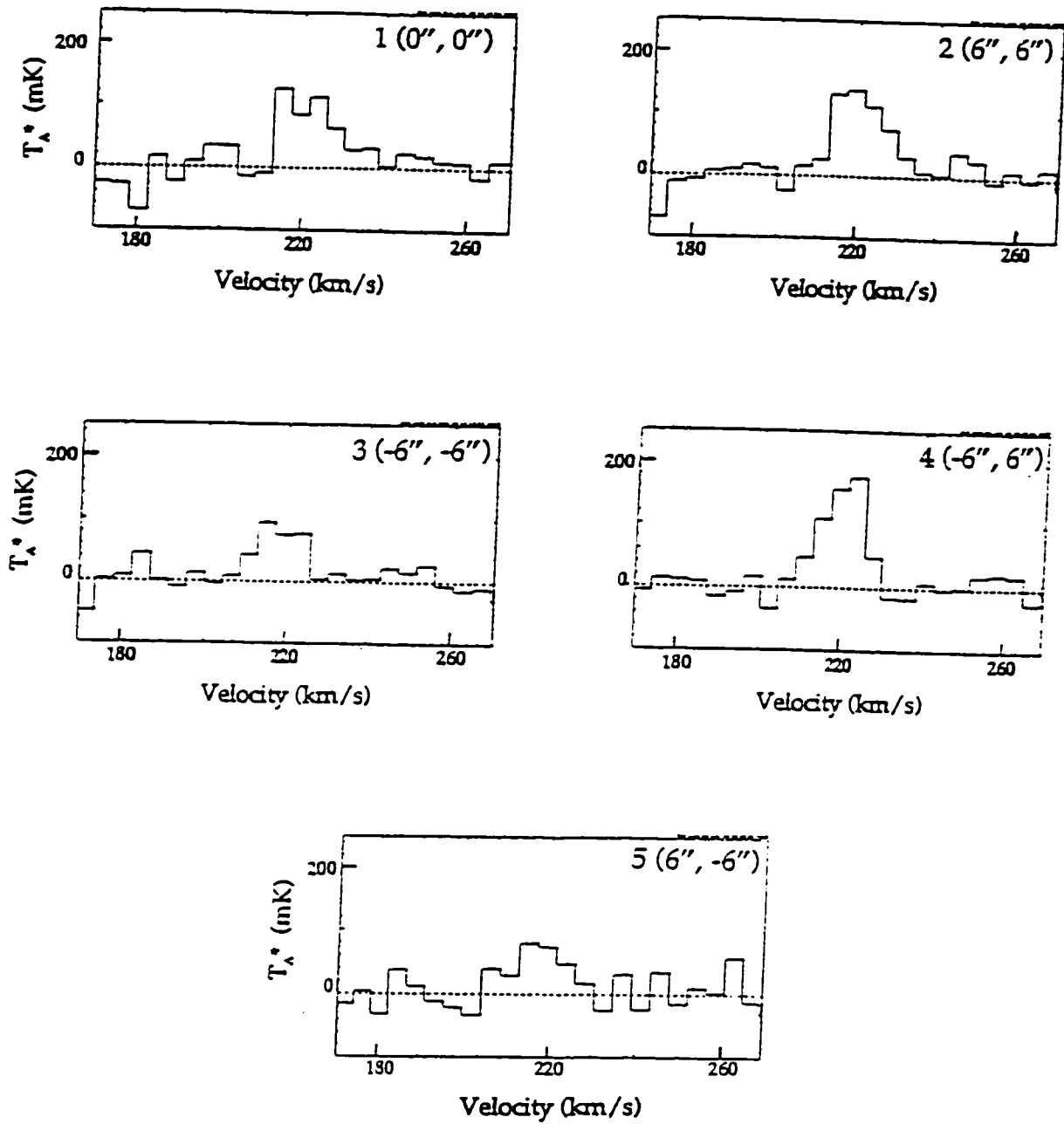


Figure 2.4: Spectra of $^{12}\text{CO } J = 3 \rightarrow 2$ toward five positions in H660. The offsets, which are indicated in the upper right corner of each spectrum, are with respect to the centre of H660: $\alpha = 14^{\text{h}}01^{\text{m}}26^{\text{s}}.3$ and $\delta = 54^{\circ}33'30''.0$.

Source	$\Delta\alpha$ (")	$\Delta\delta$ (")	$\int T_A^* dv$ (K km s ⁻¹)	V_{peak} (km s ⁻¹)	ΔV (km s ⁻¹)	T_{peak} (mK)	Integration time (sec)
H1	0	0	1.92 ± 0.3	221	14.5	117 ± 22	3240
H2	6	6	2.28 ± 0.3	220	14.7	140 ± 17	2880
H3	-6	-6	1.31 ± 0.3	218	14.0	92 ± 17	2880
H4	-6	6	2.33 ± 0.3	220	12.2	183 ± 21	2880
H5	6	-6	1.30 ± 0.3	218	18.8	71 ± 18	2880

Table 2.6: ¹²CO $J = 3 \rightarrow 2$ spectral line parameters for H660. The offsets are with respect to the centre of H660: $\alpha = 14^{\text{h}}01^{\text{m}}26^{\text{s}}.3$ and $\delta = 54^{\circ}33'31''.00$. The quantity $\int T_A^* dv$ is the integrated antenna temperature. The full-width at half-maximum, ΔV , and the central velocity, V_{peak} , for which the maximum antenna temperature value, T_{peak} , occurred were calculated by fitting Gaussian lines to the spectra.

positions with the possible exception of position H2 (see Table 2.7 and Figure 2.5). The peak velocity channel in position H2 has a signal-to-noise ratio of slightly less than 3 and, thus, is only marginally detected. Position H2 is also considered problematic because the line is so wide, which could be a sign that the peak that appears in this position is due to bad baselines. It is worth mentioning, however, that the integration time is much less for H2 than for the other points (390 sec vs. 1800 sec).

Baselines in positions H6, H7, and H8 are overall positive (instead of zero) for velocities lower than the velocity where the emission peaks. Unfortunately, irrespective of whether linear or polynomial baselines were used, the baselines were suspicious. The problematic baselines are not a major concern because only the strongest line in position H1 is used for the calculation of line ratios. Furthermore, these baseline differences are not apparent in the ¹²CO $J = 3 \rightarrow 2$ data (see

Source	$\Delta\alpha$ ($''$)	$\Delta\delta$ ($''$)	$\int T_A^* dv$ (K km s $^{-1}$)	V_{peak} (km s $^{-1}$)	ΔV (km s $^{-1}$)	T_{peak} (mK)	Integration time (sec)
H1	0	0	4.03 ± 0.2	220	15.8	222 ± 11	4500
H2	6	6	$< 3.78 \pm 2.0$	216	39.9*	115 ± 39	390
H4	-6	6	2.43 ± 0.2	220	18.4	119 ± 12	3600
H6	0	12	1.54 ± 0.4	223	22.6	64 ± 19	1800
H7	-12	0	2.66 ± 0.4	216	16.0	152 ± 19	1800
H8	-12	12	2.07 ± 0.4	220	23.0	88 ± 19	1800

Table 2.7: $^{12}\text{CO } J = 2 \rightarrow 1$ spectral line parameters for H660. The offsets are with respect to the centre of H660: $\alpha = 14^{\text{h}}01^{\text{m}}26^{\text{s}}.3$ and $\delta = 54^{\circ}33'30''.0$. The quantity $\int T_A^* dv$ is the integrated antenna temperature. The full-width at half-maximum, ΔV , and the central velocity, V_{peak} , for which the maximum antenna temperature value, T_{peak} , occurred were calculated by fitting Gaussian lines to the spectra. The asterisk indicates that the detection is questionable because the signal to noise ratio is low and the width of the line is unrealistically large: however, it is probable that the line would be detected if the integration had not been interrupted prematurely.

Figure 2.4), which are used for convolving and ultimately for the line ratio estimates.

Lorne Avery and Gerald Moriarty-Schieven³ observed NGC 5462, NGC 5461, and H660 in ‘service’ mode for three shifts (24 hours) during February 1997. This set includes data on NGC 5462 in all three transitions and $^{13}\text{CO } J = 2 \rightarrow 1$ observations of NGC 5461 and H660. The strongest detections in NGC 5462 in both $^{12}\text{CO } J = 2 \rightarrow 1$ (Table 2.8) and $^{12}\text{CO } J = 3 \rightarrow 2$ (Table 2.9) were for position *g*, and not for *a* which coincides with the centre of the region (see the $^{12}\text{CO } J = 2 \rightarrow 1$ emission in Figures 2.6 and 2.7, and the $^{12}\text{CO } J = 3 \rightarrow 2$ emission in Figures 2.8 and 2.9). It is interesting to note that position *g* is 430 pc away from

³Staff scientists at the Joint Astronomy Centre in Hilo, Hawaii.

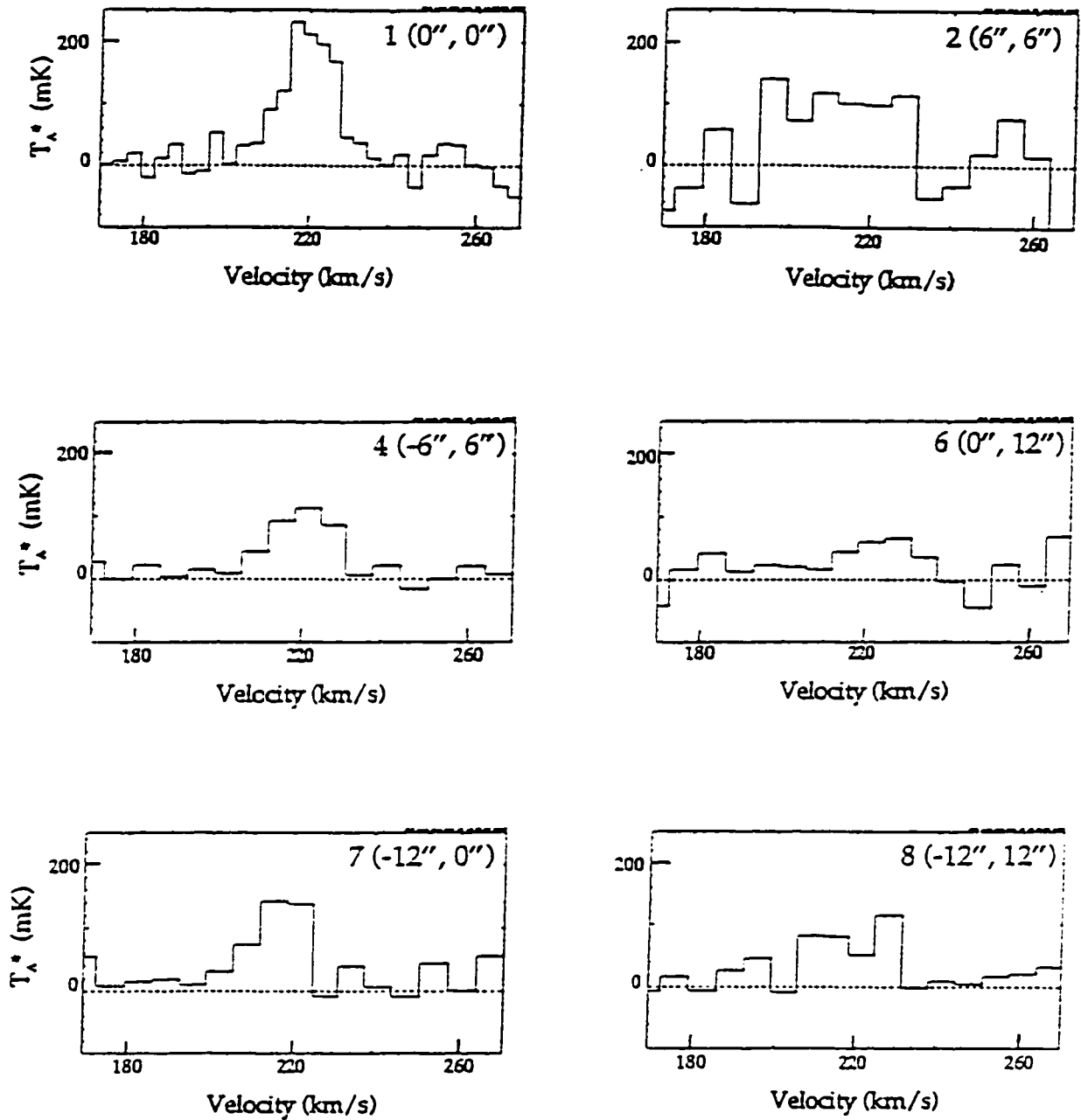


Figure 2.5: Spectra of $^{12}\text{CO } J = 2 \rightarrow 1$ toward six positions in H660. The offsets, which are indicated in the upper right corner of each spectrum, are with respect to the centre of H660: $\alpha = 14^{\text{h}}01^{\text{m}}26^{\text{s}}.3$ and $\delta = 54^{\circ}33'30''.0$. Problems with the baselines are evident in all positions except H1.

the centre of the region. The scale of the antenna temperature has been enlarged for this weaker giant H II region, so that the spectra can be seen.

In fact, it was not possible to make a detection of $^{12}\text{CO } J = 2 \rightarrow 1$ toward the central position in NGC 5462, position *a*. In these tables, if the peak is more than 3 times the rms noise and the width of the lines is reasonable (i.e., $10 \leq \Delta V \leq 25 \text{ km s}^{-1}$), then the line is considered detected. With these criteria, five out of seven and four out of nine detections of $^{12}\text{CO } J = 2 \rightarrow 1$ and $^{12}\text{CO } J = 3 \rightarrow 2$ transitions, respectively, were found. It is not surprising that there were fewer detections in $^{12}\text{CO } J = 3 \rightarrow 2$: the sensitivity was typically a factor of two too low for the expected line strength. Special care was taken so that four positions around NGC 5462g were observed in order to be convolved together so that they could be compared with the lower resolution $^{12}\text{CO } J = 2 \rightarrow 1$ data.

Finally, it was possible to get solid detections of $^{13}\text{CO } J = 2 \rightarrow 1$ toward NGC 5461a and H1 while there was a more questionable detection toward NGC 5462g (see Table 2.10). To achieve these detections, it was necessary to integrate for 3 to 4 hours because $^{13}\text{CO } J = 2 \rightarrow 1$ is very weak, which is also the reason the scale for the antenna temperature in Figure 2.10 has been enlarged ten times. Since $^{12}\text{CO } J = 2 \rightarrow 1$ was not detected toward the centre of NGC 5462, no attempt was even made to observe $^{13}\text{CO } J = 2 \rightarrow 1$ for 5462a. Despite the fact that 5462g was the strongest detection in $^{12}\text{CO } J = 2 \rightarrow 1$, it was only marginally detected in $^{13}\text{CO } J = 2 \rightarrow 1$.

Source	$\Delta\alpha$ (")	$\Delta\delta$ (")	$\int T_A^* dv$ (K km s ⁻¹)	V_{peak} (km s ⁻¹)	ΔV (km s ⁻¹)	T_{peak} (mK)	Integration time (sec)
NGC 5462a	0	0	$< 0.10 \pm 0.10$	308	14.8	$6^* \pm 8$	1800
NGC 5462b	0	6	0.51 ± 0.10	300	17.6	28 ± 8	1800
NGC 5462c	0	-6	$< 0.69 \pm 0.20$	295	34.5*	$19^* \pm 7$	1800
NGC 5462d	6	0	0.49 ± 0.10	304	17.3	27 ± 7	1800
NGC 5462e	-6	0	0.57 ± 0.10	299	16.4	32 ± 7	1800
NGC 5462f	6	6	$< 0.41 \pm 0.10$	297	24.9*	$18^* \pm 7$	1800
NGC 5462g	0	12	0.69 ± 0.05	292	12.0	53 ± 7	1800

Table 2.8: ¹²CO $J = 2 \rightarrow 1$ spectral line parameters for NGC 5462. The offsets are with respect to the centre of NGC 5462: $\alpha = 14^{\text{h}}02^{\text{m}}07^{\text{s}}.6$ and $\delta = 54^{\circ}36'17''.4$. The quantity $\int T_A^* dv$ is the integrated antenna temperature. The full-width at half-maximum, ΔV , and the central velocity, V_{peak} , for which the maximum antenna temperature value, T_{peak} , occurred were calculated by fitting Gaussian lines to the spectra. The asterisks indicate that the detections they accompany are questionable either because of insufficient signal-to-noise (as is the case in position *a*) or because the emission line is too broad (as is the case in position *c*).

Source	$\Delta\alpha$ (")	$\Delta\delta$ (")	$\int T_A^* dv$ (K km s ⁻¹)	V_{peak} (km s ⁻¹)	ΔV (km s ⁻¹)	T_{peak} (mK)	Integration time (sec)
NGC 5462a	0	0	$< 0.45 \pm 0.04$	295	7.4*	21 ± 6	4800
NGC 5462b	0	6	0.20 ± 0.04	295	11.6	18 ± 6	4800
NGC 5462d	6	0	0.56 ± 0.04	296	23.1	25 ± 7	4800
NGC 5462f	6	6	$< 0.66 \pm 0.02$	300	44*	$14^* \pm 6$	6000
NGC 5462g	0	12	1.13 ± 0.02	297	22.2	50 ± 6	6000
NGC 5462h	-6	6	$< 0.41 \pm 0.03$	300	24.1	$15^* \pm 12$	1200
NGC 5462n	0	18	1.00 ± 0.03	300	26.8	36 ± 12	1200
NGC 5462p	6	12	$< 0.94 \pm 0.03$	297	44*	$27^* \pm 12$	1200
NGC 5462q	-6	12	$< 0.49 \pm 0.03$	294	8.7*	49 ± 12	1200

Table 2.9: $^{12}\text{CO } J = 3 \rightarrow 2$ spectral line parameters for NGC 5462. The offsets are with respect to the centre of NGC 5462: $\alpha = 14^{\text{h}}02^{\text{m}}07^{\text{s}}.6$ and $\delta = 54^{\circ}36'17''.4$. The quantity $\int T_A^* dv$ is the integrated antenna temperature. The full-width at half-maximum, ΔV , and the central velocity, V_{peak} , for which the maximum antenna temperature value, T_{peak} , occurred were calculated by fitting Gaussian lines to the spectra. An asterisk beside a value in the velocity width column indicates that the line is either too narrow or too wide to be taken seriously while an asterisk in the column of peak antenna temperatures indicates that there is too much noise to detect the signal with confidence.

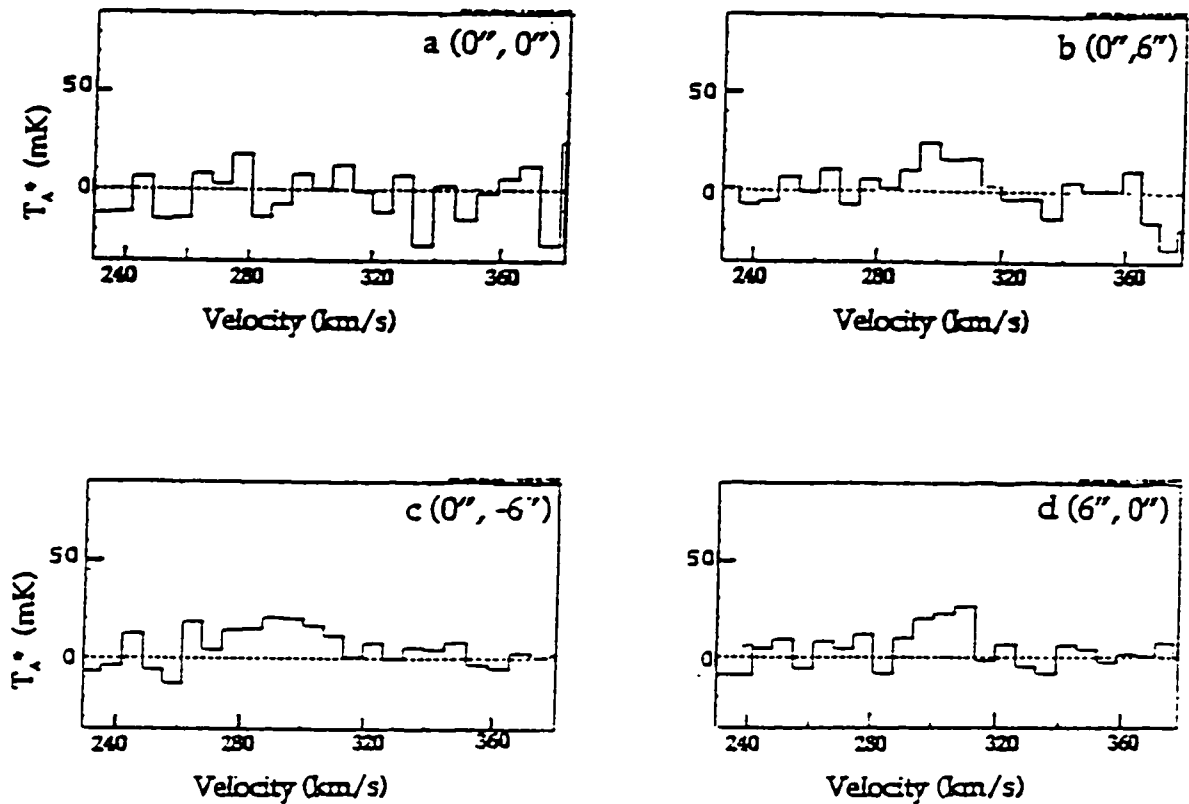


Figure 2.6: Spectra of $^{12}\text{CO } J = 2 \rightarrow 1$ toward the first four positions in NGC 5462. The offsets, which are indicated in the upper right corner of each spectrum, are with respect to the centre of NGC 5462: $\alpha = 14^{\text{h}}02^{\text{m}}07^{\text{s}}.6$ and $\delta = 54^{\circ}36'17''.4$. Positions *a* and *c* yield only an upper limit. The scale has been modified compared to the figures for NGC 5462 to accommodate the weaker signals of NGC 5461 and H660.

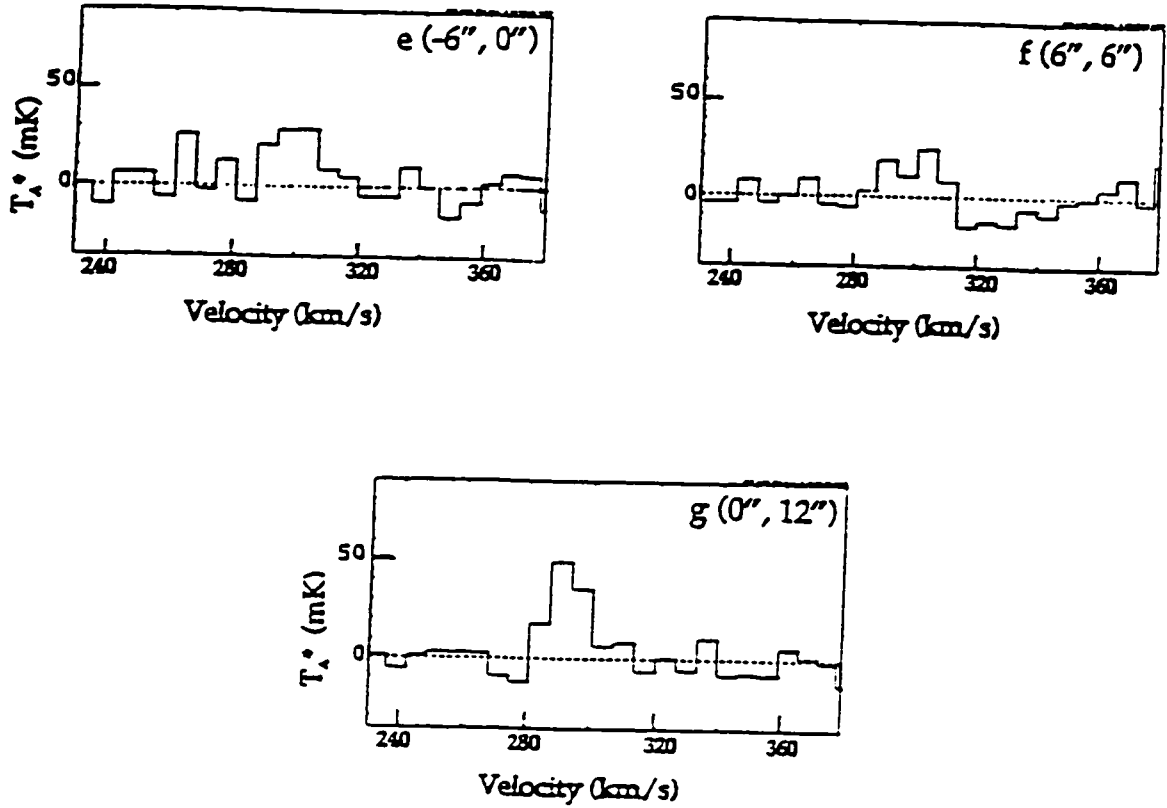


Figure 2.7: Spectra of $^{12}\text{CO } J = 2 \rightarrow 1$ toward the remaining three positions in NGC 5462. The offsets, which are indicated in the upper right corner of each spectrum, are with respect to the centre of NGC 5462: $\alpha = 14^{\text{h}}02^{\text{m}}07^{\text{s}}.6$ and $\delta = 54^{\circ}36'17''.4$. The detection of *f* is marginal, but the detection of position *g* is solid—better than seven sigma.

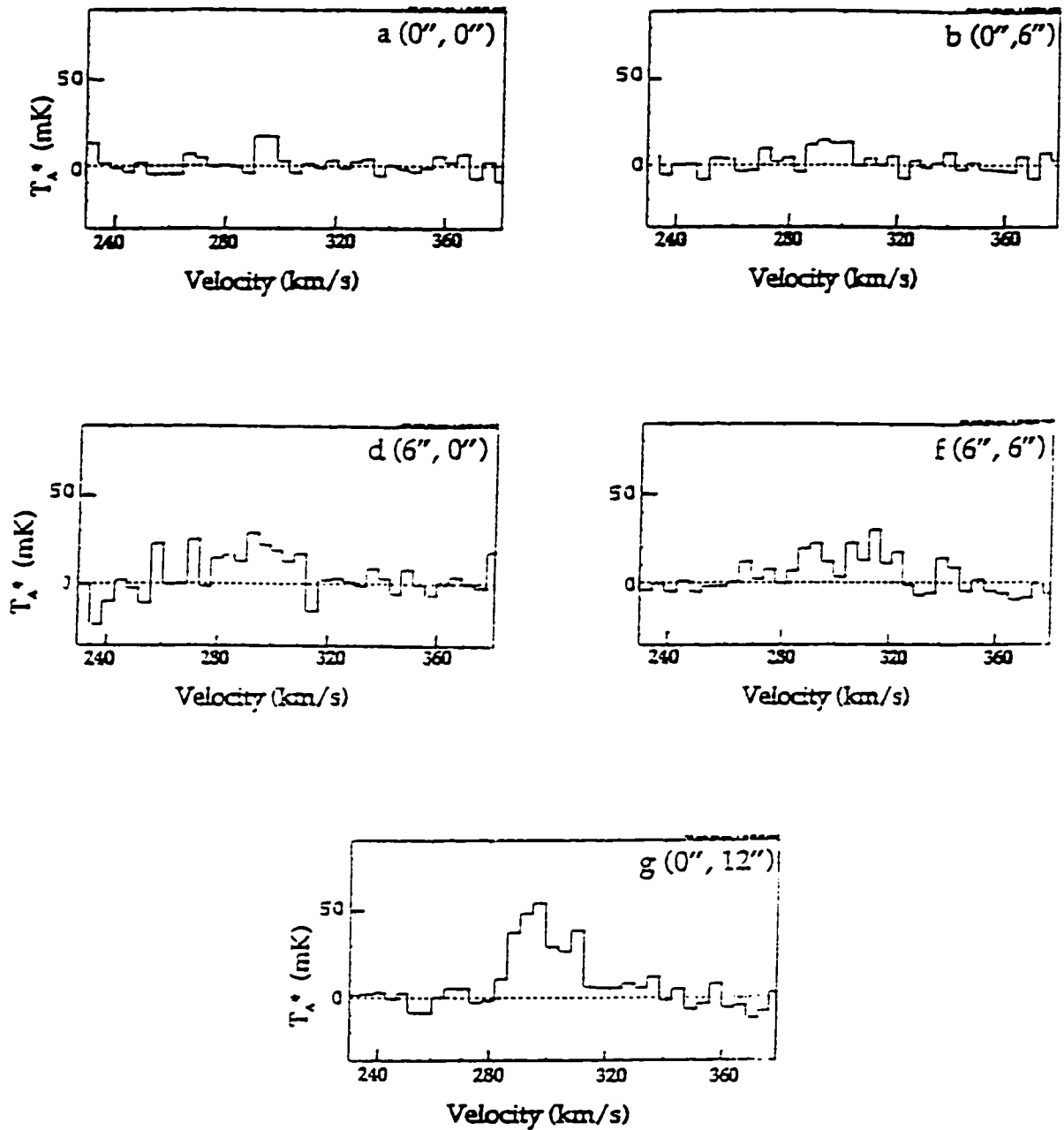


Figure 2.8: Spectra of $^{12}\text{CO } J=3 \rightarrow 2$ toward the first five positions in NGC 5462. The offsets, which are indicated in the upper right corner of each spectrum, are with respect to the centre of NGC 5462: $\alpha = 14^{\text{h}}02^{\text{m}}07^{\text{s}}.6$ and $\delta = 54^{\circ}36'17''.4$. Positions *a* and *f* yield only an upper limit. The scale for these spectra is the same with the equivalent $^{12}\text{CO } J=2 \rightarrow 1$ spectra for NGC 5462.

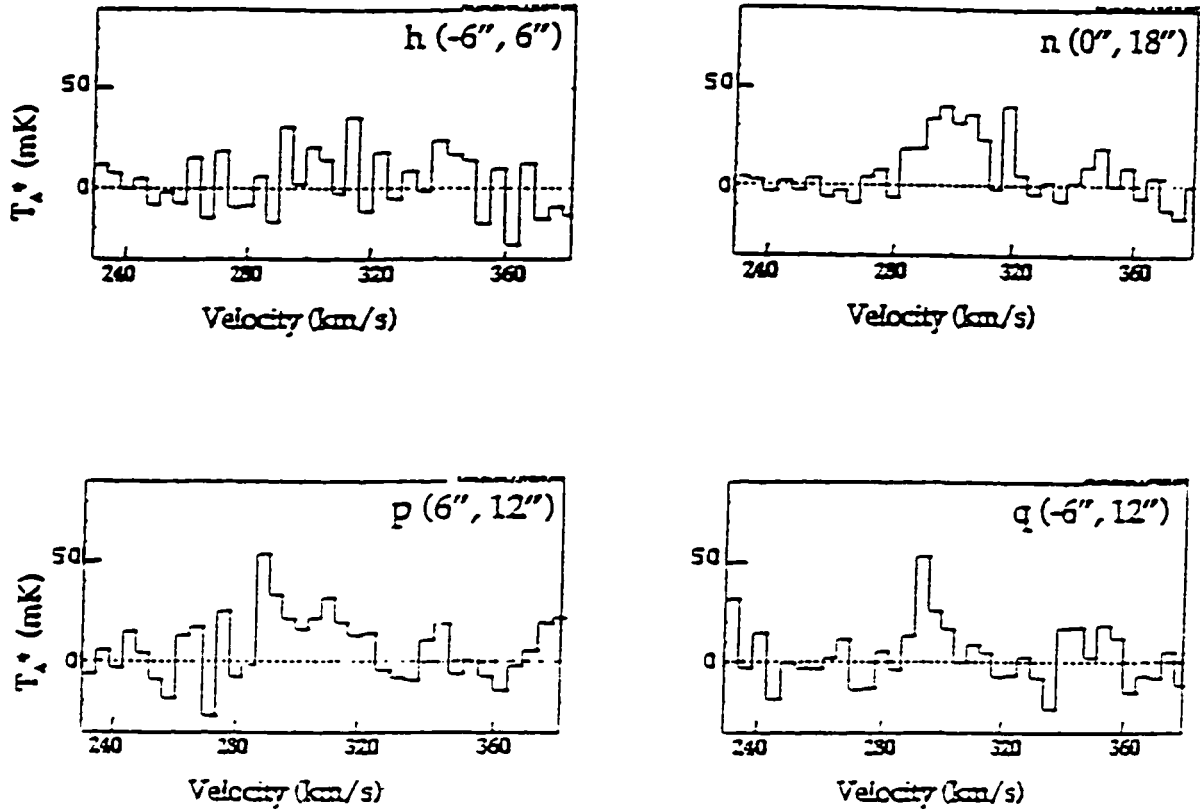


Figure 2.9: Spectra of $^{12}\text{CO } J = 3 \rightarrow 2$ toward the remaining four positions in NGC 5462. The offsets, which are indicated in the upper right corner of each spectrum, are with respect to the centre of NGC 5462: $\alpha = 14^{\text{h}}02^{\text{m}}07^{\text{s}}.6$ and $\delta = 54^{\circ}36'17''.4$. Positions h , p , and q yield only an upper limit. The scale for these spectra is the same with the equivalent $^{12}\text{CO } J = 2 \rightarrow 1$ spectra for NGC 5462.

Source	$\int T_A^* dv$ (K km s ⁻¹)	V_{peak} (km s ⁻¹)	ΔV (km s ⁻¹)	T_{peak} (mK)	Integration time (sec)
NGC 5461a	0.49 ± 0.05	272	27.8	17 ± 4.0	10840
NGC 5462g	0.10 ± 0.1	295	6	10 ± 2.5	15600
NGC H1	0.40 ± 0.1	217	18.1	22 ± 4.3	11100

Table 2.10: ¹³CO $J = 2 \rightarrow 1$ spectral line parameters toward the strongest positions of NGC 5461, NGC 5462, and H660. The quantity $\int T_A^* dv$ is the integrated antenna temperature. The full-width at half-maximum, ΔV , and the central velocity, V_{peak} , for which the maximum antenna temperature value, T_{peak} , occurred were calculated by fitting Gaussian lines to the spectra.

Relative uncertainty of T_{peak}	Fraction of data with corresponding uncertainty
1 – 10 %	25 %
11 – 20 %	25 %
21 – 30 %	28 %
31 – 40 %	11 %
> 41 %	11 %

Table 2.11: The quality of the JCMT spectra is presented by indicating the fraction of observations that have a particular range of values for the relative uncertainty. For example, this table indicates that 50% of the JCMT data have relative uncertainties of less than 20%.

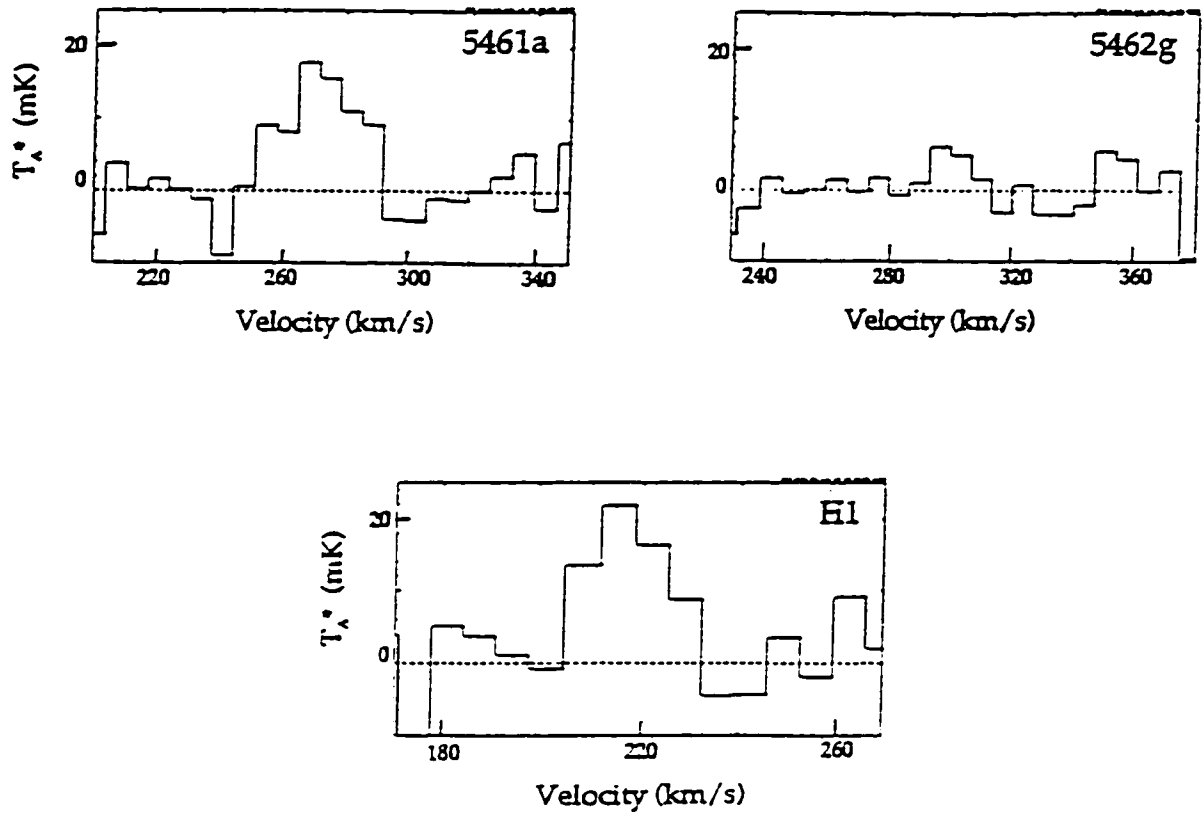


Figure 2.10: Spectra of $^{13}\text{CO } J = 2 \rightarrow 1$ toward the strongest positions of NGC 5461, NGC 5462, and H660. The scale of the y-axis for this figure has been enlarged, so that the features can be seen.

Source	$\int T_R^* dv$ K km s ⁻¹	V_{peak} km s ⁻¹	ΔV (FWHM) km s ⁻¹	$T_{R_{peak}}^*$ mK
NGC 5461(55'')	2.50 ± 0.48	273.8	29.2	78 ± 8
NGC 5462(55'')	0.84 ± 0.27	295.6	45.7	17.5 ± 5
NGC 5471(55'')	0.54 ± 0.20	290.0	52.6	12 ± 12

Table 2.12: $^{12}\text{CO } J = 1 \rightarrow 0$ spectral line parameters for the giant H II regions observed with the NRAO 12-meter telescope. The quantity $\int T_R^* dv$ is the integrated corrected radiation temperature. The full-width at half-maximum, ΔV , and the central velocity, V_{peak} , for which the maximum corrected radiation temperature value, $T_{R_{peak}}^*$, occurred were calculated by fitting Gaussian lines to the spectra. I have included the beam size of the telescope as a reminder that the area it observes is larger than that observed by the JCMT.

2.1.2 National Radio Observatory (NRAO) 12-meter

On November 6, 1996, I used the NRAO 12-meter telescope to observe NGC 5461, NGC 5462, and NGC 5471 in the rotational transition of $^{12}\text{CO } J = 1 \rightarrow 0$ (Figure 2.11 and Table 2.12).

The beam is large enough (55'') to encompass each of the three giant H II regions, so the data consisted of three long-integration spectra. For the three regions, the integration times were 60 minutes, 120 minutes, and 78 minutes for NGC 5461, NGC 5462, and NGC 5471, respectively. Each individual scan was 6 minutes. Typical system temperatures at 115 GHz were 350 – 400 K. The 256 channel 1 MHz (2.6 km s⁻¹) dual polarization filterbank was configured in series mode to

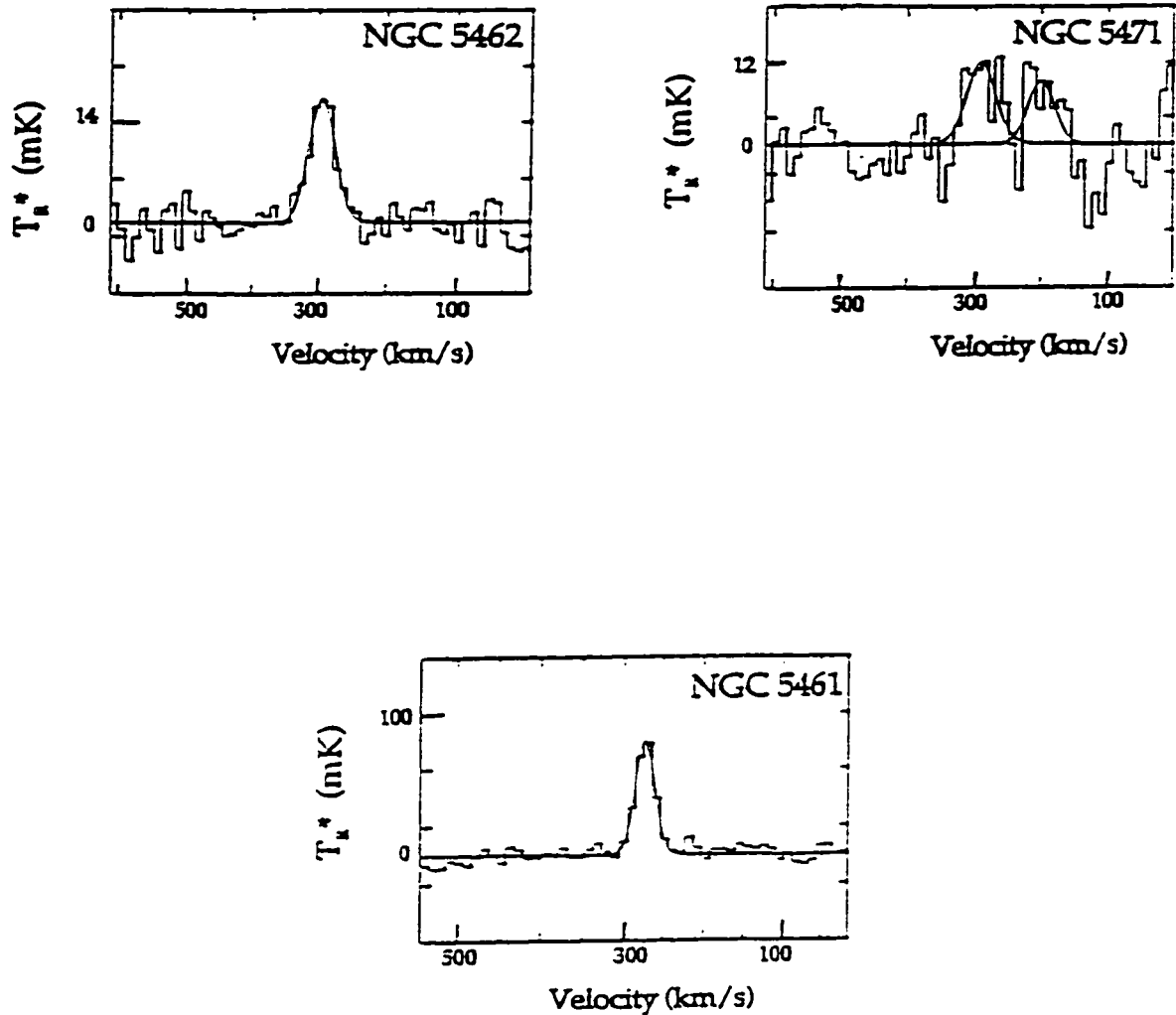


Figure 2.11: NRAO spectra of $^{12}\text{CO } J = 1 \rightarrow 0$ toward the three observed giant H II regions, NGC 5462, NGC 5471, and NGC 5461. Note that the scale differs for the three spectra; the strongest signal comes from NGC 5461. There is a double peak for NGC 5471; the relevant peak is the one on the left; the one on the right is probably an unrelated cloud in the line of sight.

gain $\sqrt{2}$ in signal at the expense of the polarization data, which are not very important in this study. This telescope measures corrected radiation temperature, T_R^* , as opposed to the corrected antenna temperature, T_A^* , that the JCMT measures (see Appendix on page 177). The telescope scale was checked by observing K3-50 [observed peak $T_R^* = (24 \pm 0.1)$ mK]—the uncertainty in the T_R^* calibration was estimated to be about 15%.

To reduce the data I used UniPOPS: a version of the POPS (People-Oriented Parsing Service) command-line interpreter for UNIX environments. Linear baselines were removed from two of the spectra (NGC 5461 and NGC 5471) while a polynomial baseline was removed from the spectrum of NGC 5462. It was necessary to sacrifice some velocity resolution to improve the signal-to-noise ratio: the data were smoothed to a resolution of 10 km s^{-1} (or 4 MHz at 115 GHz), which is still satisfactory because the lines are very wide.

2.2 Interferometer Emission Data

2.2.1 Owens Valley Millimeter Array

NGC 5461 and NGC 5462 were observed with the Owens Valley Millimeter-Wave Interferometer in the Spring 1996 and Spring 1997 respectively. This millimeter array has 6 antennae, which yield a total of $N(N - 1)/2 = 15$ baselines—the longest is 235 m. The diameter of each dish is 10.4 m. NGC 5461 was observed during three tracks (8 hour shifts): one poor and one good high resolution track, and one good low resolution track; NGC 5462 was also observed for two tracks: one useable high resolution track and one good low resolution track.

The dishes of the Owens Valley array can be configured in a variety of ways depending on the resolution needed and the declination of the object to be observed. Two configurations of the array were used: configuration A (Table 2.13) and C (Table 2.14), which were combined so that the synthesized beam is $2''.62 \times 2''.03$ for NGC 5461 and $3''.14 \times 2''.73$ for NGC 5462. The sensitivity of the array as a function of position (i.e., the beam pattern) for the two sets of observations are shown in Figures 2.12 and 2.13.

The Owens Valley array makes square maps that are 1' on a side; since there is a map, there is no need to number positions as was done for the JCMT data. The $(0'', 0'')$ point in the maps is the central position of the giant H II region: for NGC 5461, the coordinates are $\alpha = 14^{\text{h}}01^{\text{m}}55.^{\text{s}}6$ and $\delta = 54^{\circ}33'31''$, which are also the coordinates of the centre of NGC 5461a; for NGC 5462, they are $\alpha = 14^{\text{h}}02^{\text{m}}7.^{\text{s}}6$

Antenna	Location east (m)	Location north (m)
1	0	220
2	-65	0
3	100	0
4	-100	0
5	0	140
6	30	0

Table 2.13: Positions of the six Owens Valley antennas in the A configuration relative to the intersection point of the north-south track with the east-west track.

Antenna	Location east (m)	Location north (m)
1	0	80
2	-50	0
3	50	0
4	-65	0
5	0	30
6	-20	0

Table 2.14: Positions for the six Owens Valley antennas in the C configuration relative to the intersection point of the north-south track with the east-west track.

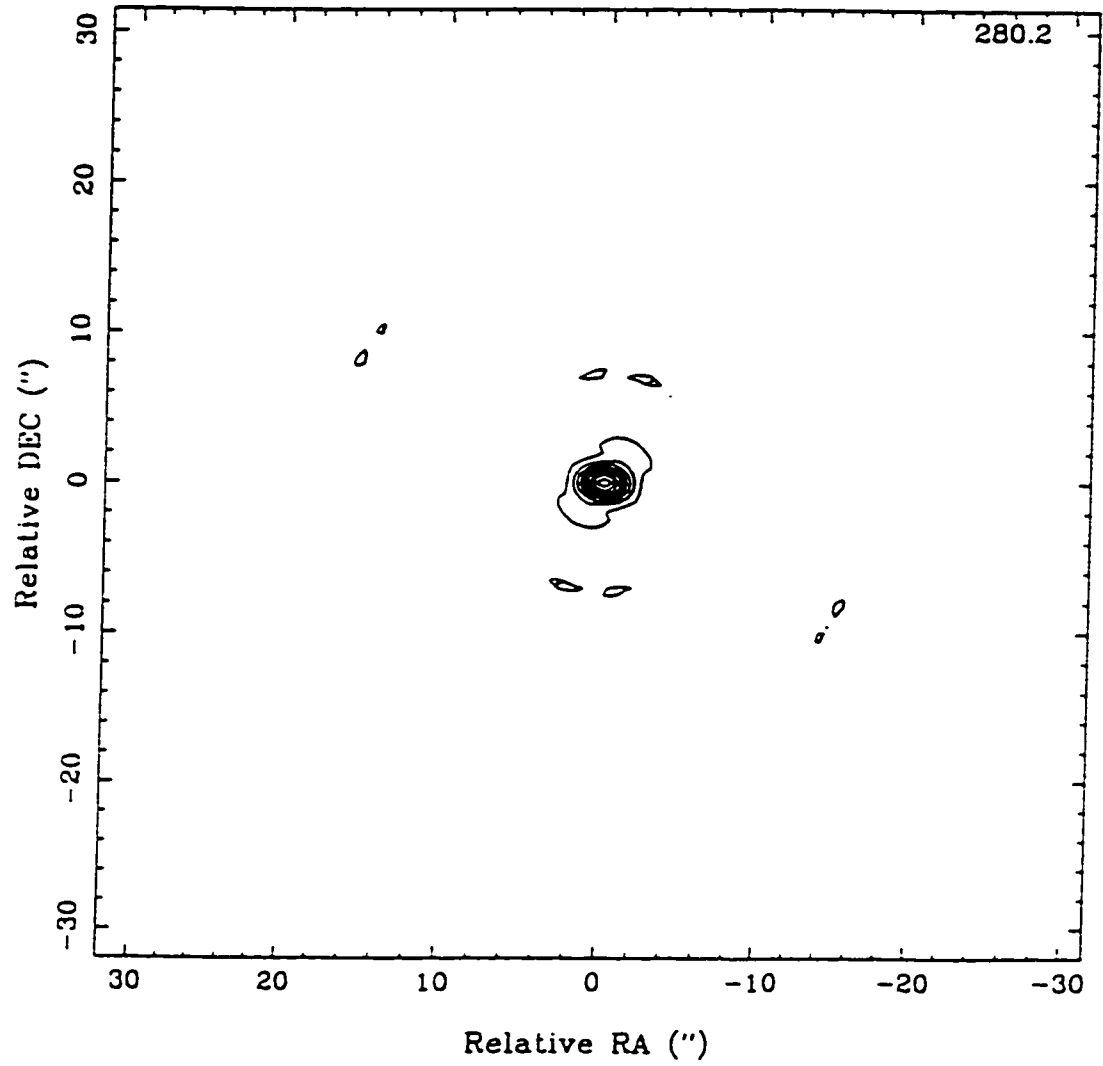


Figure 2.12: The primary beam at the Owens Valley millimeter array during the observations of NGC 5461. The contour levels are 10%, 20%, 30%, 40%, 50%, 60%, 70%, 80%, 90%, and 100% of the maximum intensity.

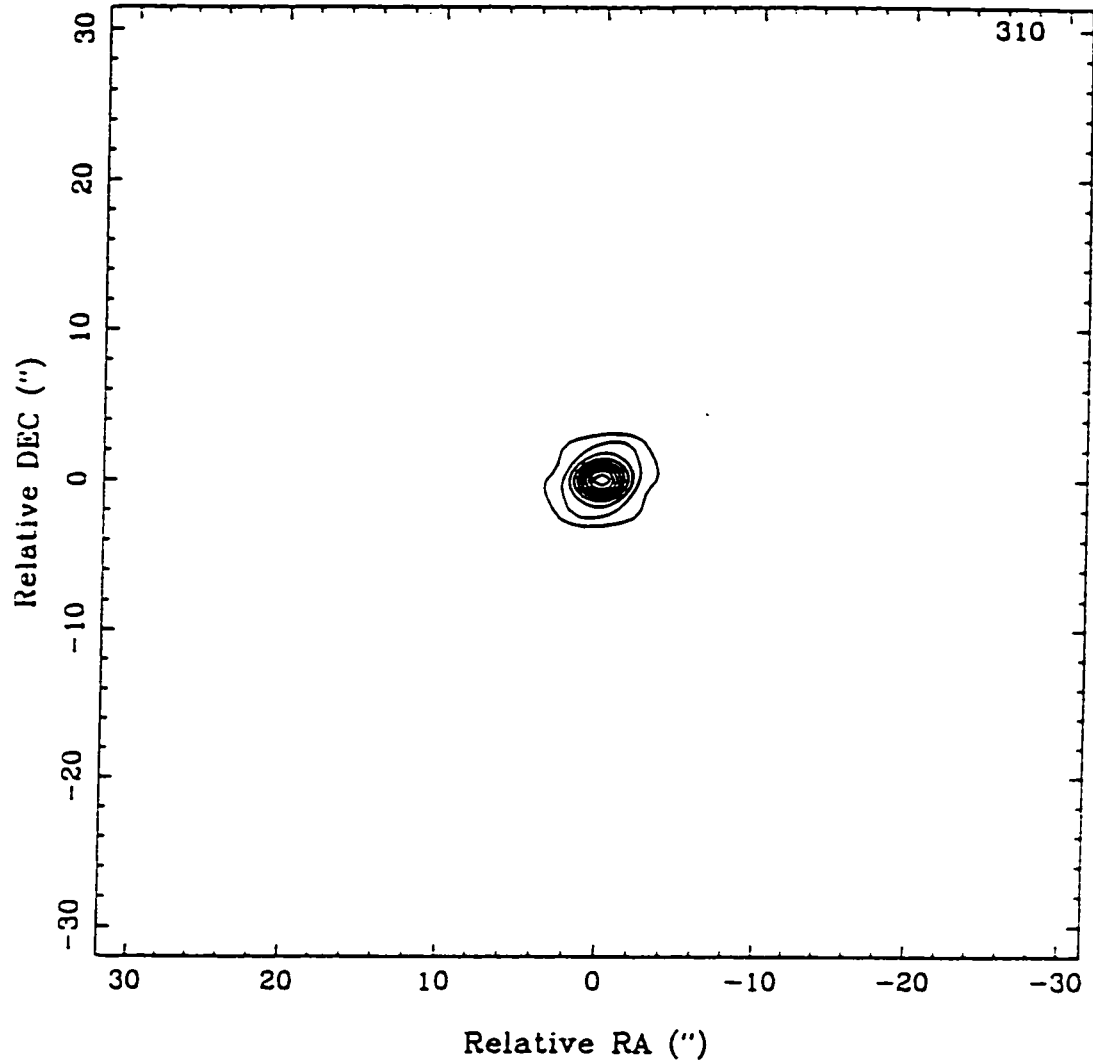


Figure 2.13: The primary beam at the Owens Valley millimeter array during the observations of NGC 5462. The contour levels are 10%, 20%, 30%, 40%, 50%, 60%, 70%, 80%, 90%, and 100% of the maximum intensity.

and $\delta = 54^{\circ}36'17''.4$, which are the coordinates of the centre of NGC 5462a. Typical single-sideband system temperatures at the zenith were 500 – 600 K.

All four independent correlator modules of the digital spectrometer system were used to observe the $^{12}\text{CO } J = 1 \rightarrow 0$ line with an effective bandwidth of 126 MHz (or 328 km s^{-1}), which is suitable for a line with a FWHM of 40 km s^{-1} . This correlator setup yielded a resolution per channel of 1 MHz (or 2.6 km s^{-1}), which is satisfactory.

To reduce data from the Owens Valley interferometer, I used the `mma`⁴ software package, which is written and maintained by the Caltech millimeter interferometry group. The `mma` package enables the observer to calibrate the data obtained. In order to achieve the most accurate calibration, one must use filters to automatically remove—for the purposes of flux calibration—all the data that are uncertain (usually with low coherence, i.e., $< 70\%$).

After poor data have been removed, one can translate the counts to Janskys, thereby establishing the flux scale (Jy/count). Ideally, this absolute flux calibration is performed by measuring the flux from a small source such as the planet Neptune. For the two tracks of NGC 5461, Neptune was used for the flux calibration; for the good high resolution track, Neptune was not high enough in the sky, so the flux calibration was based on the quasar 3C273. The flux measurements that resulted from these sources agreed within 20%. The situation was similar for the tracks

⁴`mma` stands for millimeter array analysis (Steve Scott—private communication) and is written in lower case letters to avoid confusion with the MMA—the NRAO initiative to build a new millimeter array.

of NGC 5462. One track was calibrated with Uranus observations while the other with the quasar 3C345. The flux measurements from these two tracks were even more consistent than the measurements from the NGC 5461 tracks: they agreed to within 10%.

The main reason the flux calibration is performed is to estimate the effect of the Earth's atmosphere on the phase and the amplitude of the signal by measuring repeatedly the strength of the gain calibrator. This calibrator is an object near the source: the stronger the gain calibrator and the nearer it is to the source, the more dependable the overall gain calibration is. I used the gain calibrator 1418+546 [$\alpha(1950) = 14^{\text{h}}18^{\text{m}}06^{\text{s}}.200$ and $\delta(1950) = +54^{\circ}36'57''.80$], which is fairly weak—unfortunately there are no stronger sources close enough to M101. The average measured gain calibrator flux for the NGC 5461 observations was 0.80 Jy while the 1418+546 flux for the NGC 5462 observations a year later was 0.55 Jy. Since it is possible that the intrinsic brightness of the gain calibrator changed during the course of a year, I adopted the two separate values for the remaining analysis.

After the flux calibration is applied to all the data, they should be edited before continuing the reduction to remove poor data. The main criterion is that the coherence has to be higher than 50% (with the exception of points that were assigned a value of zero coherence because the signal-to-noise was too low to measure the coherence). The second half of the poor high resolution NGC 5461 track had to be omitted due to fairly high humidity. Despite the fact that the good high resolution track was taken under good weather conditions, 20% of the data had to be removed due to anomalies in the calibration; this problem is probably due to the weakness

of the gain calibrator. Finally, the low resolution track was good: only 8% had to be removed due to some technical problems with the focusing of antenna 6. For the 5462 tracks, the high resolution track had problems at the beginning due to strong winds, so 12% of the data were deleted. The low resolution track had low coherences at the beginning and the end of the track, and, therefore, approximately 30% of the data were removed.

Finally, one has to observe a strong source (such as a quasar) to determine the channel-to-channel variation across the spectrometer band: this step is the passband calibration. For the NGC 5461 tracks, quasars 3C273 and 3C454.3 were used. For the NGC 5462 tracks, quasars 3C454.3 and 3C345 were used.

After the basic reduction was completed, I used MIRIAD⁵—a software package with a cleaning tool to reduce interferometer data. One of the first considerations when one deals with interferometric data is the weighting scheme of the data. Why would one have to consider a weighting scheme? First, all data points are not of the same quality because of changing weather conditions, system temperature etc. MIRIAD permits one to flag data points that are considered problematic, i.e., it will allow the observer to assign these points zero weight. During the first reduction of the NGC 5461 and NGC 5462 data, no points were excluded, but the resulting map features were found to be elongated in a NE-SW direction. Therefore, the extreme points (fewer than 0.5% of the data) that had very high amplitudes were removed—only 10% of the channels were affected by this. The final maps do not have any systematic streaks in them; the fact that the features in NGC 5461 are

⁵A program developed by the Berkeley-Illinois-Maryland Association.

placed like beads of a string is due to the presence of a spiral arm of M101.

Another consideration one must address when ‘cleaning’ the maps is that the coverage of an interferometer is not uniform: an interferometer has usually more short baselines, and, therefore, the low spatial frequencies tend to be over-represented at the expense of high resolution features. There are two different types of weighting schemes depending on the strength of the data. If the signal-to-noise ratio is small, one would typically use the *natural* weighting scheme, which assigns the same weight to all data points. Since the short baselines are more abundant, the beam will appear as a broad low-level plateau.

If the signal-to-noise ratio is large, then one would be tempted to use the *uniform* weighting. This scheme gives each data point a weight which is inversely proportional to the density of points within some radius of the point. Therefore, for short baselines, where the coverage is more complete, each individual data point will have less weight than points that correspond to longer baselines. The uniform weighting achieves higher resolution images but reduces the signal to noise. Unfortunately uniform weighting could not be used because the spectral lines were too weak.

All maps were ‘cleaned’ to the 1.5σ level with fewer than 1000 iterations. The rms noise and the maximum signal for the *integrated maps*—with integration over twenty channels (52 km s^{-1})—were $0.025 \text{ Jy beam}^{-1}$ and $0.12 \text{ Jy beam}^{-1}$ for NGC 5461, and $0.022 \text{ Jy beam}^{-1}$ and $0.09 \text{ Jy beam}^{-1}$ for NGC 5462.

Once the cleaning process is completed, one can identify the real features of

the maps. The features of interest are the emission peaks in the maps, which correspond to GMCs (Vogel et al., 1988). In the following discussion, the terms GMC and feature are used interchangeably.

Before describing the criteria that were chosen to find the GMCs, I will explain the three different types of plots which are useful for this endeavour. The integrated map, as mentioned before, is a plot that has been integrated over a wide velocity range (in this case 52 km s^{-1}) to include all the emission. The *channel maps* are a series of maps where the region is plotted by integrating over one channel only (2.6 km s^{-1}): these help identify real features because it is possible to follow the feature's shape in velocity space. Finally, the *optimum maps* for each GMC are integrated only over the velocity range in which the feature is visible at the 3σ level or better.

It must be stated in no uncertain terms that the process of determining the GMCs is fairly subjective. For this thesis, I have chosen three relatively conservative criteria so that the results inspire some confidence. The first criterion used to identify the GMCs is that the feature should be at least 2σ in the integrated map. Near the strong features on the map, there are several 2σ , even 2.5σ , features that coexist with equally strong negative 'sources'; therefore, it is important to establish a second criterion to discriminate the signal from the noise. For the application of this criterion, the data were plotted on individual channel maps with a resolution of 2.6 km s^{-1} . After careful inspection of the individual channel maps, I concluded that the best way to proceed was to look for 3σ features that persisted over two consecutive channels, so noise was not mistaken for signal; this method, however,

could result in underestimating the number of GMCs, especially the ones with a narrow velocity width.

The best velocity range for each GMC candidate is determined from the channel maps, and for each feature, the optimum map integrated for the appropriate velocity range can be plotted. The optimum maps are used to apply the third criterion: the feature in the optimal map should have signal of at least 3σ . It is possible for the second criterion to be satisfied but not the third because the features drift slightly from channel-to-channel, so the 'optimum' integrated flux can be less than 3σ above the noise.

The integrated map of NGC 5461 (Figure 2.14) has thirty-three features with signal of at least 2σ . Of these thirty-three features that appear in the integrated map, nine can be seen at the 3σ level in two consecutive channels of the channel maps in Figures 2.15 to 2.19. In addition, I have also considered two other features (4 and 6 in Figure 2.14) that appear on the integrated map and in three consecutive channels at the 2σ level.

Of the eleven GMCs, one is eliminated by the third criterion, i.e., the total flux in the optimum map is not three times higher than the noise of the optimum map. The rms noise determined by the 'dirty' maps varies between $0.05 - 0.069$ Jy beam⁻¹ depending on the number of channels over which the signal has been integrated. As the number of channels increases, the rms noise level decreases.

The characteristics of the ten features appear in Table 2.15. The GMCs appear in order of increasing central velocity, v . The sizes and position were determined

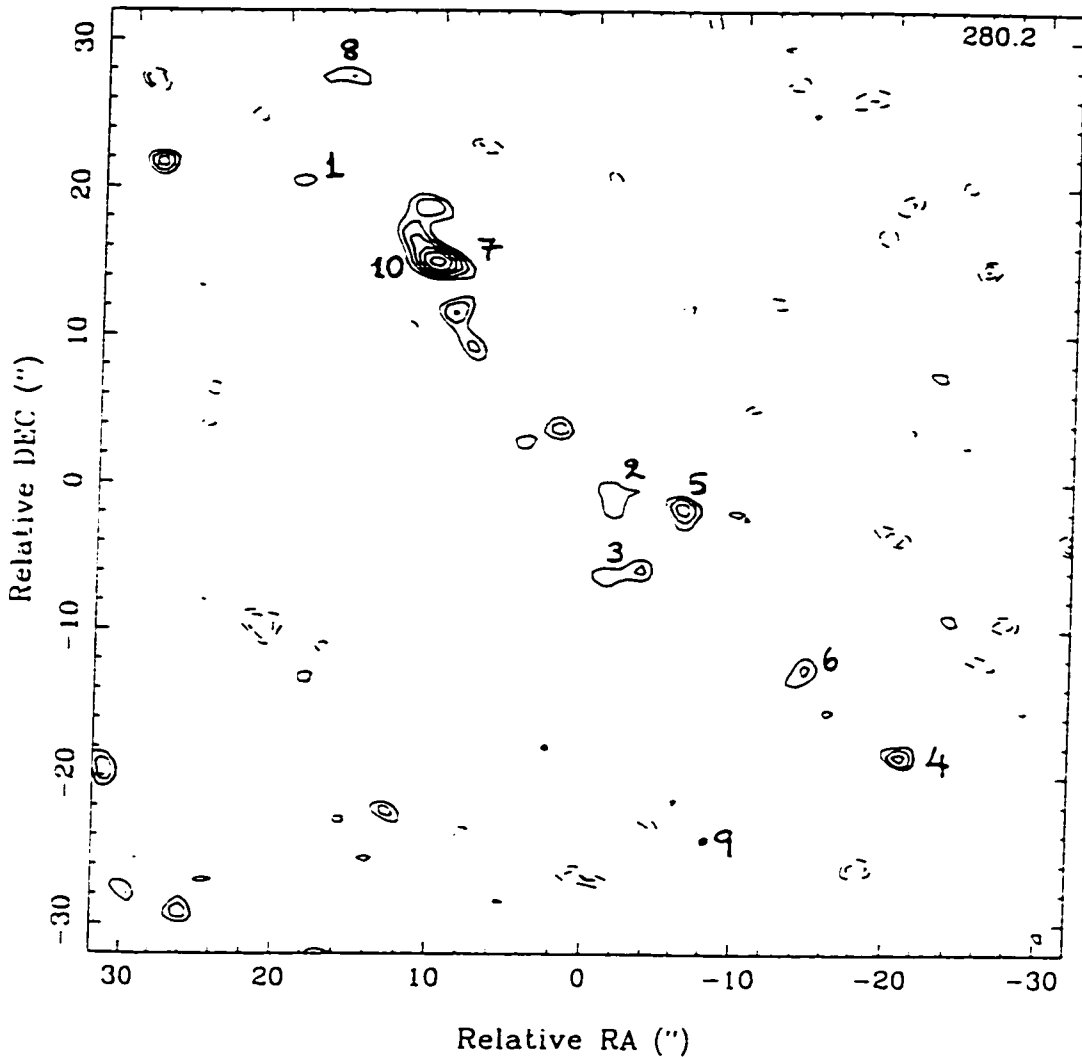


Figure 2.14: Integrated Owens Valley map of NGC 5461 over 52 km s^{-1} . The contours have been plotted at the $\pm 2\sigma$, $\pm 2.5\sigma$, $\pm 3\sigma$, $\pm 3.5\sigma$, $\pm 4\sigma$, and $\pm 4.5\sigma$; positive contours are solid while negative contours are dotted. The rms noise is $0.024 \text{ Jy beam}^{-1}$. The central velocity appears in the upper right hand corner (in km s^{-1}). An identifying number beside each peak designates each GMC; GMCs 7 and 10 coincide spatially, but they have different velocities (see Table 2.15).

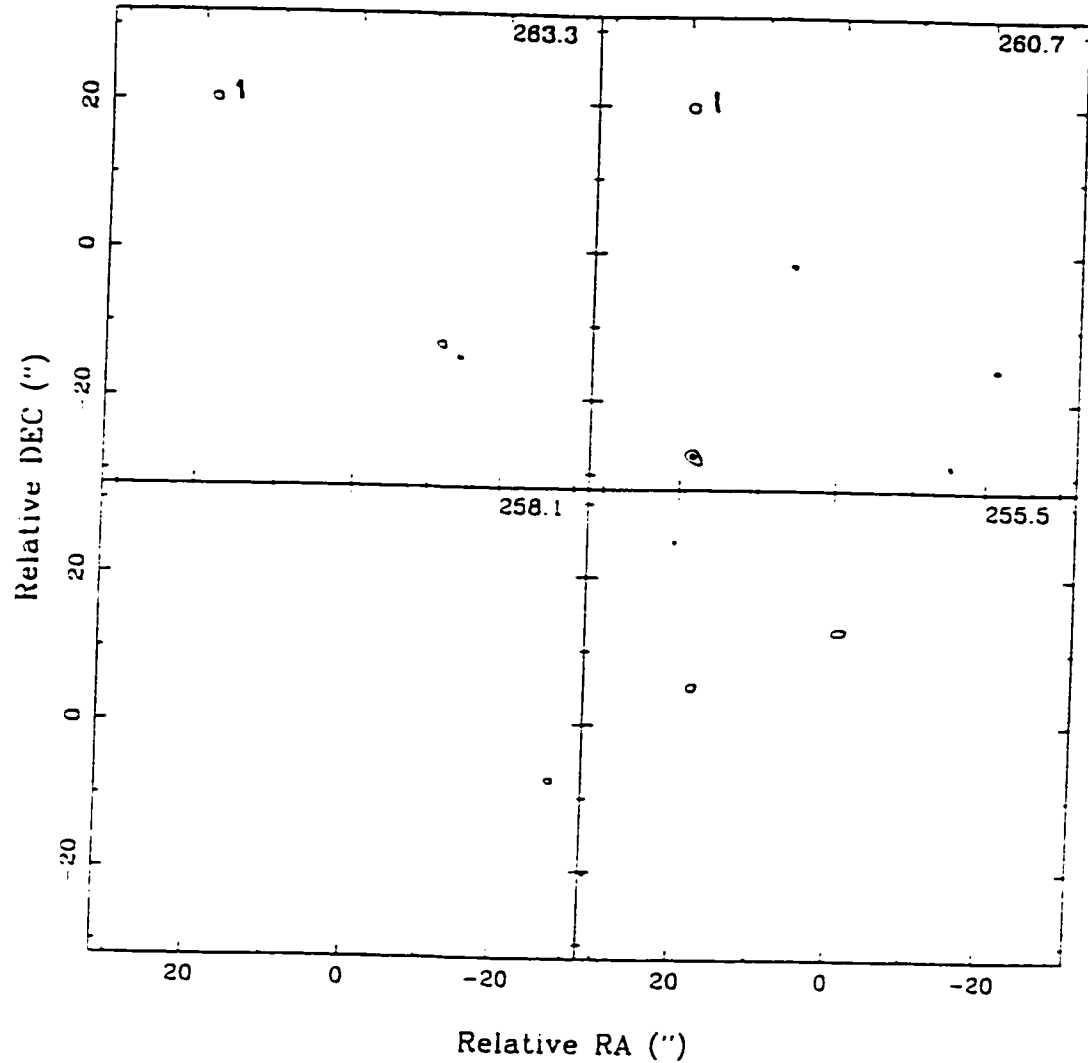


Figure 2.15: First four channel maps of NGC 5461. The central velocity, v , appears in the upper right hand corner (in km s^{-1}). The contours have been plotted at 3σ , 4σ , and 5σ with rms noise = $0.07 \text{ Jy beam}^{-1}$.

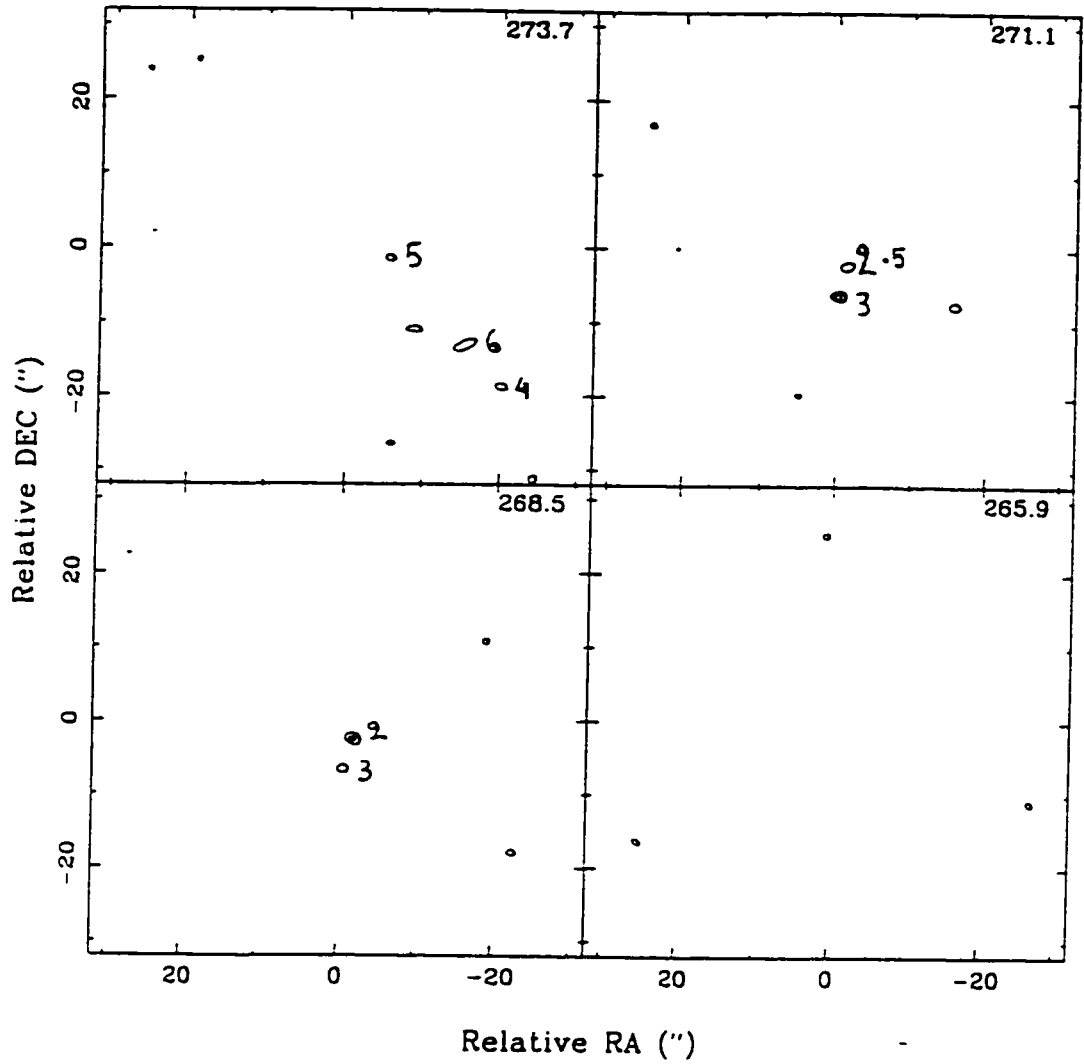


Figure 2.16: Second set of channel maps of NGC 5461. The central velocity, v , appears in the upper right hand corner (in km s^{-1}). The contours have been plotted at 3σ , 4σ , and 5σ with rms noise = $0.07 \text{ Jy beam}^{-1}$. Clouds 4 and 6 have three 2σ consecutive channels that do not appear in these maps.

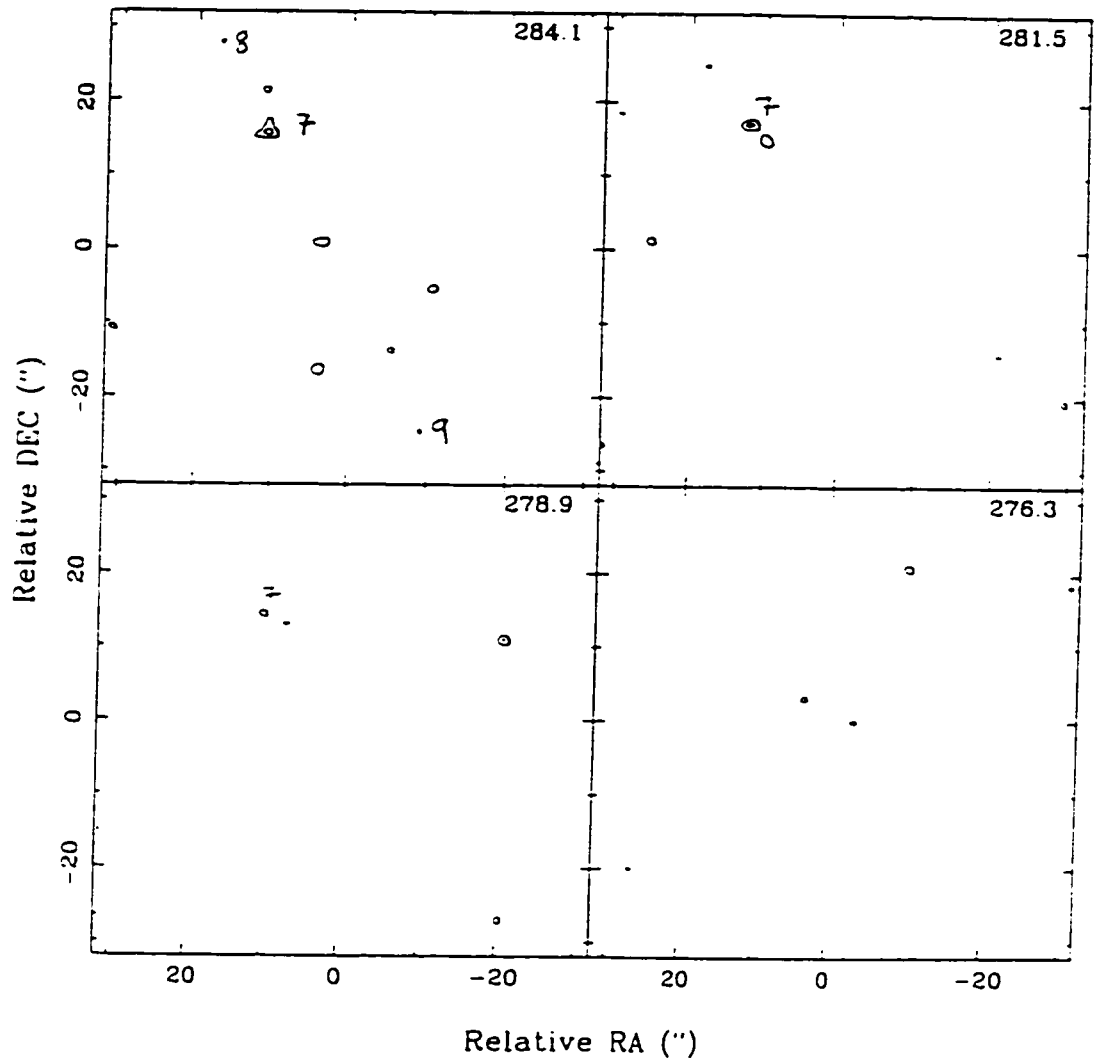


Figure 2.17: Third set of channel maps of NGC 5461. The central velocity, v , appears in the upper right hand corner (in km s^{-1}). The contours have been plotted at 3σ , 4σ , and 5σ with rms noise = $0.07 \text{ Jy beam}^{-1}$.

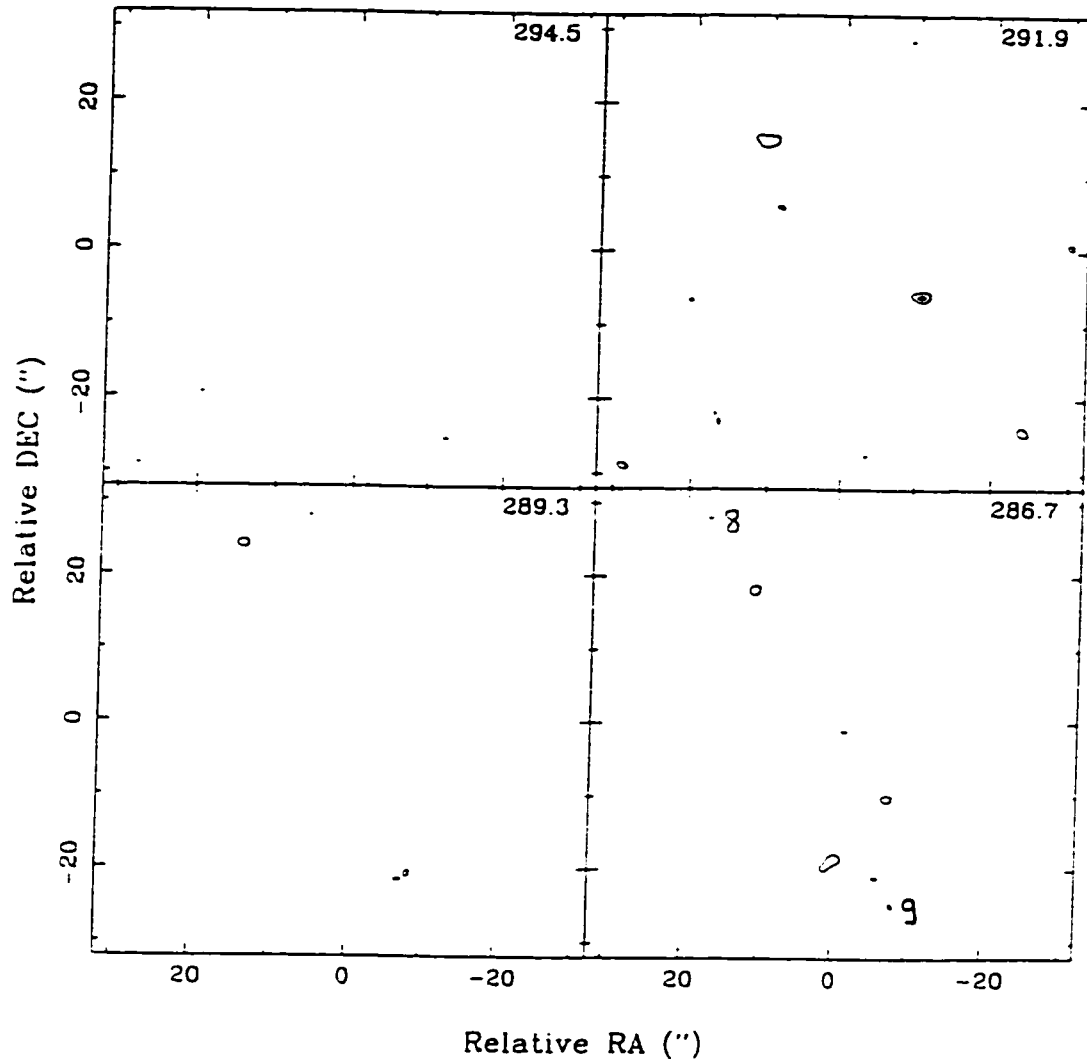


Figure 2.18: Fourth set of channel maps of NGC 5461. The central velocity, v , appears in the upper right hand corner (in km s^{-1}). The contours have been plotted at 3σ , 4σ , and 5σ with rms noise = $0.07 \text{ Jy beam}^{-1}$.

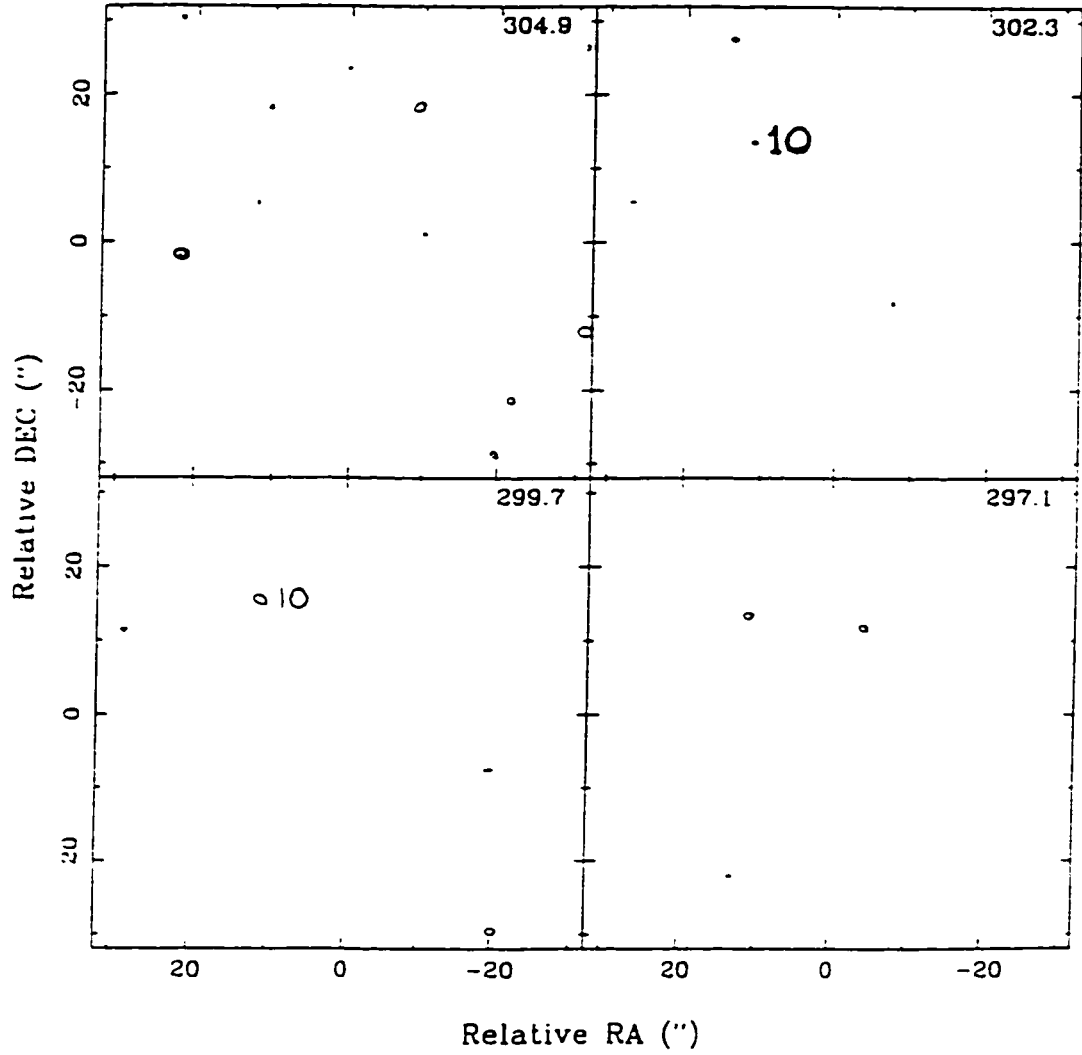


Figure 2.19: Last four channel maps of NGC 5461. The central velocity, v , appears in the upper right hand corner (in km s^{-1}). The contours have been plotted at 3σ , 4σ , and 5σ with $\text{rms noise} = 0.07 \text{ Jy beam}^{-1}$.

by the optimum maps (see Figures 2.20 to 2.28), which were integrated over the total velocity range of each GMC.

The dimensions, which are given in parsecs at the distance of 7.4 Mpc, are measured by the size of the contour at FWHM of the optimum map for each GMC: the deconvolved diameters from the beam are calculated in Table 4.2. The GMC positions are given for the centre of the peak of the GMC in terms of offsets from the centre of the region: most GMCs, however, had their peak in their centre—the shapes were quite axisymmetric. The estimated uncertainties are 10 pc in size and $0''.5$ in position.

Table 2.15 also includes the integrated intensity, which is the product of the total flux calculated by a routine in MIRIAD and the velocity width, Δv , of the optimum map. To calculate the total flux, I used a box as close as possible to the shape of the contour at zero intensity in the optimum maps. The velocity width of the optimum maps was determined by the number of consecutive channel maps on which the feature appeared, and Δv can be as small as 5.2 km s^{-1} and as large as 10.4 km s^{-1} . The integrated intensity varies from 0.96 to $4.42 \text{ Jy km s}^{-1}$. Finally, I calculated the equivalent brightness temperature, T_B , by multiplying the total flux by the conversion factor from Janskys to Kelvin (17.34 K/Jy).

Two features, GMCs 7 and 10, have similar coordinates, but they are separated in velocity space. In other words, they are in the same line of sight but moving with different velocities. In most optimum maps, there is more than one GMC; however, only the feature for which the map has been optimized is labeled. In Figure 2.27,

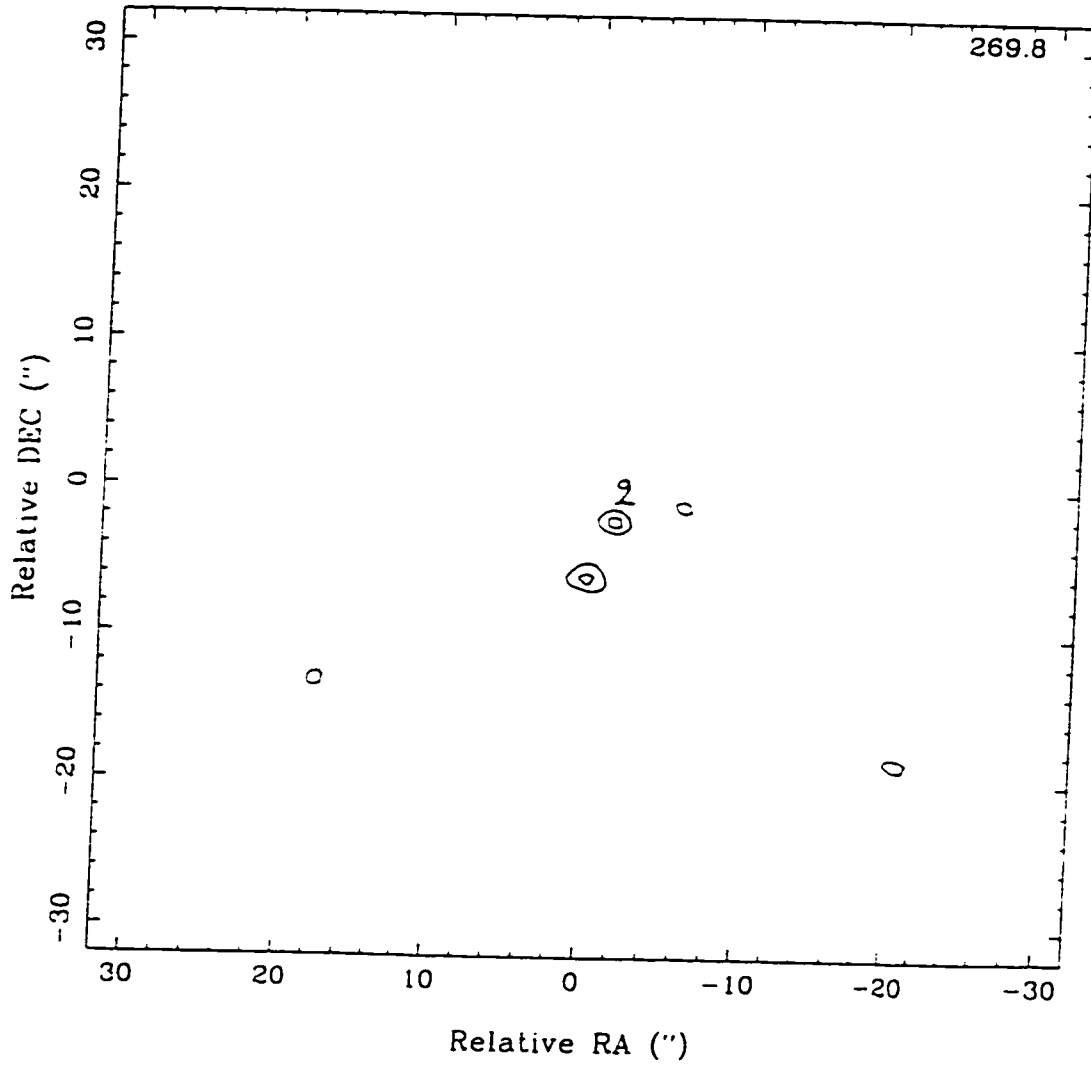


Figure 2.21: Optimum map of GMC 2 in NGC 5461. The contours have been plotted at the $\pm 3\sigma$ and $\pm 4\sigma$, where σ is $0.050 \text{ Jy beam}^{-1}$. Positive contours are solid while negative contours are dotted. There are no negative contours here.

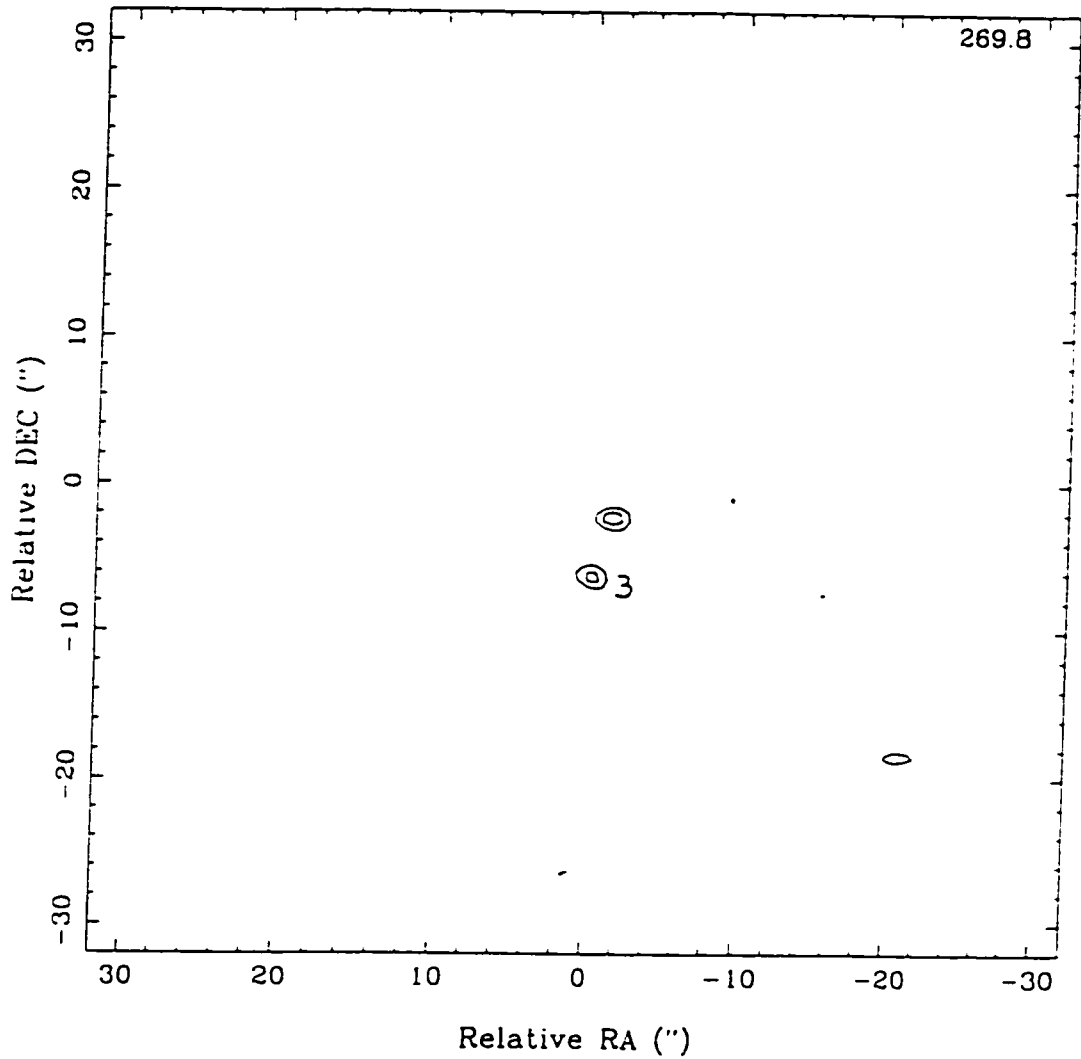


Figure 2.22: Optimum map of GMC 3 in NGC 5461. The contours have been plotted at the $\pm 3\sigma$ and $\pm 4\sigma$, where σ is $0.062 \text{ Jy beam}^{-1}$. Positive contours are solid while negative contours are dotted.

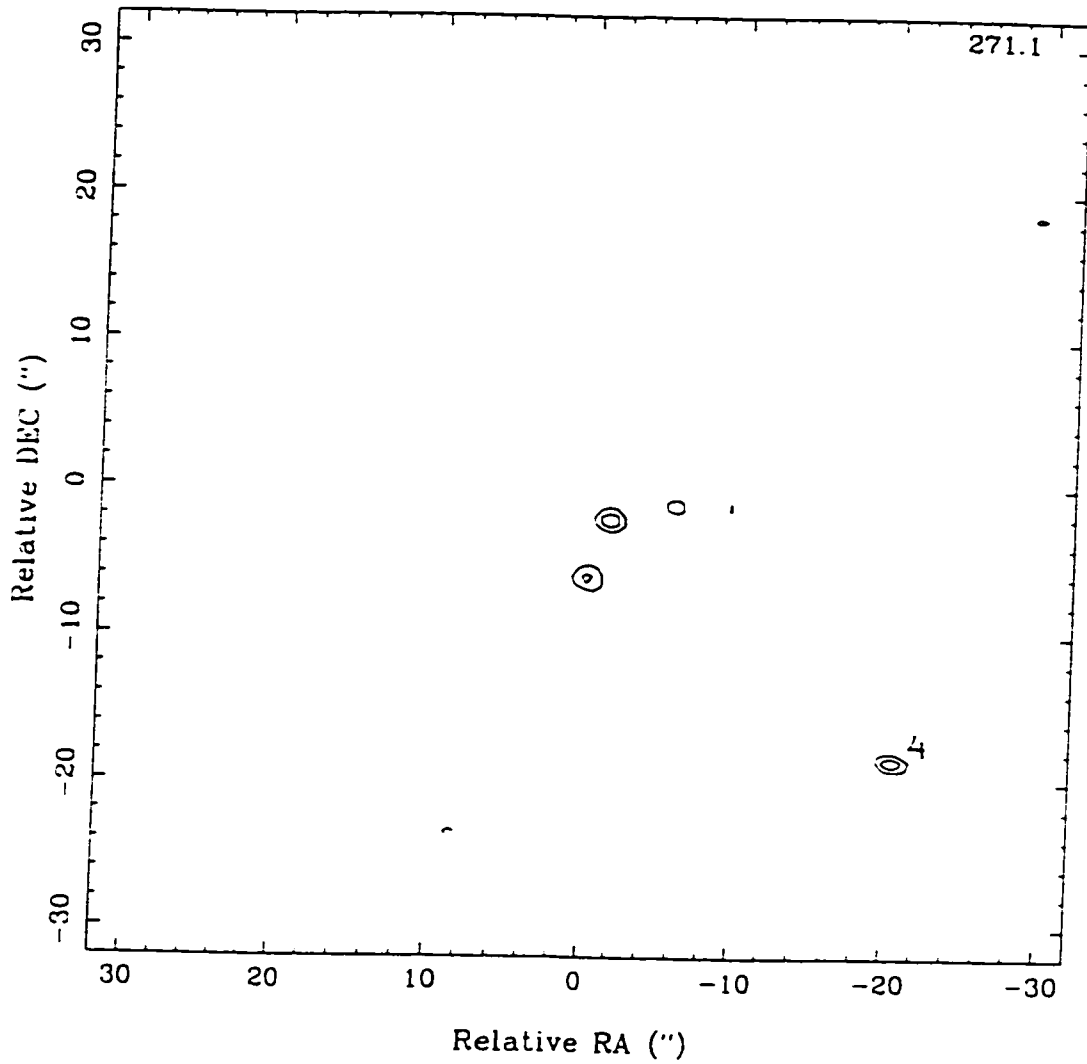


Figure 2.23: Optimum map of GMC 4 in NGC 5461. The contours have been plotted at the $\pm 3\sigma$ and $\pm 4\sigma$, where σ is $0.056 \text{ Jy beam}^{-1}$. Positive contours are solid while negative contours are dotted.

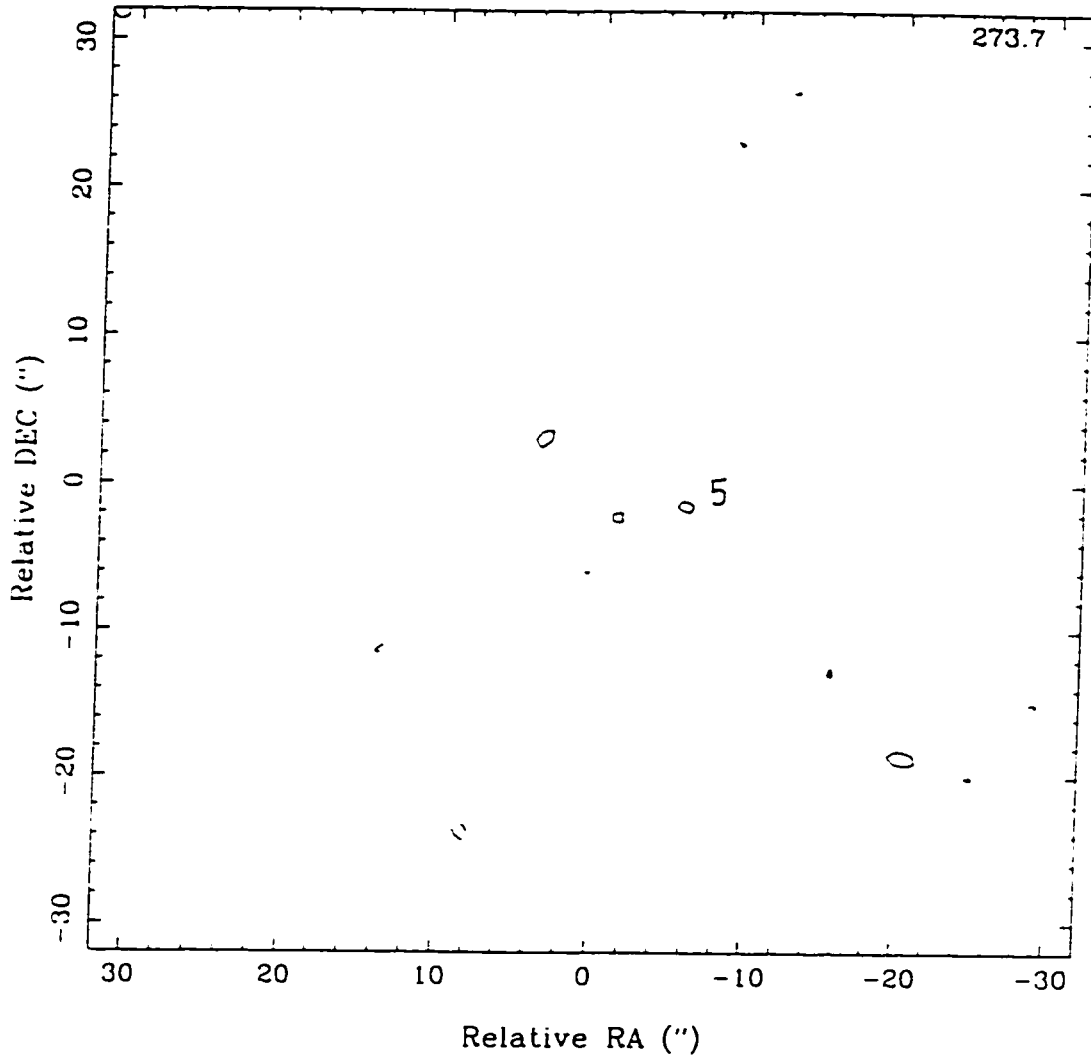


Figure 2.24: Optimum map of GMC 5 in NGC 5461. The contours have been plotted at the $\pm 3\sigma$ and $\pm 4\sigma$, where σ is $0.057 \text{ Jy beam}^{-1}$. Positive contours are solid while negative contours are dotted.

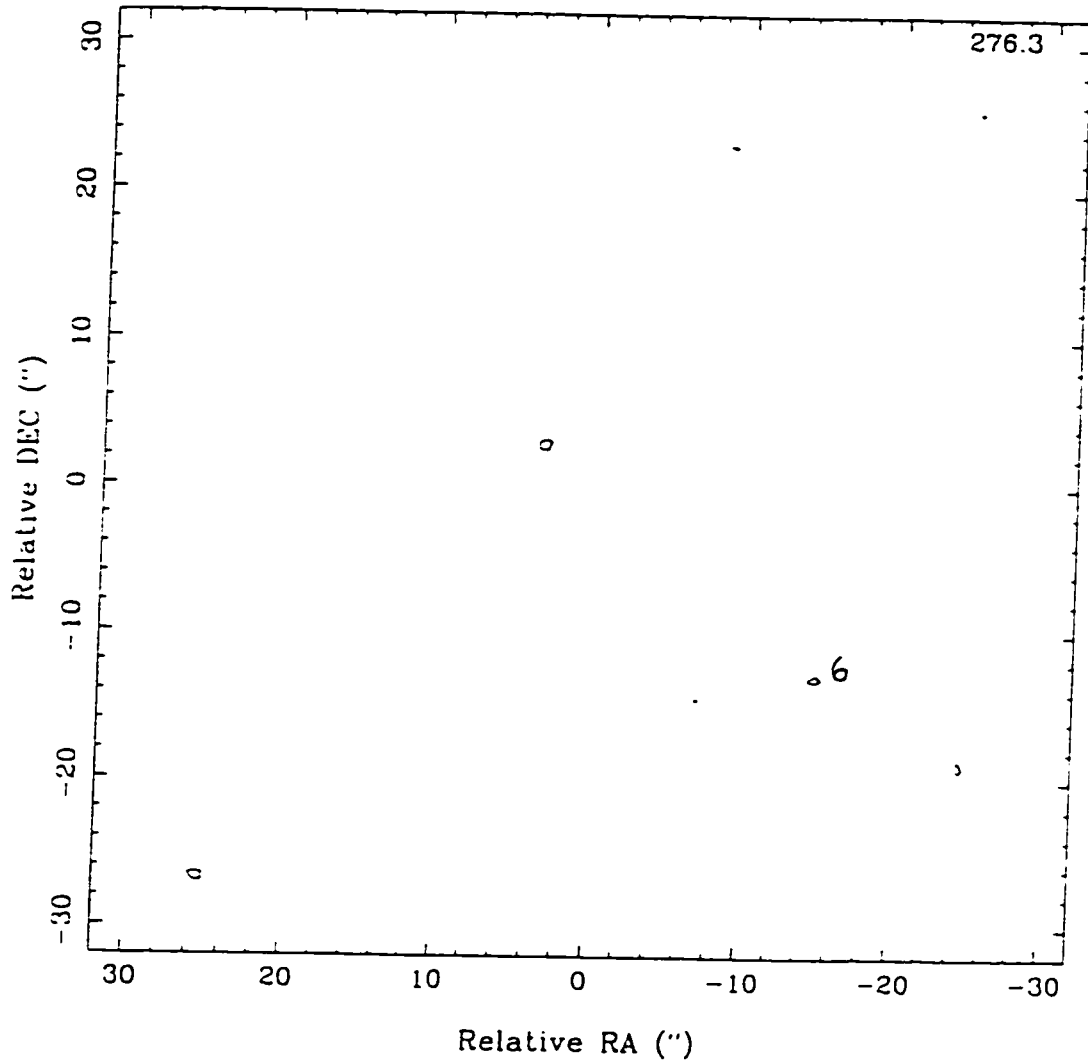


Figure 2.25: Optimum map of GMC 6 in NGC 5461. The contours have been plotted at the $\pm 3\sigma$ and $\pm 4\sigma$, where σ is $0.056 \text{ Jy beam}^{-1}$. Positive contours are solid while negative contours are dotted.

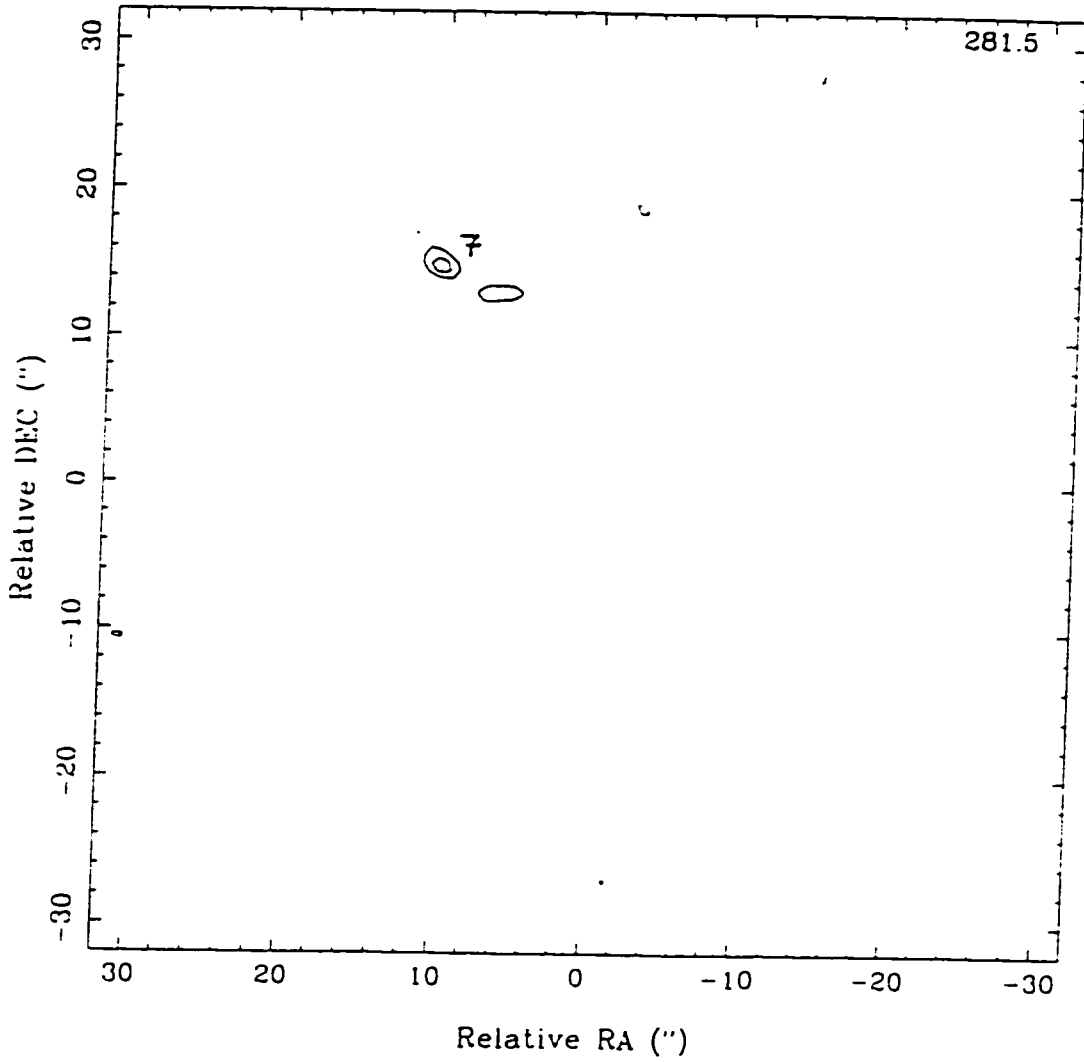


Figure 2.26: Optimum map of GMC 7 in NGC 5461. The contours have been plotted at the $\pm 3\sigma$ and $\pm 4\sigma$, where σ is $0.055 \text{ Jy beam}^{-1}$. Positive contours are solid while negative contours are dotted.

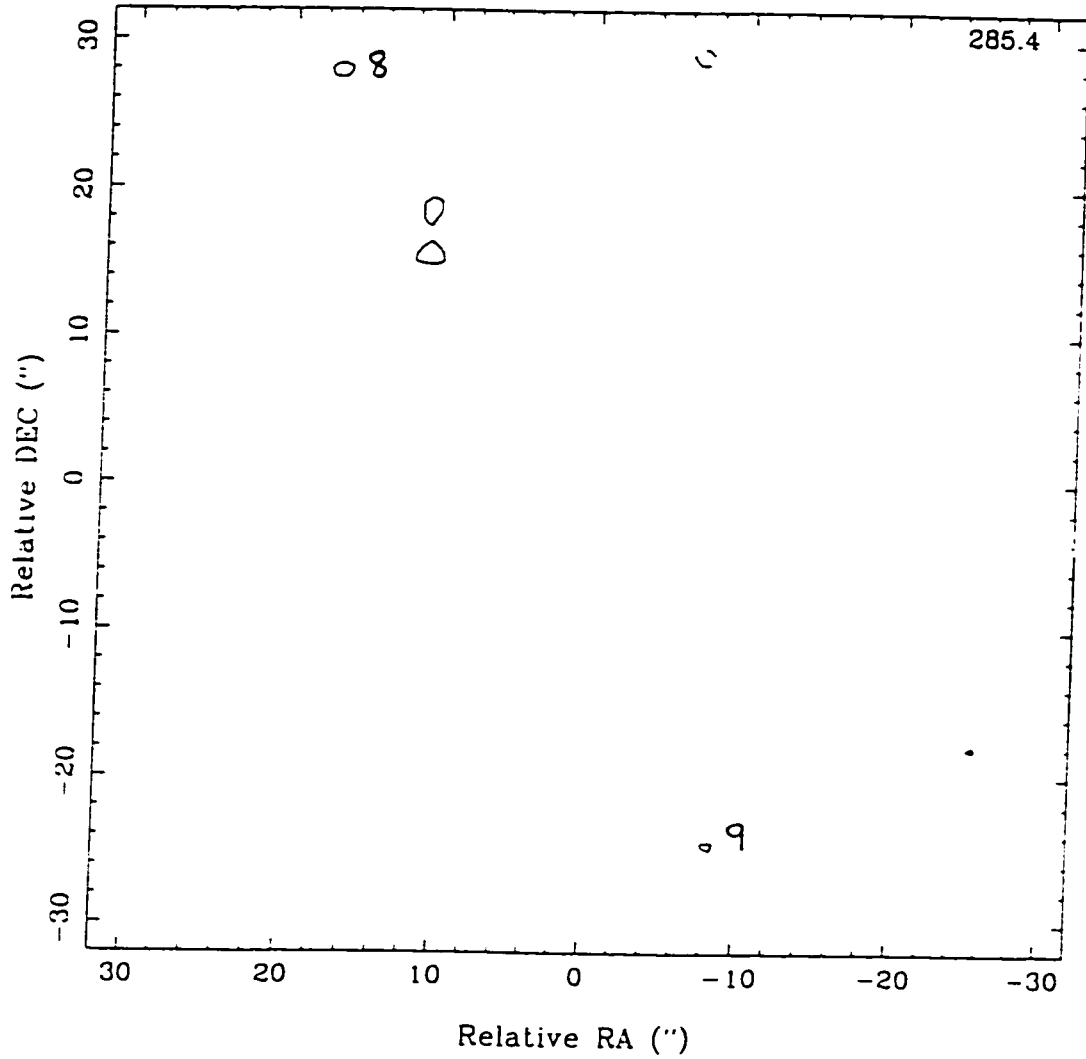


Figure 2.27: Optimum map of GMC 8 and GMC 9 in NGC 5461. The contours have been plotted at the $\pm 3\sigma$ and $\pm 4\sigma$, where σ is $0.064 \text{ Jy beam}^{-1}$. Positive contours are solid while negative contours are dotted.

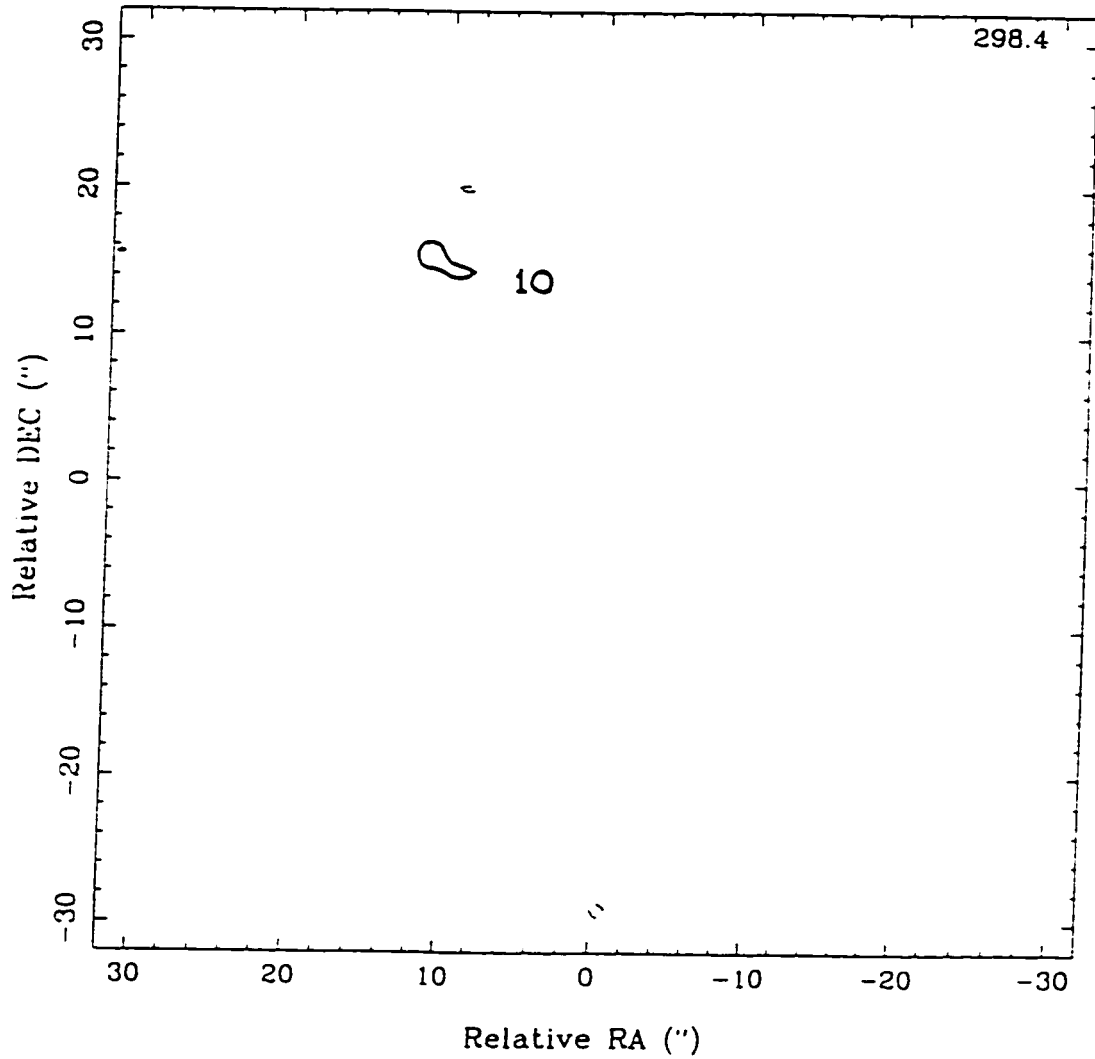


Figure 2.28: Optimum map of GMC 10 in NGC 5461. The contours have been plotted at the $\pm 3\sigma$ and $\pm 4\sigma$, where σ is $0.062 \text{ Jy beam}^{-1}$. Positive contours are solid while negative contours are dotted.

Cloud	Central Velocity (km s ⁻¹)	Dimensions (pc×pc)	Offset Position (".)	Δv (km s ⁻¹)	Total integrated flux (Jy km s ⁻¹)	T_B (K)
1	263	99 × 90	(19.20)	7.8	1.5 ± 0.5	3.4
2	270	108 × 90	(-2. -2)	10.4	4.4 ± 1.0	1.4
3	270	180 × 81	(0. -7)	5.2	1.9 ± 0.5	6.4
4	271	99 × 73*	(-21. -19)	7.8	1.7 ± 0.5	3.8
5	274	94* × 73*	(-6. -2)	7.8	1.2 ± 0.3	2.6
6	276	140 × 90	(-15. -13)	7.8	3.6 ± 0.9	8.0
7	282	126 × 81	(10.15)	7.8	2.6 ± 0.6	5.8
8	285	99 × 73*	(17.28)	5.2	1.0 ± 0.3	3.2
9	285	108 × 90	(-9. -25)	5.2	1.4 ± 0.4	4.6
10	298	180 × 90	(11.15)	5.2	2.2 ± 0.7	7.2

Table 2.15: Physical properties of GMCs in NGC 5461. The dimensions are not deconvolved from the beam (the deconvolved characteristic diameters appear in Table 4.2). Dimensions accompanied by an asterisk (*) are upper limits: the GMC has not been resolved. The offset positions are with respect to the centre of NGC 5461: $\alpha = 14^{\text{h}}01^{\text{m}}55^{\text{s}}.6$ and $\delta = 54^{\circ}33'31''.0$.

where there are two labels. GMCs 8 and 9 have the same velocity range.

To check the method chosen, I followed the same procedure for the negative peaks in the integrated map. If the method is sound, then there should be very few if any ‘detections’. Of the twenty-eight negative peaks in the integrated map, only two would be ‘confirmed’ by the two subsequent criteria. So the analysis used is fairly reliable as regards not mistaking noise for signal.

The analysis of the features in NGC 5462 will be considerably shorter than

that of the GMCs in NGC 5461 because the emission from NGC 5462 is weak (see Figure 2.29). In fact, the emission is so much weaker that there are no features that appear in consecutive channels at the 3σ level. Therefore, the best that can be accomplished is an upper limit for the flux from this region. If all the positive features are added, then the total flux from the region is 0.30 Jy, and the integrated intensity is 16 Jy km s^{-1} . The upper limit for the mass of NGC 5462 that results from this integrated intensity is consistent with the mass found from other methods (see Table 3.10).

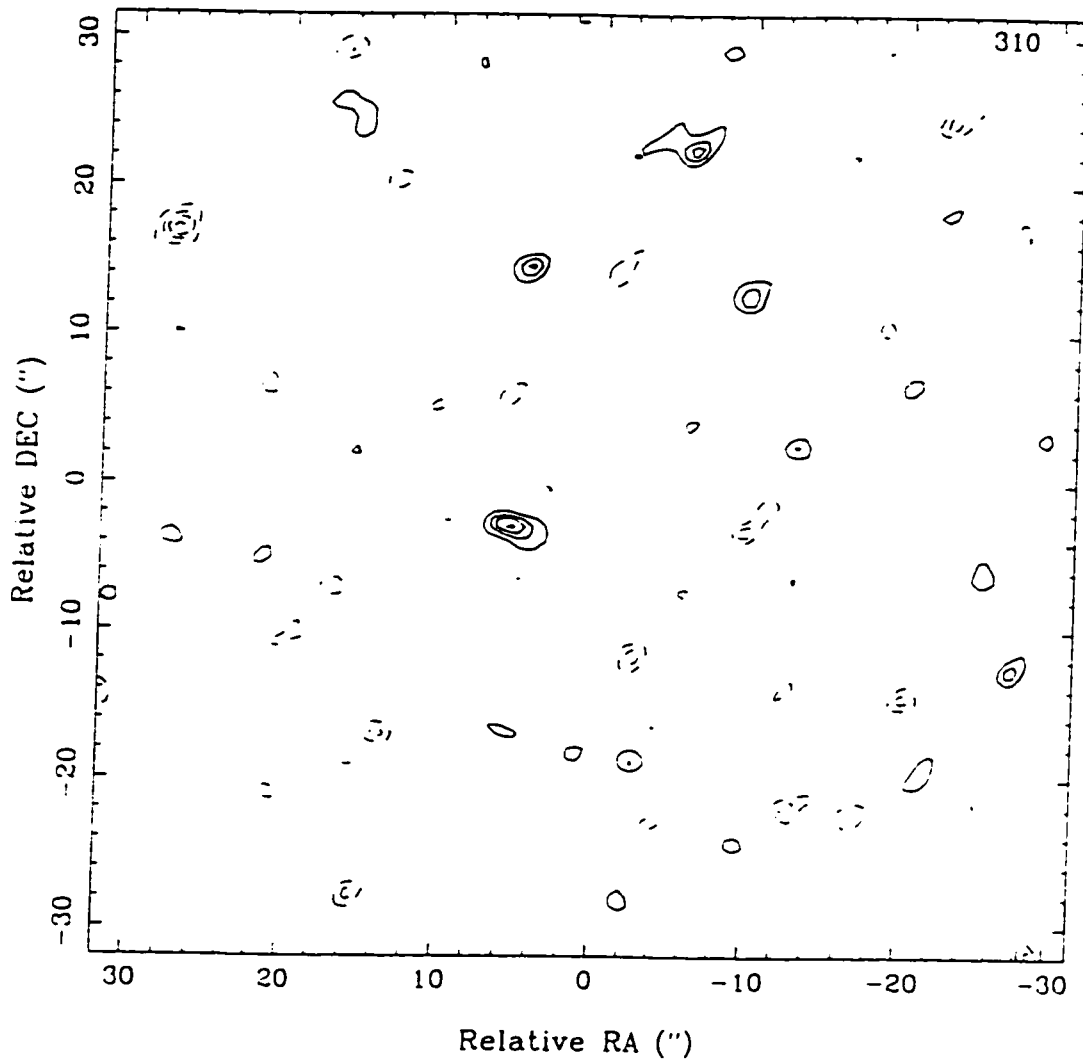


Figure 2.29: Integrated map of NGC 5462 over 52 km s^{-1} . The contours have been plotted at the $\pm 2\sigma$, $\pm 2.5\sigma$, $\pm 3\sigma$, $\pm 3.5\sigma$, and 4σ . Positive contours are solid while negative contours are dotted. The positive 'peaks' are accompanied by as many negative 'peaks', so I conclude that there are no real peaks in this map.

2.3 Summary of Observations

There are three giant H II regions and one normal H II region of M101 that have been studied to one degree or another in this thesis. NGC 5461 is the most massive and the one for which the most data are available: four transitions of CO from single-dish telescopes and one transition from an interferometer. NGC 5462, although detected in four wavelengths in single-dish observations, was not detected with the Owens Valley array. NGC 5471 was not detected with any of the JCMT observations, and yet it was detected in a lower transition ($J = 1 \rightarrow 0$) with the NRAO 12-meter telescope. Finally, the normal H II region, H660, was observed with the JCMT in three transitions of CO. These observations are analyzed and discussed in the following chapters.

Chapter 3

Analysis

A mass of interstellar gas emits a spectrum of radiation that is determined by the physical properties of the gas cloud: its temperature, mass, composition, etc. The spectrum of the *molecular* component of the gas cloud can be observed because, during the last three decades, sensitive receivers have been developed to observe astronomical emission lines of molecules such as CO. In addition, much theoretical work has been devoted to ‘inverting’ the observed spectrum to determine the physical properties of the gas cloud. Of particular interest—mostly because they are easily determined—are the column density and mass.

Several methods have been developed to calculate the column density and mass of the molecular gas; the method one chooses depends on the observations available and the anticipated conditions of the gas. Three methods are discussed here. The first method (the LTE method) estimates the optical depth and the column density

on the assumption that the gas is in *local thermodynamic equilibrium* (LTE). This technique is frequently used in studies of molecular outflows when a small number of emission lines have been observed. For the LTE analysis, I used the $J = 2 \rightarrow 1$ rotational emission lines of ^{12}CO and ^{13}CO that I observed at the JCMT.

The second method ('empirical' method) involves the assumptions that the gas is in gravitational equilibrium and that the mass of the gas is linearly proportional to the observed integrated flux density from the $^{12}\text{CO } J = 1 \rightarrow 0$ transition. Obviously, this technique requires the least amount of data: observations of a single emission line, $J = 1 \rightarrow 0$, which were observed with both the Owens Valley array and the NRAO 12-meter telescope. Finally, the third method (LVG method) finds the properties of the gas by assuming that the gas has a *large velocity gradient* (LVG), and, therefore, the Doppler-shift of the emission from one region will be large enough that the emission will be absorbed only by neighbouring molecules. This more robust technique requires at least four emission lines: therefore, all my observations at JCMT, NRAO, and Owens Valley are needed. In the present thesis, all three methods have been used.

Before presenting the three methods used in this thesis, I discuss the way in which one compensates for the fact that the data came from various telescopes with different beam sizes and characteristics. One changes all the observed quantities to a physical, telescope-independent quantity, namely the *radiation temperature*, which is the source temperature that a perfect antenna would measure at the top of the Earth's atmosphere. How to obtain the desired radiation temperature from the *antenna temperature*—the quantity observed at the telescope—is explained in

the section that follows. The second section (page 97) is on the LTE analysis, and the third section is on the empirical method (page 119). The LVG analysis is discussed in the fourth section (page 127) and is followed by a brief summary of the properties of the molecular gas near H II regions of M101 and a comparison of the results from the three methods (page 142).

3.1 Calculating the Radiation Temperature, T_R , from Observed Temperatures

Two methods discussed in this chapter—the LTE method and the empirical method for Owens Valley data—assume that from the observed temperature one can eventually obtain the radiation temperature: the temperature of the source that a perfect antenna would measure at the top of the Earth’s atmosphere. To calculate the radiation temperature, one needs the coupling efficiency, η_c —the efficiency with which the antenna diffraction pattern couples to the source (see page 183).

In particular, the LTE method requires the calculation of the excitation temperature, which depends on the radiation temperature (see equation 3.14). The mass from the empirical method for Owens Valley data, where the integrated intensity is in terms of flux density, depends on the radiation temperature and ultimately on the coupling efficiency (see equation 3.33). The complete definitions of the various quantities involved and detailed derivations are discussed in the Appendix. Here, the results will simply be presented.

Since the coupling efficiency depends on the source size and the beam size, different telescopes—even different transitions observed at the *same* telescope—will have different values for η_c . The coupling efficiency is calculated by numerical integration from equation (A.13) in the Appendix. The model used for the integration takes into account both the size (as determined from the high resolution Owens Valley data of NGC 5461) and the position of each GMC with respect to the centre

of each beam. To compute the total coupling efficiency, I added up the calculated coupling efficiencies of all the molecular clouds. This procedure was followed for the 12-meter telescope, the Owens Valley array, and the JCMT for the transitions $^{12}\text{CO } J = 2 \rightarrow 1$ and $^{12}\text{CO } J = 3 \rightarrow 2$ (the JCMT beams differ for the two transitions): the results are presented in Table 3.1.

The coupling efficiencies have been calculated with the assumption that the GMCs in NGC 5461 were resolved with the Owens Valley beam. The justification for this assumption is that the largest GMCs in the Milky Way have diameters of 100 pc (Sanders et al., 1985), which is comparable to the resolution of the Owens Valley data ($2''.3$ or 80 pc diameter at the distance of M101). It is possible, however, that the GMCs are in fact smaller.

The possibility of smaller cloud sizes is the main uncertainty in the calculation of the coupling efficiency. If, for example, the characteristic size of a cloud is 75% of the beam (or 60 pc diameter), then the value of η_c would be 55% of its original value. In Table 3.1, the estimated uncertainties for η_c have been included. If the GMCs are indeed much smaller, then the coupling efficiency could be an order of magnitude smaller, and this uncertainty would be the most severe of all the other uncertainties discussed in this thesis. There are indications, however, from the empirical method that the molecular clouds are probably not much smaller than the Owens Valley beam because the total molecular mass of NGC 5461 is the same within their uncertainties for the NRAO 12-meter data and for the Owens Valley data. The analysis of the NRAO 12-meter data does not require the coupling efficiency while the analysis of the Owens Valley data does.

Beam size	η_c
14" JCMT (345 GHz)	0.056 ± 0.024
20" JCMT (230 GHz)	0.037 ± 0.016
55" NRAO 12-meter telescope (115 GHz)	0.013 ± 0.006
2.3" Owens Valley millimeter array (115 GHz)	0.59 ± 0.22

Table 3.1: The coupling efficiencies with their uncertainties—as computed for NGC 5461—are presented: they are required to express the radiation temperature in terms of the observed corrected antenna temperature.

Furthermore, one has to assume that the coupling efficiency for the other giant H II regions are similar to NGC 5461 because no interferometric data for NGC 5462 or NGC 5471 are available. This assumption is probably not too bad because the values for the molecular mass obtained with the LTE method are within a factor of two or three from the values obtained from the empirical method, which does not utilize the coupling efficiency (see Table 3.10).

3.2 Calculation of the Physical Properties Assuming Local Thermodynamical Equilibrium (LTE)

The LTE method is frequently used to calculate the physical properties of molecular gas especially when isotopomers of CO or of other molecules such as CS and NH₃ have been observed [for example: Lada and Fich (1996), Giannakopoulou et al. (1997)]. The following theoretical arguments are fairly standard: see, for example, Spitzer (1978).

3.2.1 Optical Depth from LTE Method

In order to obtain information about the physical conditions of the molecular gas in M101, one needs to understand how the properties of the gas affect the radiative transfer. Light goes through the gas and, depending on the physical characteristics of the gas, the light will change in intensity and frequency. With the analysis that follows, one attempts to determine the properties of the gas from which the observed light came.

The most important quantity in this type of analysis is the intensity I_ν of the radiation of frequency ν . Assume that light moving in a vacuum is passing perpendicularly through some arbitrary surface area of size $d\sigma$ into a narrow cone of opening $d\omega$. The amount of energy per second going through the area is pro-

portional to $d\sigma$ and to the solid angle $d\omega$: the intensity is defined as the energy per second that flows through a unit surface area into a unit solid angle per unit frequency.

Now let the light pass through a *slab of gas* that has a total length of z and a cross section of $d\sigma$. The light travels along the length of the slab. The total energy that is absorbed or scattered when the photons move through the gas is proportional to the distance travelled, ds , and to the probability per unit length that a photon will be scattered or absorbed. This latter quantity is called *total opacity*, k_ν , and has units of cm^{-1} . Therefore, the initial radiation is diminished at some arbitrary length s in the slab by

$$dI_\nu^{\text{absorbed}} = -k_\nu(s) I_\nu(s) ds. \quad (3.1)$$

The slab also emits some radiation, which is given by the following equation:

$$dI_\nu^{\text{emitted}} = j_\nu(s) ds. \quad (3.2)$$

where j_ν , the *volume emissivity*, is the amount of radiation emitted by a unit of gas volume, per unit time, per unit frequency interval, and per unit solid angle. Combining equations (3.1) and (3.2), one obtains the intensity that has been emitted, absorbed, or scattered from the slab:

$$dI_\nu = j_\nu(s) ds - k_\nu(s) I_\nu(s) ds. \quad (3.3)$$

For the next step, it is assumed that the slab is uniform (isotropic and homogeneous): in other words, k_ν and j_ν do not depend on s . It should be pointed out here that this assumption is almost definitely not true for GMCs where there is star formation: however, the simplifying approximation might be appropriate when one considers that a single-dish beam is large enough to contain groups of GMCs, which are called molecular associations (Rand and Kulkarni, 1990), and that one observes the *average* properties of the clouds (Maloney and Black, 1988).

If equation (3.3) is multiplied by the integrating factor $e^{k_\nu s}$, the equation can be written as

$$d[e^{k_\nu s} I_\nu(s)] = j_\nu e^{k_\nu s} ds, \quad (3.4)$$

which, when integrated along the length of the cloud, z , becomes

$$e^{k_\nu z} I_\nu(z) - I_\nu(0) = \frac{j_\nu}{k_\nu} \int_0^{k_\nu z} e^{k_\nu s} d(k_\nu s). \quad (3.5)$$

The quantity $k_\nu z = \tau_\nu = \int_0^{k_\nu z} k_\nu ds$ in equation (3.5) is the *optical depth* of the gas, which determines the relative transparency of the gas. The optical depth is dimensionless: as it gets larger, the gas cloud is more opaque, whereas if the optical depth is much less than unity, the gas cloud is considered to be transparent. Equation (3.5) can be evaluated as a function of the optical depth: one finds

$$I_\nu(\tau_\nu) = I_\nu(0) e^{-\tau_\nu} + \frac{j_\nu}{k_\nu} (1 - e^{-\tau_\nu}), \quad (3.6)$$

where $S_\nu = \frac{j_\nu}{k_\nu}$ is called the *source function*. If the external radiation incident on

the slab. $I_\nu(0)$. is negligible, then the equation of transfer becomes

$$I_\nu(\tau_\nu) = S_\nu (1 - e^{-\tau_\nu}). \quad (3.7)$$

To simplify equation (3.7) further, one can make an additional assumption: even if the gas preferentially absorbs radiation in a small range of frequencies, the radiation it emits is distributed at all frequencies according to the Planck distribution of the intensity originating from a black body, B_ν (Bohm-Vitense, 1989). This condition is called local thermodynamic equilibrium (LTE). Under LTE, the source function is expressed as the intensity from a black body [$S_\nu = B_\nu(T_{ex})$] (Lang, 1980), where T_{ex} is the excitation temperature. The excitation temperature is defined as the characteristic temperature in the Boltzmann equation, which determines the number density of atoms at a given excitation level:

$$\frac{n_l g_u}{n_u g_l} = e^{h\nu/kT_{ex}}, \quad (3.8)$$

where h is the Planck constant, ν is the frequency of the $u \rightarrow l$ transition, k is the Boltzmann constant, n_l and n_u are the number densities for levels l and u respectively, and g_u and g_l are the statistical weights for those levels. If the gas were not in LTE, then the Boltzmann equation could be used but the excitation temperature would be different for each transition. In LTE, equation (3.7) reduces to

$$I_\nu(\tau_\nu) = B_\nu(T_{ex}) (1 - e^{-\tau_\nu}). \quad (3.9)$$

The observed intensity—the left-hand side of equation (3.9)—can be expressed in terms of the radiation temperature [see equation (A.4) in Appendix]:

$$I_\nu = \frac{2kT_R\nu^2}{c^2}. \quad (3.10)$$

Therefore, equation (3.9) yields

$$T_R = (1 - e^{-\tau_\nu}) \frac{h\nu/k}{e^{h\nu/kT_{ex}} - 1}. \quad (3.11)$$

In equation (3.11), there are three quantities that, in principle, can vary for different emission lines: the optical depth, τ_ν ; the transition frequency, ν ; and the excitation temperature, T_{ex} . For the case of isotopomers of the same molecule, however, the situation is simpler. For example, the transitions of $^{12}\text{CO } J = 2 \rightarrow 1$ and $^{13}\text{CO } J = 2 \rightarrow 1$ have very similar frequencies: 230 GHz and 220 GHz, respectively. This 5% difference can be easily ignored to facilitate the calculations that follow. Also, the two isotopomers have very similar energy levels and transition probabilities, so from the Boltzmann equation (3.8), the excitation temperatures for a given transition are roughly the same.¹ Taking into account the above assumptions, I calculate the ratio of the radiation temperatures for the two isotopomers as

$$\frac{{}^{12}T_R}{{}^{13}T_R} = \frac{1 - e^{-{}^{12}\tau_\nu}}{1 - e^{-{}^{13}\tau_\nu}}. \quad (3.12)$$

Although many properties of the isotopomers are similar, their abundances

¹If the gas is in LTE, then the excitation temperature is the same for all transitions.

are quite different: ^{12}CO is much more abundant than ^{13}CO . The exact ratio, $\psi = ^{12}\text{CO}/^{13}\text{CO}$, is somewhat uncertain because it may increase with the galactocentric distance (Langer and Penzias, 1990). The ratio has been measured to be as low as 24 at the centre of the Milky Way and as high as 79 at 12 kpc from the centre of our Galaxy. For the distance of the two giant H II regions from the centre of M101 (between 4 and 6 kpc), one would expect the most appropriate ratio to be at the lower end of the values.

This ratio of the abundances of the isotopomers is equal to the ratio of the optical depths of the isotopomers because the optical depth is proportional to the abundance: therefore, $^{12}\tau_\nu = \psi ^{13}\tau_\nu$. An additional consideration is that the radiation temperatures $^{12}T_R$ and $^{13}T_R$ vary with velocity (as seen from the observed spectra), so equation (3.12) should be written for clarity as

$$\frac{^{12}T_R(v)}{^{13}T_R(v)} = \frac{1 - e^{-\psi ^{13}\tau(v)}}{1 - e^{-^{13}\tau(v)}}. \quad (3.13)$$

From this equation, one can calculate the optical depth for a certain velocity interval. If the velocity interval chosen is the smallest one that can be resolved, then one can measure the radiation temperatures from the spectra (or equivalently the antenna temperatures: see page 111) for ^{12}CO and ^{13}CO . From equation (3.13) and an assumed value of ψ , one can calculate the optical depth for ^{13}CO and, therefore, the optical depth of ^{12}CO .

The calculation of the optical depth is a necessary step in the calculation of the excitation temperature; when the optical depth is calculated, it can be inserted

in equation (3.11), and the excitation temperature can be found. Since I have assumed that the gas is in LTE, the kinetic temperature is equal to the excitation temperature:

$$T_k = T_{ex} = \frac{h\nu}{k} \left(\ln \left(1 + \frac{h\nu}{k^{13}T_R(v)} (1 - e^{-13\tau(v)}) \right) \right)^{-1}. \quad (3.14)$$

It might seem odd that in equation (3.14) the excitation temperature depends on terms that are functions of velocity (or frequency), but the excitation temperature is not very sensitive to the value of $^{13}T_R$ or τ . The excitation temperature remains fairly constant—between 5 and 20 K—over the observed ranges for $^{13}T_R$ and τ .

These excitation temperatures are comparable to the average temperature in a quiescent GMC—a typical temperature of 10 K (Blitz, 1993). Low temperatures might seem strange in a star forming region where the stellar photons can heat the gas; however, the JCMT has a large beam (20") that looks at a vast region. The average excitation temperature is probably fairly low.

3.2.2 Column Density from LTE Method

On page 99, the optical depth has been defined as a measure of the transparency of gas and is given by

$$\tau_\nu = \int_0^z k_\nu ds. \quad (3.15)$$

The total opacity k_ν for a given transition between an upper level u and a lower level l can be expressed in terms of the Einstein coefficients² B_{lu} and B_{ul} as follows:

$$k_\nu = \frac{h\nu}{4\pi} (n_l B_{lu} - n_u B_{ul}). \quad (3.16)$$

where B_{lu} is the absorption coefficient, B_{ul} is the stimulated emission coefficient, and n_l and n_u are the number densities of the lower and upper level respectively. The Einstein B coefficients are not independent—the stimulated emission coefficient is linearly proportional to the absorption coefficient:

$$B_{ul} = \frac{g_l}{g_u} B_{lu}. \quad (3.17)$$

where g_l and g_u are the statistical weights of level l and u respectively.³ The statistical weight reflects the degeneracy of each rotation level, k : for linear molecules such as CO, the statistical weight can be expressed as $g_k = 2k + 1$ (Cohen-Tannoudji et al., 1977).

The spontaneous emission coefficient, A_{ul} , can be related to the stimulated

²There is some confusion in the literature about this expression because the exact formula depends on how the Einstein coefficients have been defined. In this thesis, I have decided to use the definition of Hummer and Rybicki (1971), who have used the intensity-based definition as opposed to the energy-density definition [see for example Bowers and Deeming (1984)].

³ l and u are integers with values, for example, $l = 1$ and $u = 2$.

emission coefficient by⁴ (Jefferies, 1968):

$$A_{ul} = \frac{2h\nu^3}{c^2} B_{ul}. \quad (3.18)$$

For linear molecules, this coefficient can be written as (Jefferies, 1968):

$$A_{ul} = \frac{64\pi^4\nu^3}{3hc^3} \mu^2 \frac{u}{g_u}. \quad (3.19)$$

where μ is the electric dipole moment of the molecule. If equations (3.16), (3.17), and (3.18) are substituted in equation (3.15), and if the gas is assumed to be in LTE, which allows the use of one of the forms of the Boltzmann equation (3.8), then the optical depth is given by

$$\tau_\nu = \frac{c^2}{8\pi\nu^2} \frac{g_u}{g_l} A_{ul} (1 - e^{-h\nu/kT_{ex}}) \int_0^z n_l(s) ds. \quad (3.20)$$

The integral in equation (3.20) is defined as the *column density for a given frequency range and rotational level*, $N_l(\nu) d\nu$: the column density is defined as the amount of material along the line of sight—a useful quantity to investigate because frequently the depth of the cloud is unknown. To determine the *integrated column density for a rotational level*, N_l , one must integrate the $N_l(\nu) d\nu$ over the frequency range of the line. Because the spectra are presented in terms of velocity ranges, one

⁴If the coefficients had been defined in terms of energy density, then the form of the equation (3.18) would be

$$A_{ul} = \frac{8\pi h\nu^3}{c^3} B_{ul}$$

must change from frequency ranges to velocity ranges using the Doppler formula: $d\nu = \frac{\nu}{c} dv$. The integrated column density for a rotational level l is

$$N_l = \int N_l(\nu) d\nu = \frac{\nu}{c} \int \int_0^z n_l(s) ds dv = \int \frac{8\pi \nu^3}{c^3 A_{ul}} \tau_\nu \frac{g_l}{g_u} (1 - e^{-h\nu/kT_{ex}})^{-1} dv. \quad (3.21)$$

The *total integrated column density* is needed in order to calculate the mass of the gas, so all rotational levels have to be taken into account. To obtain a relationship between the total integrated column density and the integrated column density for just one rotational level, I introduce in this discussion another form of the Boltzmann's equation (Lang, 1980):

$$\frac{N_l}{N_{13CO}} = \frac{g_l}{U} e^{-E_l/kT_{ex}}, \quad (3.22)$$

where N_{13CO} is the *total integrated ^{13}CO column density* for all rotational levels. U is the *partition function*, and E_l is the *excitation energy*,⁵ i.e., the energy of level l above the ground state. The partition function is defined as:

$$U = \sum_l g_l e^{-E_l/kT_{ex}}. \quad (3.23)$$

The excitation energy, $E_l = h B_r l(l+1)$, is linearly proportional to the *rotational constant*, B_r , that characterizes a given molecule. Equation (3.23) can be simplified

⁵It should be pointed out here that the excitation energy should not be confused with the energy difference between the upper level and the lower level $E_u - E_l = h\nu$.

if the sum is approximated by an integral so that the partition function is just

$$U = \frac{k T_{ex}}{B_r h}.$$

A more rigorous approach (Lee, 1992) gives a slightly different result:

$$U = \frac{k}{B_r h} \left(T_{ex} + \frac{h B_r}{3k} \right). \quad (3.24)$$

The correction factor is not important for high temperatures but is significant for low temperatures: for completeness, equation (3.24) will be used.

Now that the partition function has been introduced, the total integrated ^{13}CO column density, $N_{^{13}\text{CO}}$, can be obtained from equation (3.22) if equations (3.24), (3.21), and (3.19) are used:

$$N_{^{13}\text{CO}} = \frac{U N_l}{g_l} e^{E_l/k T_{ex}} = \frac{3k}{8 B_r \pi^3 \mu^2} \int \frac{e^{h B_r l(l+1)/k T_{ex}}}{(l+1)} \frac{\left(T_{ex} + \frac{h B_r}{3k} \right)}{1 - e^{-h \nu/k T_{ex}}} {}^{13}\tau_\nu dv. \quad (3.25)$$

In practice, one would first calculate the optical depth for a given velocity interval (channel), and use it to estimate the total column density $N(v_i)$ for that velocity interval. $N(v_i)$ is given by equation (3.25) evaluated for a given velocity band Δv —the $N(v_i)$ includes the measure Δv . The *integrated total column density* is calculated as the sum of all column densities for all velocity intervals where the optical depth can be estimated (i.e., for channels where ^{13}CO emission is detected). For example, if there are i channels and each channel has a column density integrated over its velocity width of Δv , then the total integrated column density will

be $N_{13CO} = \sum_i N(v_i)$.

In order to present equation (3.25) in a more user-friendly way. I substitute the constants and their units: the Boltzmann constant, k : the rotational constant for CO, $B_r = 5.764 \times 10^{10}$ Hz (Chantry, 1979); the electric dipole moment of CO, $\mu = 1.12 \times 10^{-19}$ esu cm (Chantry, 1979); and the Planck constant, h . In the previous constants there is a mix of unit systems: particularly awkward is the esu unit, a unit of charge: $\text{esu}^2 = \text{erg cm}$. For the rotational transition of ^{13}CO $J = 2 \rightarrow 1$ ($\nu = 220.3987$ GHz), equation (3.25) can be written as follows:

$$N_{13CO} = 1.16 \times 10^{14} \text{ cm}^{-2} \int e^{5.53 \text{ K} / T_{ex}} \frac{T_{ex} / \text{K} + 0.922}{1 - e^{-10.6 \text{ K} / T_{ex}}} {}_{13}\tau_\nu \left(\frac{dv}{\text{km s}^{-1}} \right). \quad (3.26)$$

Despite the fact that the integrated total column density depends on the excitation temperature in a non-linear fashion, at the relatively low temperatures that are of interest here, changes of the excitation temperature do not affect the value of the total column density significantly. The situation is different for the optical depth. The optical depth and, therefore, the column density are very sensitive to the small changes in the observed corrected antenna temperatures.

To ensure that the error analysis for the column density is done properly, I use a fairly robust, bootstrap method approach (Efron and Tibshirani, 1993). The program uses a Monte Carlo generator of many (in this case, $65536 = 2^{16}$) random pairs of values for $^{12}T_A^*$ and $^{13}T_A^*$ from two Gaussian populations: each estimated corrected antenna temperature is assumed to be drawn from a normal distribution about the measured temperature with a standard deviation obtained from the un-

certainty of the measurement. For each of the random pairs, the code calculates the column density per channel from equation (3.26). When all pairs are used, the program estimates the probability distribution for the column density per channel. From the characteristics of this distribution, one can obtain the uncertainty that is associated with the total column density. That the estimated probability distribution is obtained from sampled values is likely to introduce a small bias (Efron and Tibshirani, 1993), which is not considered.

For simplicity, the term ‘column density’ is used to mean total integrated column density in the rest of the text, and the term ‘column density per channel’ is the total column density integrated over one channel. The column density is calculated by summing the column density per channel for the channels of a given giant H II region. However, in the cases where the signal-to-noise ratio of the spectrum is low, only the channels with relatively high signal-to-noise ratios are considered in the calculation (for more details, see page 116).

3.2.3 Mass from LTE Method

Since the main constituent of the interstellar medium is molecular hydrogen, the ^{13}CO column density obtained above needs to be extrapolated to that of ^{12}CO , $N_{^{12}\text{CO}}$, which in turn will be converted to the H_2 column density, N_{H_2} . The values of the isotopomer ratio, ψ , and of the ratio of the column density of molecular hydrogen to the column density of CO are uncertain. Because of the wide range of values of the isotopomer ratio, the parameter is left in equation (3.28). Only at

the end of the LTE analysis do I adopt the value of $\psi = 20$ because the giant H II regions are fairly near the centre of M101 (see page 102).

In addition, the proportionality constant $N_{H_2} = 10^5 \times N_{^{13}CO}$ is used [see for example, Snell (1981)]. This ratio of column densities could be as low as 10^4 [e.g., Mitchell et al. (1995)], but the higher value was chosen because M101 has a lower metallicity than the Milky Way. The uncertainty in the adopted value introduces uncertainties of a factor of two in the determination of the mass of the GMCs.

The mass of the H_2 gas is found by multiplying the total H_2 column density, N_{H_2} , by the characteristic area (the beam or the source area—whichever is larger), A , and the mass of a hydrogen molecule m_{H_2} ; therefore, the molecular hydrogen mass is given by

$$M_{H_2} = N_{H_2} m_{H_2} A. \quad (3.27)$$

Finally, the fractional helium abundance (10% by number) should be taken into account in order to obtain the total mass of a GMC. Thus, the total molecular mass of a GMC in solar units is

$$M_{mol} = 2.18 \times 10^{-15} \mathcal{M}_{\odot} \times \frac{N_{^{13}CO}}{\text{cm}^{-2}} \times \frac{A}{\text{pc}^2} \times \psi. \quad (3.28)$$

3.2.4 Results from LTE Method

The LTE analysis described above requires the radiation temperature ratios of $^{12}CO/^{13}CO$. As is discussed in Appendix A, the radiation temperature is linearly

related to the corrected antenna temperature, T_A^* , which is the observed quantity (see Appendix equation A.17). In the special case of isotopomers, the observed frequencies are so similar that the forward spilling and scattering efficiency, η_{fss} (see page 183), and the coupling efficiency, η_c (see page 93) are essentially equal for ^{12}CO and ^{13}CO : therefore, the ratio of corrected antenna temperatures is equal to the ratio of radiation temperatures.⁶

These ratios have been observed toward two giant H II regions, NGC 5461 and NGC 5462, and one normal one, H660. Tables 3.2, 3.3, and 3.4 include, for each channel, the measured antenna temperatures for NGC 5461, NGC 5462, and H660 respectively. The first column of the tables lists the velocity at the centre of each channel, and all the channels have a width of 6.5 km s^{-1} because the observed emission lines have been smoothed to that velocity resolution. Since the lines are fairly wide, each emission line is at least four channels wide: NGC 5461, as the strongest source, has a line-width of six channels.

The emission lines are obviously not equally strong. But even for the same region, different channels can have quite different values for the measured corrected antenna temperatures as seen in the second and third column of Tables 3.2, 3.3, and 3.4. These corrected antenna temperatures are measured from the observed spectra (in Figures 2.1 to 2.10). The uncertainties quoted for the corrected antenna temperatures in the different regions vary because they depend on the observing conditions (system temperature and integration time), which change.

⁶Although the ratios are equal, one still needs the two efficiencies to calculate the excitation temperature (equation 3.14) from which one finds the column density.

Velocity of channel (km s ⁻¹)	¹² T _A [*] (mK) ±11	¹³ T _A [*] (mK) ±4	¹² T _A [*] / ¹³ T _A [*]	¹³ τ _ν	N _{13CO} per channel (10 ¹⁵ × cm ⁻²)
254	28.6	9.0	3.2 ± 1.4	0.378 0.24 – 0.81	6.0 2.7 – 14.6
261	80.2	8.0	10.0 ± 5.2	0.085 0.03 – 0.23	1.4 0.4 – 2.6
267	202.3	17.7	11.5 ± 2.7	0.066 0.04 – 0.11	1.7 1.3 – 2.3
274	221.7	15.4	14.4 ± 3.8	0.037 0.010 – 0.077	1.5 1.2 – 1.9
280	187.7	10.9	17.2 ± 2.2	0.016 0.003 – 0.032	1.0 0.7 – 1.5
287	114.2	9.0	12.7 ± 5.8	0.053 0.008 – 0.150	1.1 0.5 – 1.9

Table 3.2: LTE results for NGC 5461. The first column has the velocity of the centre of the channel: the second and third columns present the measured corrected antenna temperatures (with their uncertainties at the top of the column); the fourth column contains the ratios of antenna temperatures with their uncertainties; the fifth column gives the optical depth and its permitted range for each channel—the range is found by linear propagation of the uncertainties in columns 2 and 3; the last column lists the median value of the column density of ¹³CO and a range of values that span the equivalent of 1σ around the median value.

Velocity of channel (km s ⁻¹)	¹² T _A [*] (mK) ±7	¹³ T _A [*] (mK) ±2.5	¹² T _A [*] / ¹³ T _A [*]	¹³ τ _ν	N _{13CO} per channel (10 ¹⁵ × cm ⁻²)
290	49.0	0.9	54.4 [†]	0.003 [†]	0.2 0.1 – 9.7
297	34.8	6.1	5.7 ± 2.6	0.2 0.12 – 0.40	2.9 1.4 – 4.9
303	6.4	4.9	1.3 [†]	1.5 [†]	20.2 5.8 – sat [†]
310	8.3	1.6	5.1 [†]	0.2 [†]	6.2 1.0 – 38.4

Table 3.3: LTE results for NGC 5462. The numbers that are accompanied by daggers (†) are very uncertain due to a low signal-to-noise ratio. The first column has the velocity of the centre of the channel; the second and third columns present the measured corrected antenna temperatures (with their uncertainties at the top of the column). The fourth column contains the ratios of antenna temperatures, and the fifth column gives the optical depth; there is only one channel in NGC 5462 with a good enough signal-to-noise ratio in both spectra to estimate the uncertainty in the ratio and the optical depth. The last column lists the median value of the column density of ¹³CO and a range of values that span the equivalent of 1σ around the median value. For the third channel, the upper limit cannot be determined because the line is saturated; see page 116.

Velocity of channel (km s ⁻¹)	¹² T _A [*] (mK) ±7	¹³ T _A [*] (mK) ±2.5	¹² T _A [*] / ¹³ T _A [*]	¹³ τ _ν	N _{13CO} per channel (10 ¹⁵ × cm ⁻²)
208	62.6	13.5	4.6 ± 1.7	0.24 0.17 – 0.42	3.7 2.8 – 4.7
215	171.4	21.8	7.9 ± 1.6	0.12 0.09 – 0.17	2.6 2.2 – 2.9
221	202.6	16.2	12.5 ± 3.4	0.055 0.03 – 0.10	1.5 1.3 – 1.9
228	106.1	8.7	12.2 ± 6.2	0.058 0.009 – 0.18	1.1 0.6 – 1.6

Table 3.4: LTE results for H660. The first column has the velocity of the centre of the channel; the second and third columns present the measured corrected antenna temperatures (with their uncertainties at the top of the column); the fourth column contains the ratios of antenna temperatures with their uncertainties; the fifth column gives the optical depth and its permitted range for each channel—the range is found by linear propagation of the uncertainties in column 2 and 3; the last column lists the median value of the column density of ¹³CO and a range of values that span the equivalent of 1σ around the median value.

The fourth column in these Tables (3.2 to 3.4) presents the dimensionless ratios of antenna temperatures (or radiation temperatures in this case)—these ratios are used to calculate optical depths. The uncertainties for the ratios quoted in the fourth column are due to the propagation of uncertainties in the measurement of the corrected antenna temperatures. For channels of NGC 5462 where the signal is comparable to the noise, the ratios and optical depths in Table 3.3 are noted with a dagger and are considered uncertain.

The fifth column includes the optical depth, $^{13}\tau$: one cannot get a closed form solution for the optical depth as can be seen from equation (3.13): I used Newton's method to find the roots of equation (3.13). For completeness, I checked the behaviour of the first derivative of the function and found that the equation has only one possible real root for temperature ratios between 1 and ψ .

The uncertainty of the optical depth results from the range of possible values that the ratio of antenna temperatures can have. There are two limits in which one cannot calculate the optical depth. The first limit is for antenna temperature ratios that are larger than the isotopomer ratio, ψ . In this limit, the optical depth must be very small, and, therefore, the contribution to the column density will be insignificant too.

The second limit, when the antenna temperature of ^{13}CO is higher than that of the ^{12}CO , is trickier. This limit is a concern only for NGC 5462 (see Table 3.3). When the antenna temperature of ^{13}CO is higher than that of the ^{12}CO , equation (3.13) does not have real solutions. If these small values of the ratio are not

due to the low signal-to-noise ratio, then a physical explanation is that the emission line is saturated, i.e., the gas is so dense that gas closer to the observer is absorbing the CO emission from molecules on the far side of the cloud. Although the possibility of a saturated emission line cannot be eliminated, the NGC 5461 data—of considerably higher quality—show no such tendency, and there is no indication that the masses of the clouds in the two regions are significantly different (see Table 3.10). In this limit, therefore, I assume that the problematic cases occur for channels with low signal-to-noise ratios, and I ignore these data in the final calculation of the total mass, which then yields a lower limit to the mass of NGC 5462. I indicate that the upper limit of the column density per channel of the third channel in NGC 5462 might be saturated.

The column density per channel is in the sixth column of Tables 3.2 to 3.4. Because the uncertainty in the optical depth is significant, and the column density depends linearly on the optical depth, a Monte Carlo approach was used to calculate the uncertainty of the column density (see page 108). The values presented in Tables 3.2 to 3.4 are the median accompanied by the range that contains 68% of the randomly generated data (the equivalent of a standard deviation for a Gaussian distribution).

To obtain the column density N_{13CO} for each region, one must sum the column densities per channel over all channels. Because the uncertainties of the measured antenna temperatures are so high (especially for NGC 5462), there is a criterion established to choose the appropriate channels for the calculation of the total column density. The chosen restrictions are to use a channel if the peak ^{12}CO signal is

Source	^{13}CO column density ($\times 10^{15} \text{ cm}^{-2}$)	Masses ($\times 10^6 \mathcal{M}_{\odot}$)
NGC 5461	6.7 [4.1 - 10.2]	120 [70 - 180]
NGC 5462	2.9 [1.4 - 4.9]	50 [25 - 90]
H660	8.9 [6.9 - 11.1]	160 [120 - 200]

Table 3.5: Total ^{13}CO column densities and molecular masses calculated with the LTE method for the three observed H II regions. The centre of the NGC 5461 is the centre of position NGC 5461a while the centre of NGC 5462 is the centre of NGC 5462g. The column density and mass for NGC 5462 are lower limits because its spectra had low signal-to-noise ratios, and only one channel was used.

at least 3σ , and the peak ^{13}CO is at least 2σ . These criteria result in a lower limit for the value of the column density (and consequently of the mass) of NGC 5462, which has only one channel that meets the restrictions. The results are presented in Table 3.5.

The column density can be used to obtain the total molecular mass for the three regions. The column density for the molecular gas is entered in equation (3.28) to obtain the masses, which are also presented in Table 3.5. The masses are much larger than Galactic GMCs, which have typical values of $10^5 \mathcal{M}_{\odot}$ (Blitz, 1993). These large masses are expected from regions as large as 700 pc ($20''$), which would contain an association of GMCs.

The accuracy of the mass calculation depends on many parameters: on the un-

certainty in the distance to M101 because the conversion of arcseconds to parsecs has been folded in to equation (3.27) and, therefore, equation (3.28); the uncertainties in the abundance ratio of CO to molecular hydrogen (factor of two) and of the isotopomer ratio (factor of two): the uncertainty in the value of the column density of ^{13}CO , $N_{^{13}\text{CO}}$; and, finally, the uncertainty of the coupling efficiency, η_c , which also is on the order of a few.

3.3 Molecular Mass from the Empirical Method

In this section, the second method of analysis of CO emission data is presented. This method is an empirical approach to calculate the mass of the molecular gas from the column density of molecular hydrogen, N_{H_2} . The column density can be calculated if one uses a method based on data that suggest the column density of hydrogen is linearly proportional to the observed radiation temperature integrated over the emission line of $^{12}\text{CO } J = 1 \rightarrow 0$ [e.g., Sanders and Scoville (1987) and Digel et al. (1997)]. The constant of proportionality, X , is given by (Bronfman et al., 1988)

$$X = \frac{N_{H_2}}{\int T_R^* dv}. \quad (3.29)$$

Note that the integrated quantity is T_R^* , which is the observed quantity at the 12-meter telescope (as opposed to the observed quantity T_A^* at the JCMT). It is called 'empirical' because there is no obvious theoretical reason for the column density of hydrogen to have the same constant of proportionality with respect to the integrated intensity for individual clouds in different parts of the Galaxy (or, even more so, in other galaxies). This approach might be more suitable for ensembles of clouds because the *averaged* physical properties might be similar (Maloney and Black, 1988).

Although studies have shown that the X_{Gal} factor for the Galaxy is fairly constant, it is not argued here that its value is agreed upon or that its value may not change under certain circumstances. The range found in the literature for X_{Gal} is between $(1 - 12) \times 10^{20} \text{ cm}^{-2} (\text{K km s}^{-1})^{-1}$ [Digel et al. (1997) and references

therein]. I assume a value of $X_{Gal} = 3 \times 10^{20} \text{ cm}^{-2} (\text{K km s}^{-1})^{-1}$, which is in the middle of the range. One consideration is that regions with extreme star formation may have smaller values of X (Scoville and Sanders, 1987): M101 is a fairly normal spiral galaxy with no extreme star formation.

On the other hand, M101 is relatively metal-poor compared to the solar neighbourhood (Evans, 1986; Torres-Peimbert et al., 1989): a measure of the metallicity is given by the logarithm of the ratio of the density of oxygen to the density of hydrogen, $\log(\text{O}/\text{H})$. Furthermore, the metallicity drops as the distance from the centre of M101 increases. Galaxies with lower metallicity than that of the Milky Way have higher values of X than X_{Gal} (Wilson, 1995):

$$\log \frac{X}{X_{Gal}} = (5.95 \pm 0.86) - (0.67 \pm 0.10)[12 + \log(\text{O}/\text{H})]. \quad (3.30)$$

The value of $[12 + \log(\text{O}/\text{H})]$ for NGC 5461 is 8.39 ± 0.08 while for NGC 5471 is 8.05 ± 0.05 (Torres-Peimbert et al., 1989). The value of X determined by equation (3.30) for NGC 5461 is more than double X_{Gal} , and the value of X for NGC 5471 is almost four times more than the Galactic value.

The uncertainties of these estimates are severe because the expression is logarithmic: for example, the value of X for NGC 5461 could be in the range of $(0.3 - 15) \times X_{Gal}$. I use here the value of $X_{NGC\ 5461} = 6 \times 10^{20} \text{ cm}^{-2} (\text{K km s}^{-1})^{-1}$ for NGC 5461, NGC 5462, and H660 because they have similar metallicities. For NGC 5471, I use the value $X_{NGC\ 5471}$ of $12 \times 10^{20} \text{ cm}^{-2} (\text{K km s}^{-1})^{-1}$. This parameter, unfortunately, introduces an uncertainty in the final mass of at least a

factor of a few.

Once the value of X has been established, the hydrogen column density can be obtained from equation (3.29). One can deduce the total molecular mass in a similar fashion as described on page 110:

$$M_{mol} = 1.36 m_{H_2} A X \int T_R^* dv. \quad (3.31)$$

where the 1.36 factor is the factor that accounts for the presence of He. A is the area of the beam, and T_R^* is the quantity given at the NRAO 12-meter telescope. When the constants are substituted, the total molecular mass (in solar units) is

$$M_{mol} = 6.67 \mathcal{M}_\odot \times \frac{A}{\text{pc}^2} \times \frac{X}{6 \times 10^{20} \text{ cm}^{-2} (\text{K km s}^{-1})^{-1}} \times \int \frac{T_R^*}{\text{K}} \frac{dv}{\text{km s}^{-1}}. \quad (3.32)$$

This equation can also be written in terms of flux density,⁷ S_ν , if the radiation temperature is expressed in terms of the flux density—as it is for the Owens Valley millimeter array. To change equation (3.32), one must convert the observed T_R^* to the radiation temperature scale T_R : therefore, one needs to calculate the elusive quantity η_c (see page 93). When the conversion is done, the flux density can be expressed as the product of the solid angle of the source and the intensity of the source. The solid angle of the source is given by the ratio A/d^2 , where A is the area of the source and d is the distance between the source and the observer. If the radiation temperature is replaced with its definition in terms of intensity [see

⁷To distinguish the symbol for the flux density, S_ν , from the source function, \mathcal{S}_ν , I have used the calligraphic font for the source function.

equation (A.4) in Appendix], then the molecular hydrogen mass is

$$M_{H_2} = m_{H_2} X \eta_c \frac{c^2 d^2}{2k \nu^2} \int S_\nu dv \quad (3.33)$$

The total molecular mass in solar units can be expressed from equation (3.33) if the factor of 1.36 is included to account for helium. The formula for the total molecular gas in terms of the integrated flux density is needed only for the Owens Valley millimeter array observation of NGC 5461: therefore, in the following equation, the appropriate η_c value for NGC 5461 has been used (see Table 3.1).

$$M_{mol} = 1.89 \times 10^4 \mathcal{M}_\odot \frac{X}{6 \times 10^{20} \text{cm}^{-2} (\text{K km s}^{-1})^{-1}} \frac{\eta_c}{0.59} \left(\frac{d}{\text{Mpc}} \right)^2 \int \frac{S_\nu}{\text{Jy}} \frac{dv}{\text{km s}^{-1}}. \quad (3.34)$$

Equation (3.34) is in agreement with the formula published in Wilson et al. (1988) if one takes into account the different η_c and X that were used.

3.3.1 Results from the Empirical Method

I obtained $^{12}\text{CO } J = 1 \rightarrow 0$ data from the 12-meter telescope toward NGC 5461, NGC 5462, and NGC 5471. From the integrated corrected radiation temperature (see Table 3.6), one can calculate the molecular hydrogen column density using equation (3.29). As discussed before (see page 120), the X factor for the NGC 5461 and NGC 5462 will be $6 \times 10^{20} \text{ cm}^{-2} (\text{K km s}^{-1})^{-1}$, and NGC 5471 has a value for X of $12 \times 10^{20} \text{ cm}^{-2} (\text{K km s}^{-1})^{-1}$.

The molecular hydrogen column density can, in turn, be used to calculate the

total molecular mass from equation (3.32), where A is measured based on the 12-meter telescope beam size of $55''$. Table 3.6 contains the total molecular masses. One finds that the mass of the molecular gas associated with NGC 5461 is greater than the masses associated with the other two H II regions. Although the calculations indicate that NGC 5462 has a slightly greater molecular mass than NGC 5471, their allowed values are the same within their uncertainties. The uncertainties in the total molecular mass result from the uncertainty in the integrated radiation temperature—the systematic (potentially more significant) uncertainty in the value of X has been ignored.

For NGC 5461, higher resolution $^{12}\text{CO } J = 1 \rightarrow 0$ data were obtained with the Owens Valley millimeter array than with the 12-meter telescope data. The output from the interferometer, after calibration and cleaning, is the integrated flux density, $\int S_\nu dv$; therefore, the molecular mass can be obtained from equation (3.34) if the coupling efficiency of 0.59 ± 0.22 for the Owens Valley array (Table 3.1) is used. The integrated flux density was measured from the integrated map over a velocity range of 52 km s^{-1} of $^{12}\text{CO } J = 1 \rightarrow 0$ emission. The value for the integrated flux density is $(33 \pm 13) \text{ Jy km s}^{-1}$, which corresponds to $(3.4 \pm 1.4) \times 10^7 \mathcal{M}_\odot$.

This result from the Owens Valley millimeter array agrees within the uncertainties with the mass obtained from the single dish data (12-meter telescope). Since both methods yield similar masses, one does not have to evoke the presence of a constant, broadly distributed contribution to the intensity which would have been undetected by the interferometer [see, for example, Wilson and Scoville (1990)]. The reason for this potential flux loss is that there is a physical limit on how com-

compact a configuration can be. The more compact configurations of the antennas result in lower resolution data, so there is an *upper* limit to the size of a detectable feature.

After examining the total flux from the entire Owens Valley map, I use the same equation (3.34) to calculate the masses of the individual GMCs (see Table 3.7). The individual features in NGC 5461 have masses of $(10 - 44) \times 10^5 \mathcal{M}_{\odot}$ and are much greater than the masses of the GMCs in the Milky Way, which have masses typically around $10^5 \mathcal{M}_{\odot}$. The difference could be even more pronounced since the masses of the clouds in NGC 5461 are lower limits (the X factor has probably been underestimated). The large mass of the clouds in NGC 5461 might be the key to the presence of giant H II regions in M101: massive clouds have a very high probability to give birth to bright stars. Further discussion on this issue is presented in Section 4.2.1.

It is useful to compare the sum of the GMC masses in NGC 5461 (from Table 2.15 on page 86) with the total mass of the NGC 5461 association as observed with the single-dish 12-meter telescope (see Table 3.6 on page 125). The sum of the GMCs is $22 \times 10^6 \mathcal{M}_{\odot}$ while the single-dish value of the total mass is $50 \times 10^6 \mathcal{M}_{\odot}$. The discrepancy probably indicates that there are GMCs with smaller velocity widths or smaller fluxes that could not be detected.

Source	$\int T_R^* dv$ K km s ⁻¹	Masses ($\times 10^6 \mathcal{M}_\odot$)
NGC 5461	2.50 ± 0.48	50 ± 10
NGC 5462	0.84 ± 0.27	17 ± 6
NGC 5471	0.54 ± 0.20	11 ± 4

Table 3.6: Molecular masses for the three observed H II regions calculated from 12-meter telescope data (¹²CO $J = 1 \rightarrow 0$) with the empirical method.

GMC Number	$\int S_\nu dv$ (Jy km s ⁻¹)	Masses ($\times 10^5 \mathcal{M}_\odot$)
1	1.5 ± 0.5	15 ± 5
2	4.4 ± 1.0	44 ± 10
3	1.9 ± 0.5	20 ± 5
4	1.7 ± 0.5	18 ± 5
5	1.2 ± 0.3	12 ± 3
6	3.6 ± 0.9	37 ± 9
7	2.6 ± 0.6	27 ± 6
8	1.0 ± 0.3	10 ± 3
9	1.4 ± 0.4	14 ± 4
10	2.2 ± 0.7	23 ± 7

Table 3.7: The integrated flux density and the empirically calculated molecular mass are presented for each GMC in NGC 5461 (see Figure 2.14). The uncertainties in the mass take into account only the uncertainty in the measurement of the integrated flux—not the uncertainty in the coupling efficiency or the uncertainty in the X factor.

3.4 Calculation of the Physical Properties of Gas with a Large Velocity Gradient (LVG)

In sections 3.2 and 3.3, I have discussed two methods, relying on simple assumptions, for obtaining the mass of the molecular gas near H II regions in M101. The third approach, the LVG analysis presented in this section, is more rigorous in dealing with the transfer of radiation.

There are two extreme non-LTE approaches in dealing with the radiative transfer problem. One approach to this problem is to assume that there is no global motion: all the emission is a result of small-scale thermal motions and turbulence. The second approach is to assume that the gas cloud has a large velocity gradient, which means that the CO emission from one part of the cloud will be Doppler-shifted to a frequency that will not be re-absorbed by gas in other parts of the cloud (Scoville and Solomon, 1974). Under these conditions, the emission from a molecule will only be absorbed by neighbouring molecules, and the radiative transfer can be solved locally (Goldreich and Kwan, 1974). The first approach is called the microturbulence method, and the second approach is called the LVG method.

One potential problem with both these two methods is that they assume that all the emission comes from just one cloud. They do not treat the case in which there is more than one cloud in the line of sight with similar velocity. Fortunately the galaxy M101 is face-on, so it is unlikely that there are other clouds behind the clouds that are identified in this thesis.

The two non-LTE approaches typically produce results that agree within the errors of the methods, which are a factor of three due to uncertainties in geometry (White, 1977). Since the outcome of the models is sensitive to the geometry, I have used just one non-LTE method, the LVG method, to compare with the LTE analysis (White, 1977; Hasegawa et al., 1991).

If one can assume that the large velocity gradient assumption holds, it is proven that the integrated intensity over the entire line depends only on the local value of the source function, S_ν , the local probability of the photon escaping, and the external continuum flux that hits the cloud (Goldreich and Kwan, 1974). It is possible with numerical methods to solve the equation of transfer and the equation of statistical equilibrium⁸ locally. LVG codes are not easy to write because many complicated physical processes are taken into account (Lang, 1980); therefore, in the literature one frequently finds papers based on LVG codes that were written by a third party [some examples of such papers are Wang et al. (1993); Welch et al. (1996); Wilson et al. (1997)].

To estimate the physical conditions in the GMCs of M101, I have used the LVG code written by Jessica Arlett and Lorne Avery (1996) for a spherical, uniform cloud. The LVG code includes the FORTRAN programs `cotr` and `cotriso`. The purpose of these programs is to compute the radiation temperatures of various transitions of CO for a grid of kinetic temperatures T_k , abundances ζ , and densities

⁸Statistical equilibrium is the situation where one can assume that the number of transitions per unit volume per second into a given energy level should equal statistically the number of transitions out of this level.

n_{H_2} . The abundance parameter⁹ is defined as $\zeta = (N_{CO}/N_{H_2})/(dV/dR)$. The `cotr` program computes the radiation temperatures for the transitions of CO while the `cotriso` program computes them for a given isotopomer of CO (in this case, ^{13}CO). By taking the ratios of these radiation temperatures, one can easily calculate the line ratios: by comparing the theoretical ratios to those observed, one can deduce the most likely values for the kinetic temperature, abundance, and density.

The programs `cotr` and `cotriso` take as input the following: (1) the minimum, maximum, and step for the kinetic temperature grid; (2) the minimum, maximum, and logarithmic step for the abundance; and (3) the minimum, maximum, and step for the density. In addition, `cotriso` requires the isotopomer ratio of $^{12}CO/^{13}CO$. For each value of kinetic temperature, abundance, and density, the program outputs the theoretical radiation temperatures.

The procedure used in `cotr` and `cotriso` is briefly described. The main subroutine calculates the collisional rate coefficients from the lower level to the upper level with the assumption of balanced emission between the two levels. The collisional coefficient rates from the upper to the lower level are given in the literature for certain temperatures (Flower and Launay, 1985). The program has to interpolate for other temperatures. After this procedure has been completed, the main subroutine of `cotr` calculates the population of each energy level and the excitation temperature and radiation temperature for each line.

After all the parameters have been calculated in the table, the user can compare

⁹I refer periodically to the ζ parameter as abundance in the text so that the reader is reminded of what the Greek letter symbolizes.

the theoretical values of the radiation temperature derived from the LVG model with those observed values. I used a chi-squared (χ^2) analysis to find the best set of parameters for the kinetic temperature, number density, and ζ parameter to match the theoretical ratios of radiation temperatures to those observed. Specifically, the best fit is to minimize the sum over all measured emission line ratios for a given H II region:

$$\chi^2 = \sum_{\text{observed ratios}} \left(\frac{\text{ratio}_{\text{obs}} - \text{ratio}_{\text{theor}}}{\sigma} \right)^2. \quad (3.35)$$

where σ is the uncertainty in the measurement of the observed ratio. The uncertainty is not in general the same for different ratios (see Table 3.8).

3.4.1 Results from the LVG Method

For the LVG analysis, I used three transitions of ^{12}CO : $^{12}\text{CO } J = 1 \rightarrow 0$, $^{12}\text{CO } J = 2 \rightarrow 1$, and $^{12}\text{CO } J = 3 \rightarrow 2$, and one transition ($J = 2 \rightarrow 1$) of ^{13}CO . These observations were obtained at the JCMT and at the NRAO 12-meter, and they yielded a total of three ratios with respect to $^{12}\text{CO } J = 2 \rightarrow 1$. These observed ratios were compared to the theoretical ratios obtained from an LVG analysis for several values of cloud density, abundance, and kinetic temperature. I investigated values of density that span five orders of magnitude from 10^3 to 10^8 cm^{-3} , and values of ζ that cover six orders of magnitude from 10^{-8} to $10^{-2} \text{ pc s km}^{-1}$. Both of these quantities are incremented by steps of half an order of magnitude. The kinetic temperatures investigated were between 10 K and 290 K with increments of 10 K. For all values of the kinetic temperature, ζ , and density, the LVG program

calculates the radiation temperature for several rotational transitions. Then from this radiation temperature, one can find the theoretical ratio and compare it with the observed ratio. Here, the best values for the kinetic temperature, density, and abundance parameter have been determined by minimizing a χ^2 statistic.

Another parameter that has to be considered in the LVG analysis is the relative abundance of the ^{13}CO isotopomer with respect to ^{12}CO , ψ . I used three values (20, 40, 60) for this parameter to ascertain for which one the lowest minimum would occur. The lowest value, 20, provided the best fit. Such a value of ψ would be expected from studies of the Milky Way: Langer and Penzias (1990) found that the value of ψ varies with galactocentric distance with the smaller values within 4 kpc of the galactic centre. The measurement reported here seems to be in agreement with the conclusion obtained for the Milky Way.

Even more important than the isotopomer ratio is the calculation of the radiation temperature ratios for the observed lines. In order to use these ratios in the LVG analysis, one must be certain that the two spectral lines from which the ratios are measured have similar spatial resolution. Since it is not possible to increase the resolution of the low resolution data, the spectra with higher resolution need to be convolved to spectra of lower resolution. For example, one would convolve the $J = 3 \rightarrow 2$ line to match the $J = 2 \rightarrow 1$ resolution and smooth the $J = 3 \rightarrow 2$ in frequency so that the two spectra have the same velocity resolution. After the convolution is finished, the lines are divided channel-by-channel, and the value of the ratio is averaged over all channels with signal-to-noise higher than 2. Finally, for the ($^{12}\text{CO } J = 3 \rightarrow 2 / ^{12}\text{CO } J = 2 \rightarrow 1$) line ratio, one must change the antenna

Source	$\frac{^{12}\text{CO } J = 3 \rightarrow 2}{^{12}\text{CO } J = 2 \rightarrow 1}$	$\frac{^{12}\text{CO } J = 1 \rightarrow 0}{^{12}\text{CO } J = 2 \rightarrow 1}$	$\frac{^{13}\text{CO } J = 2 \rightarrow 1}{^{12}\text{CO } J = 2 \rightarrow 1}$
NGC 5461	0.80 ± 0.04	0.56 ± 0.11	0.147 ± 0.015
NGC 5462	1.14 ± 0.22	-	0.135 ± 0.030
H660	0.58 ± 0.06	-	0.104 ± 0.010

Table 3.8: The ratios of the radiation temperatures with their uncertainties as they were used in the LVG analysis.

temperatures to the radiation temperature scale by using the equation (A.16) from the Appendix. The values of the available line ratios for the H II regions are in Table 3.8. The uncertainties quoted take into account the observational uncertainty of the CO emission.

Unfortunately it was not possible to calculate the ($^{12}\text{CO } J = 1 \rightarrow 0$)/($^{12}\text{CO } J = 2 \rightarrow 1$) ratio for NGC 5462 and H660, because I did not have all the necessary spectra to convolve the $^{12}\text{CO } J = 2 \rightarrow 1$ line to the $55''$ beam of the NRAO 12-meter telescope. Furthermore, I was unable to observe any transition of CO toward NGC 5471 at the JCMT, so there are no ratios for this giant H II region in Table 3.8 either.

For NGC 5461, there are enough data to use the LVG analysis with confidence. The fits were best for $\psi = 20$, so χ^2 is plotted for the three parameters of interest—

kinetic temperature, density, and abundance—in Figures 3.1, 3.2, and 3.3 with the optimum value of ψ . Because of the design of the program `cobfit`, which computes the χ^2 fits, one has to run it separately for three temperature regions of interest: the low (from 10 K to 100 K), the intermediate (from 100 K to 190 K), and the high temperature region (from 200 K to 290 K). The Figures include only the fits from the three temperature regions that have a χ^2 fit lower than 20. To estimate the uncertainty in the value of the parameter of interest, I found all the fits that result in χ^2 less than nine—an average discrepancy between the observed and the theoretical ratio less than $\sqrt{3}\sigma = 1.73\sigma$. The fits that have $\chi^2 < 9$ are symbolized as full circles in Figures 3.1, 3.2, and 3.3.

The best fit of all ($\chi_{min}^2 = 5.82$) occurs for a temperature of 60 K. From Figure 3.1, one sees that there are two possible regions for the kinetic temperature that have $\chi^2 < 9$. One region is at relatively low temperatures, between 30 and 90 K while the other is at high temperatures: 230 to 250 K. To evaluate these fits, one must also investigate the best values of the other two parameters—density and abundance.

The best fits for the density at low (10 – 100 K), intermediate (100 – 190 K), and high kinetic temperatures (200 – 290 K) are seen in Figure 3.2. The low temperature fits correspond to densities of between $3 \times 10^3 - 10^4 \text{ cm}^{-3}$ with the best fit of $3 \times 10^3 \text{ cm}^{-3}$; for high temperatures, the best fitting density is also $3 \times 10^3 \text{ cm}^{-3}$. The fit for the density, therefore, seems to be fairly stable and independent of temperature. A GMC with a diameter of 80 pc and that density would have a mass of $30 \times 10^5 \mathcal{M}_\odot$, which is in agreement with the masses obtained with the

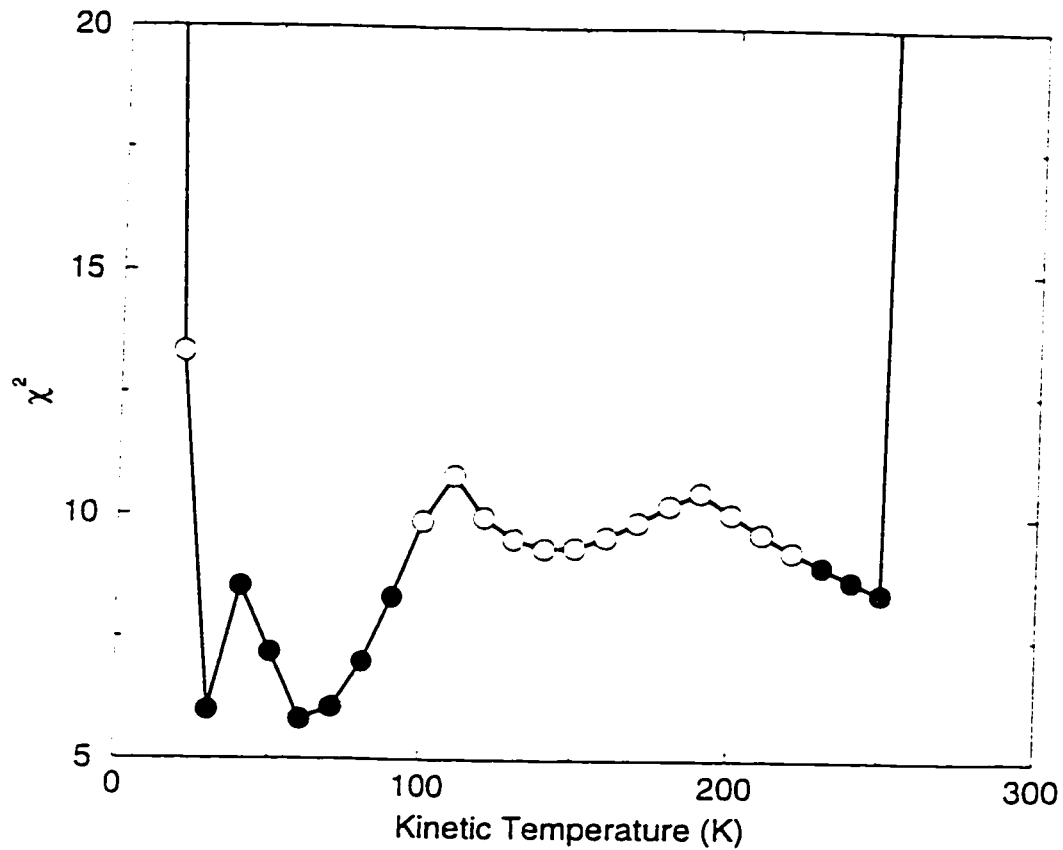


Figure 3.1: The χ^2 is plotted for a large range of kinetic temperatures of the gas in NGC 5461: the χ^2 was minimized over the other parameters for each temperature. Fits that have $\chi^2 < 9$ are denoted by filled circles. The best fit ($\chi^2_{min} = 5.82$) occurs for the kinetic temperatures of 60 K. There are two ranges of temperatures with $\chi^2 < 9$: a cold range of 30 – 90 K and a hot range of (230 – 250 K).

empirical method for individual GMCs (see Table 3.7).

From the discussion of the temperature and the density, one wonders whether the observations come from two separate components of gas: hot dense gas and cold, perhaps less dense, gas. The third parameter, the abundance, adds another dimension to this question. For the first region of temperatures, the abundance is between $1 - 3 \times 10^{-6}$ pc s km⁻¹ while the region of higher temperatures has a value of ζ that is an order of magnitude larger: 3×10^{-5} pc s km⁻¹. The abundance parameter should be examined carefully to decide what are realistic values for it given the available observations for the GMCs of M101.

The abundance parameter, ζ , is defined as the ratio of CO abundance to molecular hydrogen abundance, ϕ , over the ratio of the velocity range of the GMC to its size, $\xi = \text{velocity}/\text{size}$: thus, $\zeta = \phi/\xi = \text{size} \times \phi/\text{velocity}$. The velocities and the sizes of the clouds are given in Table 2.15: from there, it can be deduced that the lowest value for ξ is $5.2/180 = 0.03$ km s⁻¹ pc⁻¹ and the highest value is $10.4/45 = 0.2$ km s⁻¹ pc⁻¹. There are two commonly used values of ϕ : 10^{-4} and 10^{-5} , each of which are examined separately.

If $\phi = 10^{-4}$, then the allowed values of ζ are between 2×10^{-4} and 3×10^{-3} pc s km⁻¹, which are at least an order of magnitude larger than even the largest permitted theoretical values. On the other hand, for $\phi = 10^{-5}$, the abundance can range between 2×10^{-5} and 3×10^{-4} pc s km⁻¹. The lower value of this range is within the possible values of ζ , which means that the model indicates indirectly that the best value for the ratio of the CO abundance over the molecular hydrogen,

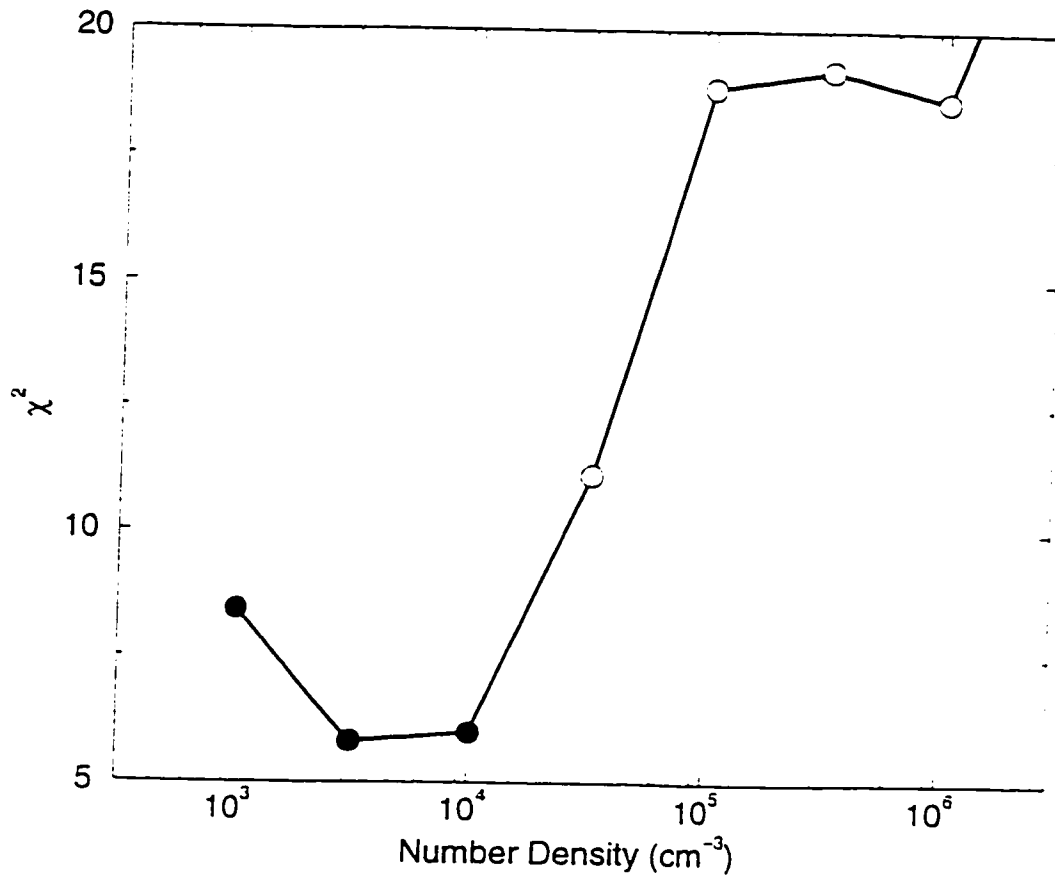


Figure 3.2: The χ^2 is plotted for a large range of number densities of the gas in NGC 5461 for low (10 – 100 K), intermediate (100 – 190 K), and high kinetic temperatures (200 – 290 K). For each temperature range, the χ^2 was minimized for each density. Fits that have $\chi^2 < 9$ are denoted by filled circles. The best fit ($\chi_{min}^2 = 5.82$) occurs for a value of $3 \times 10^3 \text{ cm}^{-3}$ for both the cold and the hot kinetic temperature; the allowed range for the density is $10^3 - 10^4 \text{ cm}^{-3}$.

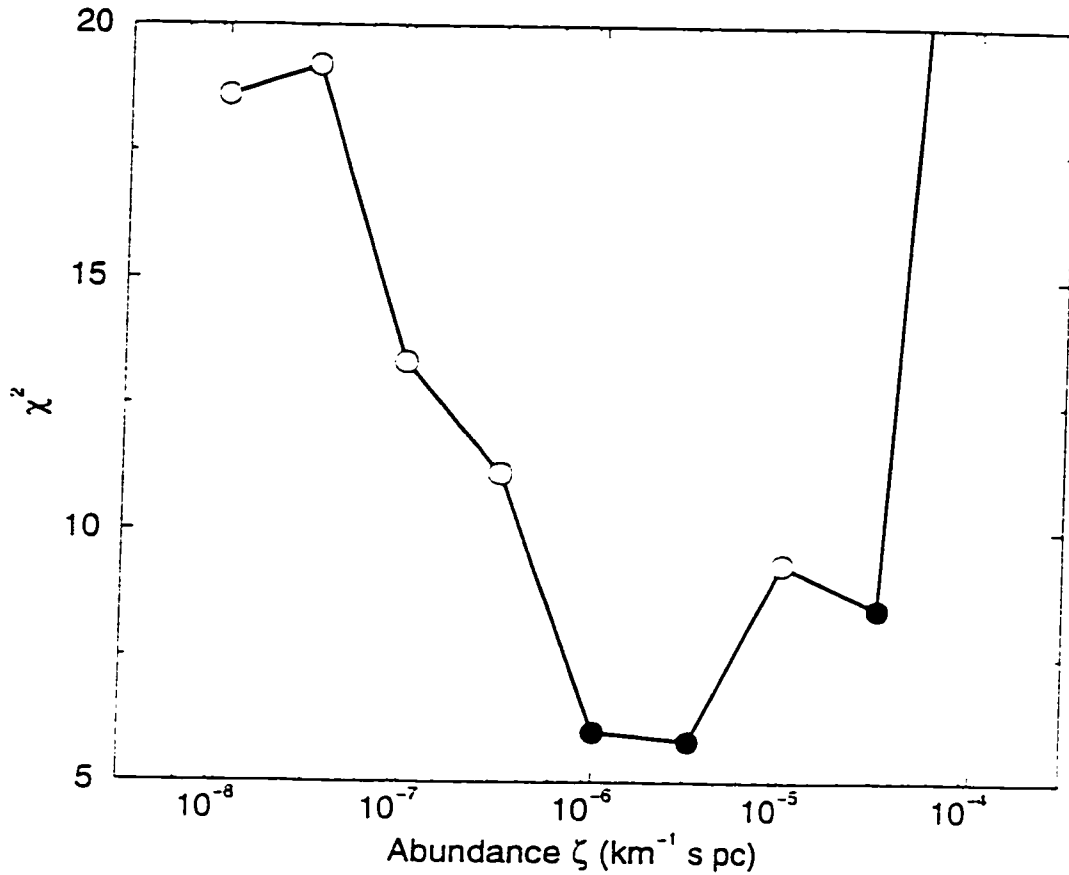


Figure 3.3: The χ^2 is plotted for a large range of abundances of the gas in NGC 5461 for low (10 – 100 K), intermediate (100 – 190 K), and high kinetic temperatures (200 – 290 K). For each temperature range, the χ^2 was minimized for each abundance. Fits that have $\chi^2 < 9$ are denoted by filled circles. The best fit ($\chi^2_{min} = 5.82$) occurs for an abundance of $3 \times 10^{-6} \text{ pc s km}^{-1}$. The values for the abundance that yield a $\chi^2 < 9$ are between $1 - 3 \times 10^{-6} \text{ pc s km}^{-1}$ for the cold gas and $3 \times 10^{-5} \text{ pc s km}^{-1}$ for the hot gas.

ϕ is 10^{-5} . The parameters that provide the two possible fits for NGC 5461 are summarized in Table 3.9.

Before the other H II regions are considered, I plot the best LVG values of the density and abundance with respect to the kinetic temperature in Figure 3.4. It is not surprising that the value of the best fit for the density should increase for lower best fits for the temperature because the product of the density and the temperature is constant if the surface pressure is constant (McLaughlin and Pudritz, 1996). This relation can be understood in a simple way: if the gas is cold, then the molecules are not likely to interact with each other unless the density is significantly high. Furthermore, the smaller scale features (with low ζ) have lower temperatures: this tendency could be due to shielding of the small dense clumps from the stellar UV radiation. The two previous tendencies of the LVG parameters that are seen in Figure 3.4, therefore, are consistent with what one would expect in the environment of the molecular gas in NGC 5461.

The LVG analysis cannot be done for NGC 5462 and H660 because there are only two available ratios (see Table 3.8). The LVG analysis is not conclusive with only two ratios (Thornley and Wilson, 1994), but one can use the available ratios to make some general statements about the physical properties of NGC 5462 and H660. Because the ($^{12}\text{CO } J = 3 \rightarrow 2 / ^{12}\text{CO } J = 2 \rightarrow 1$) ratio for NGC 5462 is larger than that of NGC 5461, the molecular gas in NGC 5462 may be warmer than the molecular gas around NGC 5461. One expects from the Boltzmann equation (3.8) that, for usual temperatures of quiescent molecular gas (10 K), the second level is more populated than the third level, which means that for cold gas the ratio (^{12}CO

$J = 3 \rightarrow 2 / ^{12}\text{CO } J = 2 \rightarrow 1$) is less than unity; however, in the case of NGC 5462, the ratio is larger than unity, which implies that the gas is probably considerably hotter than the quiescent gas.

Unlike the ($^{12}\text{CO } J = 3 \rightarrow 2 / ^{12}\text{CO } J = 2 \rightarrow 1$) ratio, which is an indicator of temperature (Wilson et al., 1997), the ($^{12}\text{CO } J = 2 \rightarrow 1 / ^{13}\text{CO } J = 2 \rightarrow 1$) ratio is mostly a tracer of molecular gas according to the LVG model. One can conclude that the normal H II region, H660, has less gas than the giant H II regions because it has a small value of ($^{13}\text{CO } J = 2 \rightarrow 1 / ^{12}\text{CO } J = 2 \rightarrow 1$). The giant H II regions for which the ratio has been measured, NGC 5461 and NGC 5462, have the same ratios within their uncertainties, which may suggest that the two regions have similar masses in accordance with the LTE method.

Parameter	Cold solution [Range of values]	Hot solution [Range of values]
Density (cm^{-3})	3×10^3 [$3 \times 10^3 - 10^4$]	3×10^3 [($1 - 3$) $\times 10^3$]
Kinetic Temperature (K)	60 [30 - 90]	250 [230 - 250]
Abundance ζ (pc s km^{-1})	3×10^{-6} [($1 - 3$) $\times 10^{-6}$]	3×10^{-5}

Table 3.9: The allowed physical parameters for NGC 5461 from the LVG analysis and their best values for the low temperature solution (in second column) and for the high temperature solution (in column three).

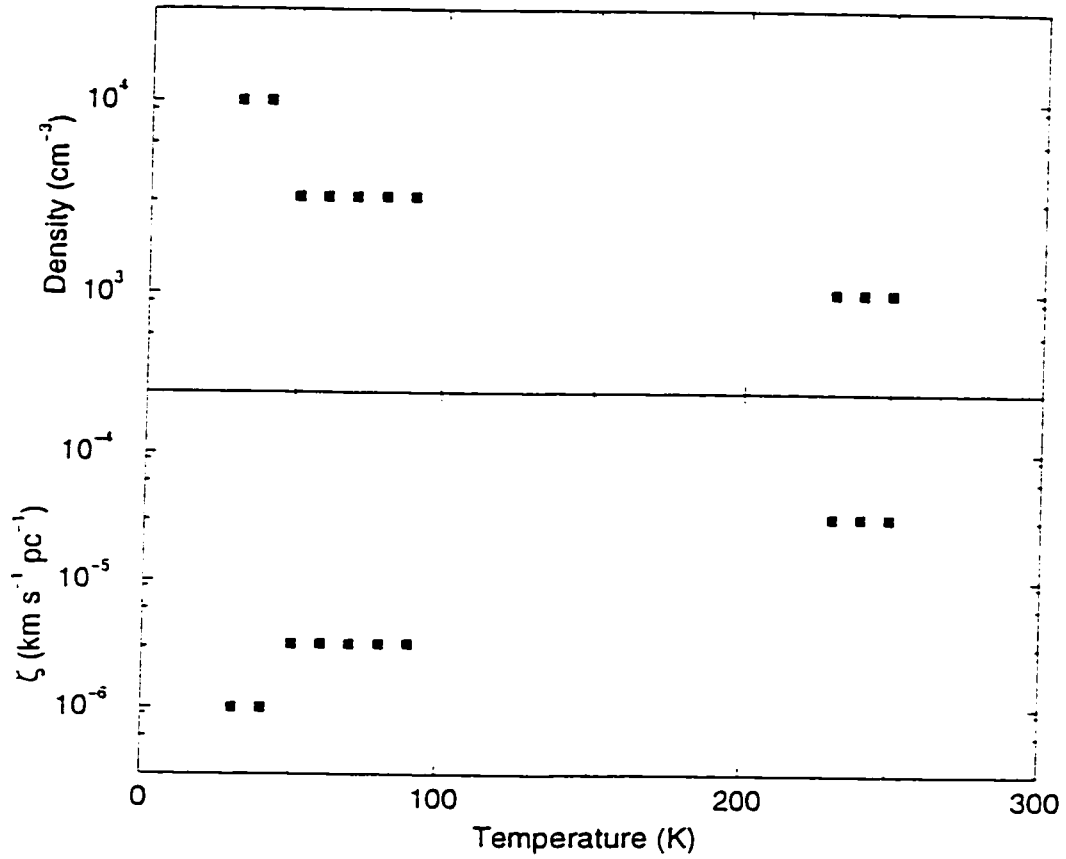


Figure 3.4: The density and the abundance of the molecular gas are plotted against the kinetic temperature. The warm, slightly denser gas is probably organized in small clumps of 1 pc while the hotter clouds are comparable with the diameters (approximately 80 pc) of the features in the Owens Valley map.

3.5 Summary of the Properties of the Molecular Gas in the H II Regions of M101

Three methods have been used to calculate the masses of the H II regions in M101. The results are summarized in Table 3.10, which also includes an upper limit from the Owens Valley observation of NGC 5462. The LTE method yields the highest values for the molecular mass: on the order of $10^8 \mathcal{M}_{\odot}$ associated with each of the H II regions. Because the masses are so large, it is certain that with the single dish instruments one observes associations of molecular clouds (typical values of individual GMCs are around $10^5 \mathcal{M}_{\odot}$).

The empirical method yields masses that are two to three times smaller than the mass obtained from the LTE analysis. The most important uncertainty here is the value of X . If the value of X were just a few times larger, then the two results would be comparable. Since the value of X has a large intrinsic uncertainty, the discrepancy between the LTE results and the empirical methods can be easily solved if the X value is larger. A factor of two or three is still well within the allowed values of X from equation (3.30).

Another encouraging result is that two empirical molecular masses (one from the 12-meter and the other from the Owens Valley array) agree within their uncertainties. This is particularly interesting when one considers that the elusive η_c parameter is not necessary to calculate the empirical mass from the 12-meter NRAO telescope. The fact that the two results agree fairly well indicates that the

value of η_c is probably reasonably determined or, in other words, the GMCs are nearly (maybe even completely) resolved in the Owens Valley observations.

Finally, the last method involves an LVG calculation. For the best value of the density and an assumed cloud diameter of 80 pc, the mass of an average GMC in NGC 5461 is $3.0 \times 10^6 \mathcal{M}_\odot$, which is similar to what is calculated for the individual GMCs from the empirical method.

The LVG analysis indicates that there are two possible regimes of kinetic temperature: a cold regime of 30 to 90 K, and a hot regime of 230 to 250 K. The colder gas has the slightly higher density of $3 \times 10^3 - 10^4 \text{ cm}^{-3}$ and the very small values of the zeta abundance. These values of ζ suggest that the cold gas is organized in clumps with diameters of a few pc, which could not possibly be resolved with the current technology. The hotter gas has values of ζ that are consistent with the sizes of the GMC in NGC 5461 of approximately 80 pc—the features that are observed with the Owens Valley array. The properties of the molecular gas and the comparison of the three methods are discussed in more detail in Section 4.1.1.

Source	Method	Mass ($\times 10^6 \mathcal{M}_{\odot}$)
NGC 5461	LTE [†]	120 [70 - 180]
NGC 5461	Empirical 12-meter telescope	50 ± 10
NGC 5461	Empirical [†] Owens Valley	34 ± 14
Average mass of GMC in NGC 5461	Empirical [†] Owens Valley	2.2
Mass of typical GMC in NGC 5461	LVG	3
NGC 5462	LTE [†]	> 50 [25 - 90]
NGC 5462	Empirical 12-meter telescope	17 ± 6
NGC 5462	Empirical [†] Owens Valley	< 50
H660	LTE [†]	160 [120 - 200]
NGC 5471	Empirical 12-meter telescope	11 ± 4

Table 3.10: Summary of masses obtained from the three methods in the analysis. The methods that are accompanied by a dagger ([†]) are dependent on the value of the coupling efficiency, η_c .

Chapter 4

Discussion

The goal of this chapter is to explain some of the properties of the molecular gas in the H II regions and discuss the consequences of the star-forming process. The chapter is divided into two parts. In Section 4.1, the properties of the molecular gas in the H II regions are presented and compared with those of H II regions in other galaxies. Section 4.2 contains estimates of the star-formation efficiencies of NGC 5461 and NGC 5471 and a discussion of how the star-forming process influences the properties of the interstellar medium (molecular, atomic, and ionized gas) in these H II regions in M101.

4.1 Properties of the Molecular Gas

The physical characteristics of the molecular gas, such as temperature and mass, are discussed in Section 4.1.1. Section 4.1.2 presents the relationship between the size of the gas cloud and its velocity dispersion. Finally, the stability of the GMCs is discussed in Section 4.1.3.

4.1.1 Masses and Temperatures

The physical characteristics of the molecular gas as observed for the four H II regions in M101 are presented in turn.

NGC 5461

NGC 5461 is the brightest H II region in CO emission; therefore, the data set for NGC 5461 is the most complete of all the giant H II regions in M101. There are three estimates for the mass of the association of molecular clouds in NGC 5461, which range in value from $(3 - 12) \times 10^7 \mathcal{M}_\odot$ (see page 144). The discrepancy of a factor of four in the range of possible values is not disconcerting, because there are large uncertainties. The easiest, most likely explanation is that the real X factor for M101 is higher than what was used in the analysis.

It is a useful check to compare the range of masses for NGC 5461 with the total molecular mass calculated for the inner area of M101 (within a 5' radius), which is

$380 \times 10^7 \mathcal{M}_\odot$ (Kenney et al., 1991) when one adjusts for the adopted distance of 7.4 Mpc: the measurements by Kenney et al. (1991) agree well with my measurements at the 12-meter telescope as seen in Table 4.1.

The value of the mass of the inner area of M101 was calculated by Kenney et al. using the empirical method with the same type of data I obtained (NRAO 12-meter): therefore, the total molecular gas for the inner part of M101 should be compared with the equivalent measurement of the gas in NGC 5461, $5 \times 10^7 \mathcal{M}_\odot$, which represents a little over 1% of the total mass of the inner area of its host galaxy. NGC 5461 has a surface area of slightly less than 1% of the inner galaxy: so the association of clouds in NGC 5461 has a surface density that is comparable to the average surface density of the inner core of M101. This conclusion is not true for individual giant GMCs in NGC 5461. The surface density of the average cloud is at least an order of magnitude higher than the average surface density of the inner galaxy, which is consistent with the presence of star-formation in the giant H II regions.

Another result of star-formation is that the molecular gas becomes hotter. One of the diagnostics of high temperatures is the ($^{12}\text{CO } J = 3 \rightarrow 2 / ^{12}\text{CO } J = 2 \rightarrow 1$) ratio (page 138). NGC 5461 has a similar ($^{12}\text{CO } J = 3 \rightarrow 2 / ^{12}\text{CO } J = 2 \rightarrow 1$) ratio with the clouds in M33 that are associated with H II regions (Wilson et al., 1997). However, the ratio for NGC 5461 does not approach the value for the GMC NGC 604-2 which is, indeed, very high compared to other ratios seen in M33 and other galaxies (see page 18).

Measured Quantity	Kenney et al. (1991)	Measurements reported here
$\int T_R^* dv$ (K km s ⁻¹)	2.59 ± 0.32	2.50 ± 0.48
V_{centre} (km s ⁻¹)	275	273.8
ΔV (km s ⁻¹)	28	29.2
obs peak T_R^* (mK)	91 ± 17	78 ± 8

Table 4.1: Comparison of $^{12}\text{CO } J = 1 \rightarrow 0$ emission measurements with the 12-meter for NGC 5461 made by Kenney et al. (1991) with the measurements for this thesis.

An explanation for the lower value of the ($^{12}\text{CO } J = 3 \rightarrow 2 / ^{12}\text{CO } J = 2 \rightarrow 1$) ratio in NGC 5461 than that found in other giant H II regions is that the clouds in NGC 5461 have cold gas mixed in with the hot gas. According to the LVG analysis, the GMCs in NGC 5461 consist of large (80 pc), hot (250 K) balls of gas that have embedded in them small clumps (5 pc) of warm (60 K), denser gas. The hot component is similar in temperature and density to the GMCs in M33 associated with H II regions (Wilson et al., 1997).

NGC 5462

Both the LTE method and the empirical method suggest that NGC 5462 has two or three times less molecular mass than NGC 5461. One could argue that the LTE estimate of the molecular mass for NGC 5462 is based only on the column density from one channel, so the LTE mass value is uncertain. The masses from the empirical analysis, however, are based on data obtained during the same few hours and under similar weather conditions—there probably *is* more molecular material in NGC 5461 than NGC 5462. This conclusion is consistent with the fact that the molecular gas in NGC 5462 was not detected with the Owens Valley array.¹

NGC 5462 might not be as massive as NGC 5461, but it might be hotter than NGC 5461. The ($^{12}\text{CO } J = 3 \rightarrow 2 / ^{12}\text{CO } J = 2 \rightarrow 1$) ratio of NGC 5462 is even higher than the extraordinary cloud NGC 604-2 in M33. The uncertainty of this ratio for NGC 5462 is unfortunately fairly high—it agrees within its uncertainty with normal clouds in M33 and IC10 (Petitpas and Wilson, 1998).

NGC 5471

NGC 5471 is significantly weaker than NGC 5462 and NGC 5461: the only observation that was made of NGC 5471 was in $^{12}\text{CO } J = 1 \rightarrow 0$ emission. One explanation is that the molecular mass has been underestimated because the X

¹Even the strongest peak of NGC 5461 was only 4.5σ above the noise level in the interferometer map, so it is not surprising that CO was not detected in NGC 5462 with the Owens Valley millimeter array.

factor for this region is higher than what was used. Unlike NGC 5462, NGC 5471 is several kpc away from NGC 5461 and from the galaxy's centre: therefore, NGC 5471 has considerably lower metallicity than regions closer to the centre of M101. An effort was made to compensate for the metallicity effect and increase the value of X for NGC 5471, but one cannot exclude the possibility that the value of X might be three or four times larger than the one used. If the X factor is larger, then the mass of the molecular gas of in NGC 5471 could be comparable to that of NGC 5461.

A more probable explanation of the deficiency of CO emission in NGC 5471 is that there is genuinely less molecular gas present. A clue to this problem is the presence of large amounts of atomic gas near the giant H II region (Kamphuis, 1993). Perhaps the atomic gas was converted to molecular gas in NGC 5471 slower than in the other two giant H II regions, or more of the molecular gas was dissociated to atomic gas. There is more on this topic in Section 4.2.3.

H660

The LTE mass of the normal H II region is comparable with the mass of NGC 5461. This result is somewhat unexpected, but it is likely that the 20'' beam of the JCMT might have measured ambient gas that is not associated with the H II region. Furthermore, the ratio ($^{13}\text{CO } J = 2 \rightarrow 1 / ^{12}\text{CO } J = 2 \rightarrow 1$) is low, which implies that the density toward H660 is lower than that of the giant H II regions.

It is particularly interesting that H660 has a ($^{12}\text{CO } J = 3 \rightarrow 2 / ^{12}\text{CO } J = 2 \rightarrow 1$) ratio that resembles the ratio of the clouds in M33 that are not associated with any

H II regions. Therefore, it seems that the molecular gas in the normal H II region might be cooler and less massive than the gas associated with the giant H II regions.

4.1.2 Size:line-width Relationship

Another interesting property of GMCs is the size:line-width relationship they exhibit. In several cases, it has been found that the diameter of a cloud, D , is related to its line-width or velocity dispersion, ΔV , and indeed that the relationship holds on a variety of scales (McLaughlin and Pudritz, 1996). In M31 and M33 (Wilson and Scoville, 1990; Wilson and Rudolph, 1993), the relationship is

$$\frac{\Delta V}{\text{km s}^{-1}} = 1.2 \left(\frac{D}{\text{pc}} \right)^{0.5}, \quad (4.1)$$

which agrees (within large error bars) with the relationship observed for GMCs in the Milky Way (Sanders et al., 1985).

In equation (4.1), the diameter D is assumed to be the true size of the resolved GMC. The true size of the cloud is obtained by deconvolution of the observed size, D_{obs} from the size of the beam, D_{beam} . A simple approach is to assume that the beam and source are Gaussians, so that the deconvolved diameter will be

$$D = \left(D_{obs}^2 - D_{beam}^2 \right)^{1/2}, \quad (4.2)$$

where D_{beam} is in this case 80 pc (2.3"). The deconvolved diameter and velocity dispersion of the GMCs in NGC 5461 are presented in Table 4.2. For the GMCs

that are clearly not resolved with the interferometric data, an upper limit of their true diameter is presented.

From the size:line-width relationship, the expected diameter D_{exp} is calculated given the observed velocity ΔV_{obs} . Table 4.2 indicates that several GMCs in NGC 5461 (3, 6, 9, and 10) are considerably larger than expected from equation (4.1). Some of the larger GMCs do not seem to follow the well established principle in our Galaxy that the larger GMCs have higher velocity dispersion (Maloney and Black, 1988). For the clouds in NGC 5461, the larger clouds tend to have the smallest velocities.

To explain these differences from the standard size:line-width relation in a simple way, one might consider that GMC sizes can vary by two orders of magnitude in the same galaxy (Maloney and Black, 1988): therefore, one could expect a large spread of velocity dispersions and sizes of GMCs. The smaller GMCs of the range have probably not been resolved even with the high resolution interferometric data. However, the large GMCs are probably resolved, and they have the smallest velocity dispersions. This tendency of the NGC 5461 GMCs can be explained if the clouds resulted from the collision of small clouds: the velocity dispersion of the large GMC would be smaller as the number of clouds, and consequently the mass of the final cloud increases (Blitz, 1993).

The GMCs in the Milky Way and M33 have higher velocity dispersions for a given size of GMC than those in NGC 5461. Another grand-design spiral, M51, has associations of GMCs that are considerably larger (250 – 370 pc with a linear

Molecular Cloud	ΔV_{obs} (km s ⁻¹)	D (pc)	D_{exp} (pc)
1	7.8	49	42
2	10.4	58	75
3	5.2	91	19
4	7.8	< 80	42
5	7.8	< 80	42
6	7.8	78	42
7	7.8	62	42
8	5.2	< 80	19
9	5.2	58	19
10	5.2	99	19

Table 4.2: The velocity dispersion, ΔV_{obs} , and the size, D , of the ten GMCs in NGC 5461 are presented along with the expected sizes, D_{exp} , given the M33 size:line-width relationship. The diameter, D , is the deconvolved size of each GMC; the entries that are upper limits indicate that the clouds are unresolved.

resolution of 160 pc), and their velocity dispersion is smaller than that observed in NGC 5461 (Rand, 1993). So the GMCs in M101 seem to be the intermediate step between those seen in M51 and the Milky Way: M51 has even smaller velocity dispersions than M101 while the Galaxy and M33 have larger dispersions for the same size of cloud. This difference in kinematic properties of the clouds in these galaxies might suggest that the GMCs formed differently. In M101 and M51, perhaps collisions of smaller clouds were a more important mechanism of cloud formation than in the Milky Way and M33.

4.1.3 Stability of the GMCs in NGC 5461

Some kinematic information of the GMCs in NGC 5461 has been presented. To find out if these structures are, in fact, gravitationally bound, I compare their molecular masses to their virial masses. If the virial mass is less than the molecular mass, then the GMCs are considered gravitationally bound.

The virial mass is (Rand, 1993)

$$M_{vir} = 525 \mathcal{M}_{\odot} \left(\frac{\Delta V_{FWHM}}{\text{km s}^{-1}} \right)^2 \frac{D}{\text{pc}}, \quad (4.3)$$

where the diameter is the deconvolved diameter of Table 4.2. These results have been tabulated in Table 4.3 along with the masses found by the empirical method. In the calculation of the virial mass, the contribution of streaming motions has not been included because the streaming motions in GMCs of M101 are small.

The virial and the molecular masses have been plotted with their uncertainties in Figure 4.1: the uncertainty in the virial masses is estimated to be 30%. The virial mass of each GMC is equal to its molecular mass within the uncertainties. There are two cases (GMCs 4 and 5) where the virial masses appear to be larger than the molecular masses, but the virial masses are just upper limits.

Because the virial masses are smaller than the molecular masses, the GMCs in NGC 5461 are in gravitational equilibrium. This conclusion is even stronger if the real value of the X factor is greater than what was used for the calculation of the molecular masses. Therefore, the GMCs in NGC 5461 are bound, in the same manner as the GMCs in the irregular galaxy IC 10 (Petitpas and Wilson, 1998) and the GMCs in M33 that were associated with H II regions (Wilson and Scoville, 1990).

Molecular Cloud	M_{vir} ($10^5 \mathcal{M}_\odot$)	M_{mot} ($10^5 \mathcal{M}_\odot$)
1	16 ± 5	15 ± 5
2	33 ± 10	44 ± 10
3	13 ± 4	20 ± 5
4	$< 26 \pm 8$	18 ± 5
5	$< 26 \pm 8$	12 ± 3
6	25 ± 8	37 ± 9
7	20 ± 6	27 ± 6
8	$< 11 \pm 3$	10 ± 3
9	8 ± 2	14 ± 4
10	14 ± 4	23 ± 7

Table 4.3: A comparison of the virial masses of the GMCs in NGC 5461 with the masses calculated empirically.

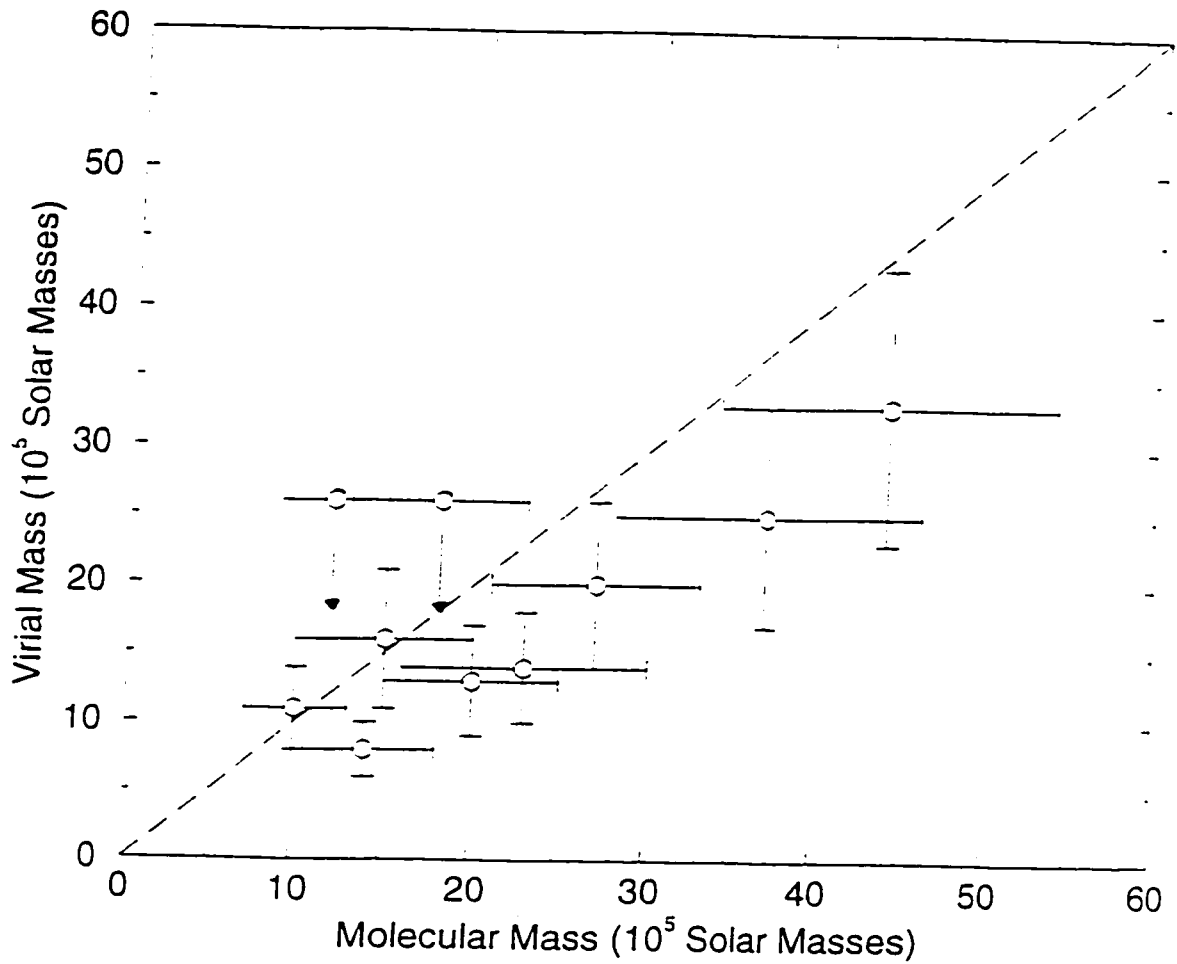


Figure 4.1: Comparison of the molecular mass of each GMC in NGC 5461 (obtained with the empirical method) with the virial mass. The dotted line indicates where the virial and the molecular masses are equal. The virial masses of the two points that lie above the line of equal masses are, in fact, upper limits.

4.2 Star Formation

In this section, I examine how the star-forming process influences the properties of the interstellar medium in its vicinity. There is some theoretical work that suggests that the mass of the GMC can be used to predict how many bright stars the GMC will produce: this discussion follows in Section 4.2.1. The radiation from the star ionizes its surrounding gas and probably changes its morphology: see Section 4.2.2. In Section 4.2.3, a comparison of the CO map and the H I map indicates that the atomic gas is offset from the molecular gas. The mass of the interstellar dust in the GMC is calculated, and some conclusions are drawn about the inferred total mass of the gas in Section 4.2.4. Finally, the star-forming efficiency is discussed in Section 4.2.5.

4.2.1 Role of the Cloud's Mass in Star-formation

One of the main motivations of this thesis is to understand the connection (if any) between the molecular gas of M101 and the existence of bright stars that produce giant H II regions. In the Milky Way, the masses of GMCs that are affiliated with OB associations² are between $(1 - 7) \times 10^5 \mathcal{M}_{\odot}$ (Williams and McKee, 1997). From this observational result, Williams and McKee (1997) suggest that the mass of a GMC might be a prognostic of the probability of the GMC to have a massive star embedded in it: the probability that a GMC will contain a very bright massive

²OB associations are loose affiliations of very young bright stars.

star (O9.5) increases as the mass of the cloud increases. All the GMCs in NGC 5461 have masses of at least $1 \times 10^6 \mathcal{M}_{\odot}$, which would indicate with certainty, according to Fig. 7 of Williams and McKee (1997), that some bright O stars have formed. Of course, these stars would not be visible in optical wavelengths because the light from the stars would be obstructed by the gas and interstellar dust in the clouds.

4.2.2 CO Map Compared with the High-resolution $H\alpha$ Image

One might expect that molecular and ionized hydrogen, which is observed via the $H\alpha$ transition, should be associated with each other. In Figure 4.2, the CO map is compared with a recent $H\alpha$ map that was kindly provided by Robert C. Kennicutt: special care was taken to match the co-ordinates to those of the CO map from the Owens Valley millimeter array. The enumerated GMCs are denoted by crosses or dots to distinguish them from the contours of the $H\alpha$ map.

The CO peaks surround the $H\alpha$ emission peaks: in particular, the GMCs are displaced from the peak of the $H\alpha$ image by 2 - 5" or, at the distance of M101, 70 - 130 pc. A possible reason, which was used to explain the same type of anticorrelation in M51 (Rand, 1993), is that the presence of gas with high surface density increases the extinction from the associated dust. The radiation from the ionized gas is obstructed, and therefore the $H\alpha$ emission is anticorrelated with the molecular gas.

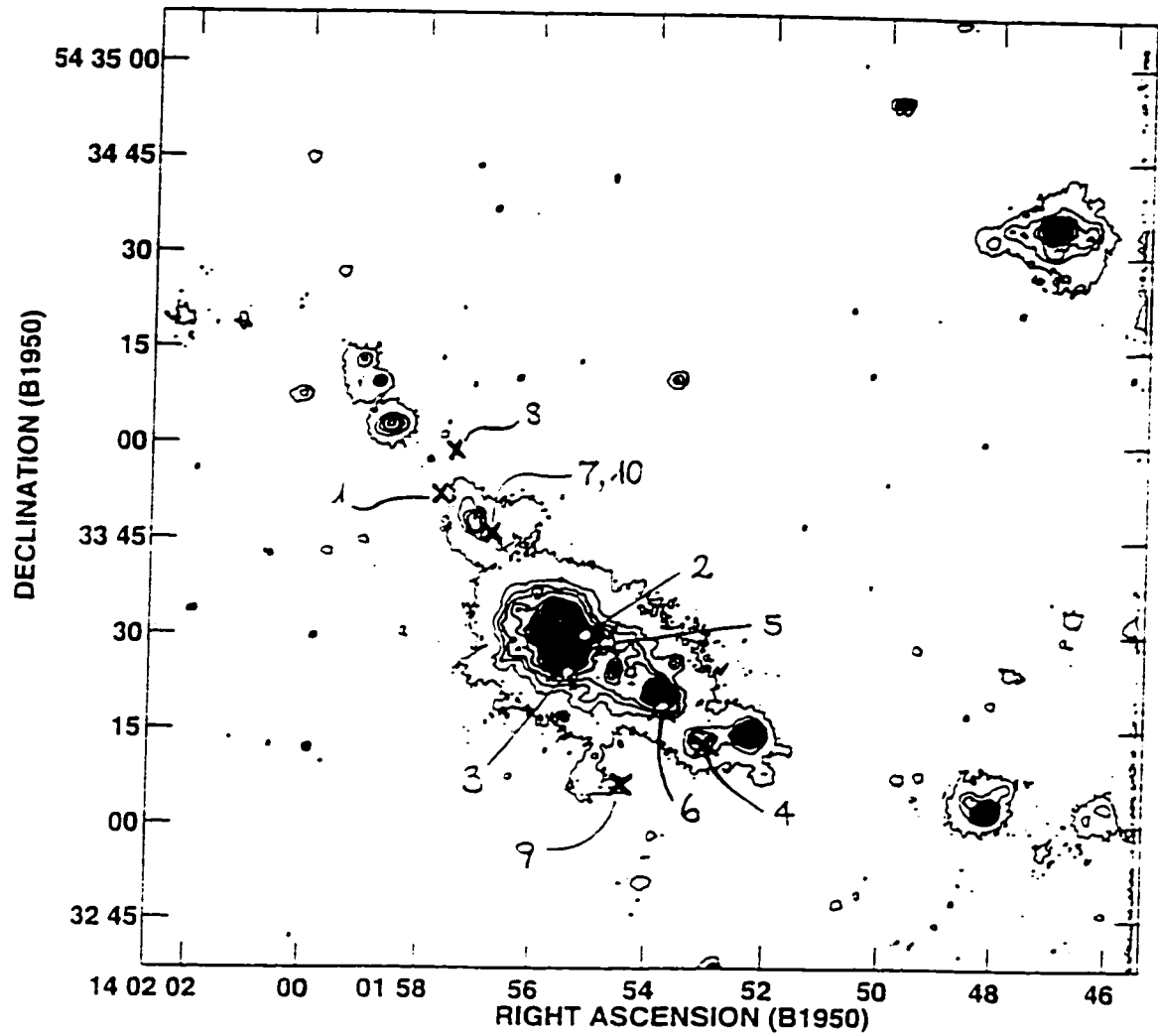


Figure 4.2: Comparison of the CO with the contour H α map of NGC 5461. The GMCs, which are denoted by crosses or dots, surround the H α emission peaks.

4.2.3 Molecular Gas Compared with Atomic Gas

The anticorrelation between $H\alpha$ and molecular hydrogen is noted in the previous section. In this section, the relationship between the molecular and *atomic* gas H I is discussed.

Figure 4.3 presents the GMCs in NGC 5461 superimposed on the high resolution (9") H I contour map that was kindly provided by Robert Braun. The GMCs are denoted with crosses. The CO peaks are displaced compared to the peak of the H I image by 15" - 20" or, at the distance of M101, 540 - 720 pc. A possible explanation for this displacement is that the radiation from the young massive stars in the H II regions may have dissociated the molecular gas to atomic gas: this explanation was used for M51 where a similar displacement was observed. (Vogel et al., 1988)

A large scale study of the atomic gas in M101 was conducted with a 6" resolution (Braun, 1995). Two of the several positions observed coincide with the giant H II regions NGC 5461 and NGC 5471. The atomic masses for the two regions are $5 \times 10^7 M_{\odot}$ and $4 \times 10^7 M_{\odot}$ respectively, which are a few times higher than the corresponding molecular mass observed in similar beams. This result is consistent with the observed ratios of atomic over molecular gas in a sample of 27 Sc galaxies (Young and Scoville, 1991).

Despite the fact that the masses of the atomic gas for NGC 5461 and NGC 5471 are similar, their *molecular* masses are different by probably an order of magnitude. Why does NGC 5461 have so much more molecular gas than NGC 5471? Either

NGC 5461 has an abundance of molecular material, or NGC 5471 has an abundance of atomic gas. For the first scenario, NGC 5461 has a more efficient mechanism to convert atomic to molecular gas than NGC 5471 does. The efficiency of the conversion might be enhanced by large-scale gravitational effects that increase gas interactions and remove loosely bound atomic gas (Young and Scoville, 1991). The slightly higher star-forming efficiencies in NGC 5461 compared to those in NGC 5471 (see Section 4.2.5) might suggest that the GMCs have formed in NGC 5461 faster than in NGC 5471.

Of course, star-formation creates powerful young stars that dissociate the GMCs eventually: this mechanism might have caused the displacement of the H I from the CO clouds in NGC 5461 (Vogel et al., 1988). For the second scenario, the star-formation mechanism in NGC 5471 has had more time to dissociate the molecular gas to atomic gas by the intense radiation from the young stars (Vogel et al., 1988; Wilson and Matthews, 1996).

Either of these theories could be true. Unfortunately, the available data do not suffice to find the ages of the giant H II regions in order to distinguish among the two possibilities. If NGC 5471 were older than NGC 5461, then probably the second scenario would be true. Because there are no relative age data, one might hypothesize that the first scenario is closer to the truth: i.e., the atomic gas in NGC 5461 formed more molecular gas than the atomic gas in NGC 5471 did. The reason for this choice is that NGC 5461 is nearer the centre of the galaxy; the atomic clouds in it might experience more collisions and hasten the conversion to molecular gas.

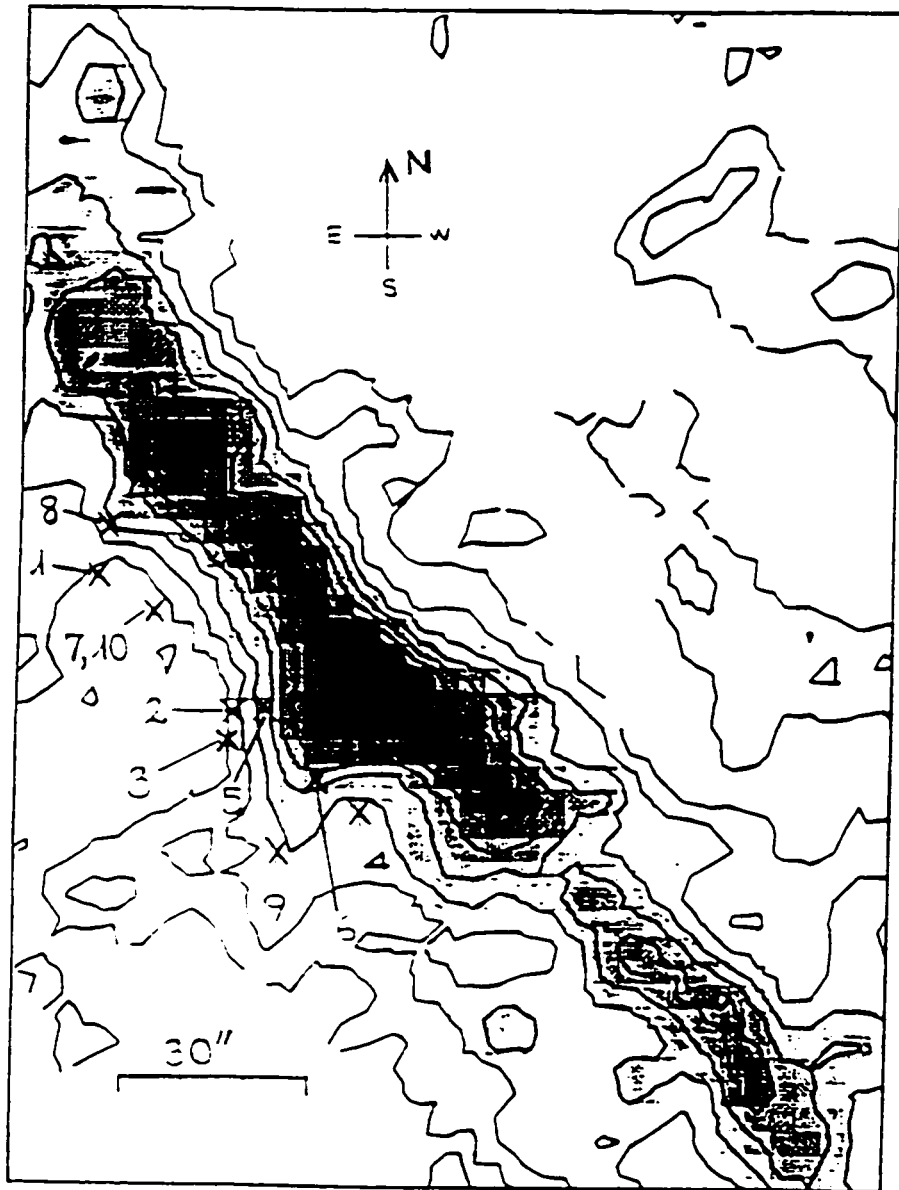


Figure 4.3: Comparison of the GMCs, which are denoted with crosses, with the atomic hydrogen contour map of NGC 5461. The GMCs in the CO map are offset by approximately 600 pc on average from where the H I emission peaks.

4.2.4 Masses Derived from the IRAS Catalog

Another way of estimating the total mass of the gas is to calculate the mass of the dust and then assume some gas-to-dust ratio. One can calculate the dust mass from the 60 μm -wavelength fluxes obtained from the Infrared Astronomical Satellite (IRAS) point source catalog with the equation (Fich and Hodge, 1991):

$$M_{dust} = \frac{4 a \rho}{3 Q_{em}} \frac{S_\nu d^2}{B_\nu(T)}. \quad (4.4)$$

where a is the radius of the dust grain, ρ is the density of the dust grain, Q_{em} is the dust grain emission efficiency, S_ν is the measured flux density, d is the distance to the dust (7.4 Mpc for the giant H II regions in M101), and $B_\nu(T)$ is the Planck function. The infrared fluxes for two giant H II regions of M101 are given in Table 4.4: NGC 5462 is not detected as a point source.

The data in Table 4.4 can be used in equation (4.4) to find the mass of the dust. For the calculation, it has been assumed that $\rho = 3 \text{ g cm}^{-3}$, $Q_{em}/a = 340 \text{ cm}^{-1}$, and $T=30 \text{ K}$ (Fich and Hodge, 1991). With these assumptions, the dust mass for NGC 5461 is $5 \times 10^5 \mathcal{M}_\odot$ while, for NGC 5471, the dust mass is $9 \times 10^4 \mathcal{M}_\odot$. If the gas-to-dust ratio is assumed to be a typical value of 600 for Sc galaxies [Young and Scoville (1991) and references therein], then the total gas mass in NGC 5461 is $3 \times 10^8 \mathcal{M}_\odot$, and the total gas mass in NGC 5471 is $5 \times 10^7 \mathcal{M}_\odot$. This result is in agreement with the total gas mass one would expect from the sum of the molecular gas (see Table 3.10), the ionized gas (in Table 1.5), and the atomic gas for the two regions.

Wavelength (μm)	Flux for NGC 5461 (Jy)	Flux for NGC 5471 (Jy)
12	0.40	0.25
25	1.93	(0.25)
60	9.65	1.81
100	(18.25)	(2.54)

Table 4.4: The infrared fluxes of the giant H II regions of M101 (NGC 5461 and NGC 5471) from the IRAS Point Source Catalog. NGC 5462 was not detected as a point source. The values in parentheses are uncertain.

The uncertainties in the estimates of the dust mass, and therefore of the total gas mass, are large. Typical uncertainty in the dust mass is a factor on the order of unity. It will be interesting to compare the crude mass from IRAS with the mass obtained from SCUBA, the Submillimeter Common User Bolometer Array recently installed on the JCMT.

4.2.5 Star-formation Efficiency

The star-formation efficiency is the ratio of the mass of stars formed in the region to the molecular mass of the region [see, for example, the references in Wilson and Matthews (1996)]. To calculate the mass of stars, one has to make a series of assumptions because it is not possible to observe individual normal stars at the distance of M101. The assumption used is that one can estimate the mass of the OB stars from the measured UV flux of which 40% results from the OB stars (Rosa and Benvenuti, 1994): the masses of the stars in NGC 5461 and NGC 5471 appear in Table 1.5 on page 23. The masses of the molecular associations appear in Table 3.10 on page 144.

Now one can divide the stellar masses with the masses of the molecular gas in the two giant H II regions. The star-forming efficiencies are tabulated in Table 4.5. These values are *smaller* than the efficiencies of a few percent (1% – 4%) observed in several GMCs in the Milky Way such as the Taurus-Auriga, Orion A, and Orion B clouds [see, for example, the references in Blitz et al. (1981) and Wilson and Matthews (1996)]. The conclusion is that the *GMCs in these giant H II regions*

Property	NGC 5461	NGC 5471
Total molecular mass	$10^8 \mathcal{M}_\odot$	$1 \times 10^7 \mathcal{M}_\odot$
Total efficiency	0.1%	0.08%

Table 4.5: Star-formation efficiencies for NGC 5461 and NGC 5471.

are not particularly efficient in creating stars: however, they still produce many massive stars because the GMCs have such large reservoirs of molecular material (as discussed in Section 4.2.1).

Chapter 5

Conclusions

In this thesis, the molecular component of three giant H II regions and one normal H II region in the spiral galaxy M101 were investigated with new observations from two single dish telescopes (JCMT and NRAO 12-meter) and from the Owens Valley millimeter array. NGC 5461 and NGC 5462 were observed in the following transitions: $^{12}\text{CO } J = 1 \rightarrow 0$, $^{12}\text{CO } J = 2 \rightarrow 1$, $^{12}\text{CO } J = 3 \rightarrow 2$, and $^{13}\text{CO } J = 2 \rightarrow 1$: NGC 5461 was the only region that had strong enough emission that its molecular gas could be observed with the Owens Valley millimeter array (resolution of approximately 80 pc). The third giant H II region, NGC 5471, was detected only in the single-dish observation of $^{12}\text{CO } J = 1 \rightarrow 0$ at the NRAO 12-meter telescope. Finally, the normal H II region H660 was observed with the JCMT in three CO transitions: $^{12}\text{CO } J = 2 \rightarrow 1$, $^{13}\text{CO } J = 2 \rightarrow 1$, and $^{12}\text{CO } J = 3 \rightarrow 2$.

The data were analyzed using three independent methods to calculate the mass

of the molecular gas in the H II regions. The first method (LTE) assumes that the gas is in LTE (local thermodynamical equilibrium); a detailed description of the definition of LTE can be found on page 97. The second method ('empirical') is an empirical approach based on the observation that the column density of molecular hydrogen is proportional to the observed integrated intensity—the constant of proportionality, X , can be estimated based on the metallicity of the galaxy and the value of X_{Gal} (page 119). More rigorous is the third method (large velocity gradient or LVG): the sophisticated LVG code calculates the best density, temperature, and abundance to match the observations (page 127).

The results of my analysis are summarized in the following sections. The properties of the *associations* of the GMCs in the four H II regions are discussed first: these results are followed by a discussion of the properties of the *individual* GMCs in NGC 5461.

5.1 Conclusions about the Molecular Associations in M101

NGC 5461 is the most studied region in this thesis. The range of the molecular mass for the association of GMCs in NGC 5461 is calculated to be $(34 - 120) \times 10^7 \mathcal{M}_{\odot}$. The higher value in the range comes from the LTE analysis while the lower value comes from the empirical method using the interferometric data of NGC 5461. The lower value is questionable. First, the metallicity in M101 is significantly lower than the solar metallicity, and the X factor depends on the metallicity; therefore, the real X factor might be two or three times *larger* than what is used on page 120, and the empirical method may have underestimated the mass by a similar factor. Furthermore, the interferometric data provide the lower limit of the range because the flux from extended low-level emission is typically lost in an interferometer.

The molecular mass of the NGC 5461 association of GMCs is accompanied by a few times as much atomic mass. The fairly large ratio of atomic to molecular gas can be attributed either to slow formation of GMCs from the original atomic clouds, or to efficient dissociation of the GMCs to atomic gas. Both mechanisms remain possible because it is not clear yet in which region star-formation started first.

NGC 5462, another giant H II region near NGC 5461, has its peak CO emission $12''$ (or 430 pc) from the centre of the optical image of the H II region; the molecular mass of NGC 5462 obtained from both methods (LTE and the empirical method) is

three times less than that of NGC 5461. The stars that formed from this association are probably responsible for a superbubble seen in atomic maps (page 24).

It was not possible to detect molecular gas at the 9 mK level toward NGC 5471 with the JCMT despite the fact that NGC 5471 is a very bright giant H II region. CO emission can be detected with the NRAO 12-meter telescope, which observed a larger area, but the emission was weaker than expected. The weakness of the CO emission is interpreted as an indication that there is less molecular gas in NGC 5471. There is, however, a strong presence of atomic hydrogen in the vicinity of the region, which could indicate either the atomic gas has not converted to molecular gas yet, or the GMCs that *did* form were efficiently dissociated to atomic gas. Since NGC 5471 has a slightly smaller star-forming efficiency than NGC 5461, it is tempting to assume that NGC 5471 has not converted much of its atomic gas to molecular gas yet. Perhaps these giant H II regions are very young.

For both NGC 5461 and NGC 5471, the total gas mass can be extrapolated from the mass of the dust, which in turn can be estimated from IRAS measurements (see page 164). The estimates of the total gas mass from the dust are consistent with the sum of the molecular, ionized, and atomic masses.

Having summarized the conclusions on the giant H II regions, I now discuss the properties of H660. This normal H II region is much smaller in size than the giant H II regions, so the mass that is included in the JCMT beam probably includes contributions from other regions, and that is the reason why the mass of the normal H II region appears to be comparable to the mass of NGC 5461. Reinforcing this

conclusion. the ($^{13}\text{CO}/^{12}\text{CO}$) ratio for H660 is much less than that for NGC 5461: the density of the molecular gas associated with the giant H II region is larger than that in H660 according to the LVG model. Also, the gas in the normal H II region is probably cooler than the gas associated with the giant H II region.

5.2 Conclusions about the GMCs in NGC 5461

Now that the conclusions for the associations of GMCs have been completed, I summarize the results for the individual GMCs in NGC 5461—the only H II region with strong enough emission to be detected with the Owens Valley millimeter array. Some of the results depend on whether the GMCs have been resolved with the high-resolution data. Two reasons to accept that the clouds have been resolved are (i) the resolution of the Owens Valley millimeter array is comparable to the size of single large GMCs in our Galaxy, and (ii) the masses resulting from methods that do depend on the size of the source agree (within their uncertainties) with the masses resulting from methods that do not depend on the size of the GMC (see page 144).

The molecular gas of NGC 5461, according to the LVG analysis, has small (a few pc), warm (60 K) clumps embedded in large (several tens of pc), hot (250 K) GMCs. The masses of these large clouds cover a range of $(10 - 40) \times 10^5 \mathcal{M}_{\odot}$. Because the GMCs have such large masses, they probably contain significant quantities of dust, which would obscure visible light from the H II regions. This high extinction might explain why ionized hydrogen, observed in the optical part of the spectrum, is anticorrelated with the presence of detected GMCs.

The GMCs in NGC 5461 have masses comparable to their virial masses, which depend on the size and velocity dispersion of each cloud (see page 154). Therefore, these GMCs share a characteristic with those in the Milky Way: they are gravitationally bound.

Despite this similarity, the typical masses of the GMCs in NGC 5461 are an order of magnitude larger than the masses of the GMCs in the Milky Way. The large masses observed toward the clouds in NGC 5461 reinforce the hypothesis that *giant H II regions in M101 are so much brighter than the H II regions in our Galaxy because of the different properties of the natal clouds in M101.* In particular, the large number of bright O and B stars necessary to illuminate the giant H II regions can be produced by massive clouds in NGC 5461: Williams and McKee (1997) suggest that GMCs with masses greater than $10^6 \mathcal{M}_{\odot}$ will definitely produce an O9.5 star. Therefore, this thesis produces evidence that the mass of the GMC—not the star-forming efficiency of the gas—is the key to the formation of giant H II regions in M101.

Another important difference between the NGC 5461 GMCs and those seen in the Milky Way is their size:line-width relationship, which relates the size of the cloud to the velocity dispersion inferred from the line-widths. The GMCs in NGC 5461 have considerably larger sizes than expected given their small velocity dispersion. The sizes observed in M101 are between the small sizes observed in the Galaxy and the large sizes observed in M51, a grand-design spiral galaxy. This size:line-width relationship suggests that *the GMCs in M101 (and M51) form from collisions of smaller clouds.*

5.3 Future Directions

One of the current unresolved issues in star-formation theories is the mechanism for the formation of GMCs (Rand, 1993; Blitz, 1993). The observations presented in this thesis indicate that, for the case of the GMCs in NGC 5461, collisions of smaller clouds are important in the formation of the observed larger clouds. Since our understanding of the formation of GMCs is still in a state of flux, an attempt to incorporate the extreme cases of the massive GMCs in M101 will prove a challenge to future theoretical models.

Another theoretical issue that would assist the interpretation of observations is a prediction of the changes in the properties of the molecular gas as a result of star-formation. In other words, is it possible to predict the properties of the gas *after stars have formed in the cloud* based on a set of properties of the *pre-natal* GMC? When this theoretical problem is answered, then it will be easier to address the issue of whether the stars *change* the properties of the clouds, or the stars formed *because* the properties of the initial cloud were different.

The theoretical work obviously needs clues from observations. Because of the interesting nature of the giant H II regions in M101, future studies should attempt to improve and expand some of the suggestive observations presented in this work. For example, SCUBA can now be used to observe the properties of the dust in the H II regions more accurately (page 166).

Most of the observations obtained for this thesis, however, were reaching the sensitivity limits of the instruments used; with the current generation of instruments,

the improvement of the observations would be difficult. One possible exception is NGC 5462: it would be worthwhile to observe the CO emission from this giant H II region with the Owens Valley millimeter array again—this time pointing at the peak of the emission. If NGC 5462 is not detected even when the array is pointed directly at the peak of the CO emission, then one would conclude that the molecular component of NGC 5462 is indeed different from that of the nearby NGC 5461. If the CO is detected, then there will be more GMCs to analyze and improve the statistics of the GMCs in the M101 galaxy. In addition to NGC 5462, one might attempt to detect CO emission from the giant H II regions of M101 that were not observed, namely NGC 5447 and NGC 5455.

Detections of these fainter giant H II regions will be a challenge; however, the new generation of millimeter arrays (Brown, 1997) will have the necessary sensitivity to detect all the giant H II regions in M101 and the necessary resolution ($0''.1$ or 4 pc at the distance of M101) to observe the GMCs in galaxies within 50 Mpc of the Milky Way. Eventually it will be possible to observe weaker transitions of CO, such as $^{13}\text{CO } J = 3 \rightarrow 2$, which would be useful in further constraining the properties of the gas with the LVG analysis. The detailed study of GMCs in our own Galaxy and other galaxies will be greatly enhanced with the new instruments. Hopefully, these enhancements in technology will complement new theories of star-formation that can explain how GMCs form—even in the case of M101.

Appendix A

How to Calibrate Emission Line Observations

Since this thesis is based to a large extent on emission line data, it seems appropriate to include a detailed analysis of the method used to calibrate my observations. One quick survey of the literature is enough to conclude that there is no single, all-purpose analysis: different authors use different definitions; therefore, it is best to state explicitly the method used. This analysis shows the relationship between the physical temperature of the source and the observed temperature.

One of the main physical properties astronomers wish to determine is the *kinetic temperature* of the source, T_K : the standard measure of the source's physical temperature. If an unshocked, single fluid gas consists of molecules whose velocity distribution is Maxwellian, then the average velocity of the molecules between

collisions. $\langle v \rangle$, is (Lang, 1980)

$$\langle v \rangle = \left[\frac{8k T_K}{\pi \mu} \right]^{1/2} \quad (\text{A.1})$$

where k is the Boltzmann constant, and μ is the reduced mass of the molecule. Therefore, the kinetic temperature increases as the average velocity of the molecules increases.

In order to make the next step in the sequence of temperature definitions, one introduces the concept of local thermodynamic equilibrium (LTE). If the gas is in LTE, then the kinetic temperature is equal¹ to the *excitation temperature* of the source, T_{ex} , which is defined from the Boltzmann law [equation 3.8 in section 3.2]. Boltzmann's law indicates that as the excitation temperature rises, the higher energy states become more populated. The connection between the excitation temperature and the kinetic temperature is important because the strength of the intensities of the observed emission lines depend on the excitation temperature.

In addition to the above temperatures, it is customary to introduce the *black body brightness temperature*, T_B : the temperature of an imaginary black body² that would emit the same intensity as that observed, B_ν . The intensity emitted by a

¹The excitation temperature is not always equal to the kinetic temperature. When there is subthermal excitation, the excitation temperature is smaller than the kinetic temperature. In the opposite case, that is, the excitation temperature is larger than the kinetic temperature, the emission is due to some stimulated process such as that observed toward masers.

²What is interesting about this definition is that the observed source need not be—and usually is not—a black body.

black body is given by Planck's law, which in terms of frequency is

$$B_\nu = \frac{2h\nu^3}{c^2} \frac{1}{e^{h\nu/kT_B} - 1}. \quad (\text{A.2})$$

The only reason I introduce this quantity is that some authors use interchangeably the brightness temperature and the *radiation temperature*, T_R : I separate the two quantities and explain the reason for this confusion. Planck's law can be approximated by the Rayleigh-Jeans law for $h\nu \ll kT_B$ (Rohlfs, 1986):

$$B_\nu \approx \frac{2kT_B\nu^2}{c^2}. \quad (\text{A.3})$$

Therefore, for relatively low frequencies ($\nu \leq 10$ GHz or, equivalently $\lambda \geq 3$ cm) or high temperatures ($T_B \gg h\nu/k$), equation (A.3) can be used interchangeably with (A.2). This approximation is very convenient because the intensity at a particular frequency can be expressed simply in terms of a temperature multiplied by a constant.

In the millimeter-submillimeter part of the spectrum, however, the assumption necessary to use the Rayleigh-Jeans approximation is not valid. In the case of the CO $J = 2 \rightarrow 1$ transition, for example, the appropriate condition for the Rayleigh-Jeans law is $T_B \gg h\nu/k = 10.6$ K, which in general is not true for molecular gas. Therefore, since equation (A.3) is so convenient, the radiation temperature, T_R , is defined to satisfy the equation even for high frequencies (Lang, 1980):

$$B_\nu \equiv \frac{2kT_R\nu^2}{c^2}. \quad (\text{A.4})$$

Now it is clear why there has been some confusion between the radiation temperature and brightness temperature. For low frequencies, they are equal: for high frequencies, they are not.³

The radiation temperature is the source's temperature that a perfect antenna would measure at the top of the Earth's atmosphere. But this definition does not take into account factors which may arise in the measuring process. One of the physical quantities that can be defined is the power in a given frequency band, w , that is observed in a real telescope. The *antenna temperature*, T_A , is defined as the temperature of a fictitious resistor that would produce the same power per unit bandwidth as that observed:

$$w = k T_A \quad (\text{A.6})$$

where k is the Boltzmann constant.

The antenna temperature is affected by the source structure, the antenna behaviour, and the atmosphere. The source is not necessarily uniform: the intensity of the source, B_ν , is in general a function of a solid angle, Ψ . In addition to the source structure, the measured temperature depends on the antenna characteristics and how the beam couples with the source. In particular, one characterizes the

³In addition to the definition I have already presented, I should point out for completeness that Lang (1980) suggests an alternate definition for radiation temperature based on the relationship of the Einstein probability coefficients:

$$A_{mn} = I_\nu B_{mn} \frac{h\nu}{kT_R} \quad (\text{A.5})$$

where A_{mn} and B_{mn} are the Einstein probability coefficients, and I_ν is the intensity of the radiation. For the rest of this analysis, I assume the definition of the radiation temperature from the Rayleigh-Jeans law regardless of wavelength (A.4).

antenna response by the antenna power pattern, $P(\Omega)$, where Ω is a solid angle. Furthermore, it is customary to define a normalized antenna power pattern $P_n(\Omega)$, so that $P_n(0) = 1$.

The received power per unit bandwidth depends on the convolution of the intensity of the source and the antenna power pattern (Kraus, 1986); it also depends on the atmosphere, which reduces the signal from the source. The percentage of radiation that penetrates the atmosphere depends on the airmass, A , and the atmospheric optical depth, τ_a , at the wavelength of interest. Furthermore, the antenna transforms some of the signal it receives into heat. These losses are due to the ohmic heating of the antenna, and to take them into account, Kutner and Ulich (1981) define the radiation efficiency, η_r , as the ratio of the total power available at the receiver to the total power incident on the antenna. Therefore, one has

$$w = \frac{1}{2} \eta_r e^{-\tau_a A} A_e \iint_{\Omega_s} P_n(\Psi - \Omega) B_\nu(\Psi) d\Psi = kT_A \quad (\text{A.7})$$

where the $\frac{1}{2}$ factor in equation (A.7) is to indicate that only one polarization is measured. Ω_s is the solid angle subtended by the source, and A_e is the effective aperture of the antenna. The latter quantity is defined as the aperture of a perfectly surfaced antenna with no blockage that would measure the same signal as observed:

$$A_e = \eta_a A_g, \quad (\text{A.8})$$

where η_a is the aperture efficiency (Kraus, 1986), and A_g is the geometric aperture (the actual area of the aperture). For example, the James Clerk Maxwell Telescope

(JCMT) has $\eta_a = 0.63$ at 230 GHz (Matthews. 1996).

Using the definition of radiation temperature (A.4) and including its explicit dependence on direction. I can write equation (A.7) as follows (Kraus. 1986):

$$T_A = \eta_r e^{-\tau_a A} \frac{A_e}{\lambda^2} \iint_{\Omega_s} P_n(\Psi - \Omega) T_R(\Psi) d\Psi. \quad (\text{A.9})$$

where λ is the wavelength of the radiation. For a given wavelength, the product of the effective aperture and the solid angle that contains the beam of the telescope is constant (Kraus. 1986):

$$\frac{A_e}{\lambda^2} = \frac{1}{\Omega_A}$$

where Ω_A is the solid angle that contains the beam and is given by

$$\Omega_A = \iint_{4\pi} P_n(\Omega) d\Omega.$$

Therefore, the antenna temperature is (Kraus. 1986)

$$T_A = \eta_r e^{-\tau_a A} \frac{1}{\Omega_A} \iint_{\Omega_s} P_n(\Psi - \Omega) T_R(\Psi) d\Psi. \quad (\text{A.10})$$

Suppose that the radiation temperature is uniform across the source, i.e. $T_R(\Psi) = \bar{T}_R$. To define the efficiencies necessary for the calibration, one needs the quantity Ω_d , which is defined by Kutner and Ulich (Kutner and Ulich. 1981) based on the idea that one can “divide the antenna pattern into two zones, one involving the normal diffraction pattern and the other involving spillover (both forward and rearward) as

well as scattering from the feed support legs and other structures. . . . If [one says] that all of the power within a solid angle Ω_d is part of the diffraction pattern, then everything outside Ω_d is considered spillover and scattering." Therefore, equation (A.10) can be written as follows:

$$T_A = \eta_r e^{-\tau_a A} \bar{T}_R \frac{\iint_{\Omega_s} P_n(\Psi - \Omega) d\Psi}{\iint_{\Omega_d} P_n(\Omega) d\Omega} \frac{\iint_{\Omega_d} P_n(\Omega) d\Omega}{\iint_{4\pi} P_n(\Omega) d\Omega} \quad (\text{A.11})$$

where

$$\frac{\iint_{\Omega_d} P_n(\Omega) d\Omega}{\iint_{4\pi} P_n(\Omega) d\Omega} = \frac{\iint_{\Omega_d} P_n(\Omega) d\Omega}{\iint_{2\pi} P_n(\Omega) d\Omega} \frac{\iint_{2\pi} P_n(\Omega) d\Omega}{\iint_{4\pi} P_n(\Omega) d\Omega} = \eta_{fss} \eta_{rss}.$$

Here η_{fss} is the efficiency of forward scattering and spillover, whereas the η_{rss} is the backward scattering and spillover efficiency. These definitions can be used safely because the sources of interest, associations of GMCs at the distance of M101, are very small compared to Ω_d , which is typically 1 - 5' for NRAO (Kutner and Ulich) and 0'.25 for the JCMT at $^{12}\text{CO } J = 3 \rightarrow 2$.

If the efficiencies η_{fss} and η_{rss} are replaced in equation (A.11), I obtain:

$$T_A = \eta_r \eta_{fss} \eta_{rss} e^{-\tau_a A} \bar{T}_R \frac{\iint_{\Omega_s} P_n(\Psi - \Omega) d\Psi}{\iint_{\Omega_d} P_n(\Omega) d\Omega}. \quad (\text{A.12})$$

The ratio of the integrals in the previous equation is defined as the coupling efficiency, η_c , which is the efficiency that the antenna diffraction pattern couples to the source (Kutner and Ulich, 1981):

$$\eta_c = \frac{\iint_{\Omega_s} P_n(\Psi - \Omega) d\Psi}{\iint_{\Omega_d} P_n(\Omega) d\Omega} \quad (\text{A.13})$$

If the ratio of integrals is replaced with the coupling efficiency, then equation (A.12) becomes

$$T_A = \eta_r \eta_{fss} \eta_{rss} \eta_c e^{-\tau_a A} \bar{T}_R. \quad (\text{A.14})$$

With equation (A.14), the discussion of the connection between the antenna temperature and the radiation temperature is complete. Now it is necessary to bridge theoretical and observed quantities. This bridging is done by introducing some corrections for the observed antenna temperature. During the measuring process, the antenna temperature can be corrected for the atmosphere's effects, the ohmic losses at the telescope, and for rearward spillover and scattering (e.g., at the JCMT). Therefore, a corrected antenna temperature, T_A^* , can be defined:

$$T_A^* = \frac{T_A e^{\tau_a A}}{\eta_r \eta_{rss}}. \quad (\text{A.15})$$

Some telescopes (such as the NRAO 12-meter Telescope), however, use T_R^* , which is defined as the radiation temperature corrected for everything except the actual

coupling of the source of the antenna diffraction pattern⁴ (Kutner and Ulich) :

$$T_A^* = T_R^* \eta_{fss}. \quad (\text{A.16})$$

If the source is uniform ($\bar{T}_R = T_R$), and equations (A.15) and (A.16) are combined in equation (A.14), then

$$T_R = \frac{T_A^*}{\eta_c \eta_{fss}} = \frac{T_R^*}{\eta_c}. \quad (\text{A.17})$$

The goal of relating the observed quantity, T_A^* , with the physically interesting temperature, T_R , has been achieved. Equation (A.17) is crucial to obtain quantitative results from emission line observations.

⁴Another temperature scale is the main beam temperature, T_{MB} —the radiation temperature for a source that uniformly fills the main beam. The main beam temperature is related to the radiation temperature through this equation

$$T_R = T_{MB} \frac{\eta_c(mb)}{\eta_c},$$

where $\eta_c(mb)$ is the coupling efficiency of the main beam with the antenna diffraction pattern. This coupling efficiency is not the same with the main beam efficiency, η_{mb} ; the two efficiencies are connected by the following equation:

$$\eta_{mb} = \eta_c(mb) \eta_{fss} \eta_{rss}.$$

For the NRAO 12-meter Telescope, the $\eta_c(mb) = 0.63$ (Kutner, private communication).

Bibliography

- Allen, R., Le Bourlot, J., Lequeux, J., Pineau des Forets, G., and Roueff, E.: 1995, *Astrophys. J.* **444**, 157
- Allen, R. J. and Goss, W.: 1979, *Astron. Astrophys. Suppl. Ser.* **36**, 135
- Blitz, L. Israel, F. P., Neugebauer, G., Gatley, I., Lee, T. J., and Beattie, D. H.: 1981, *Astrophys. J.* **249**, 76
- Blitz, L.: 1993, in J. I. L. Eugene H. Levy (ed.), *Protostars and Planets III*, Space Science Series, p. 125. The University of Arizona Press, Tucson
- Blitz, L. and Shu, F. H.: 1980, *Astrophys. J.* **238**, 148
- Blitz, L. and Thaddeus, P.: 1980, *Astrophys. J.* **241**, 676
- Bohm-Vitense, E.: 1989, *Introduction to Stellar Astrophysics—Stellar Atmospheres*, Cambridge University Press, Cambridge
- Bowers, R. L. and Deeming, T.: 1984, *Astrophysics*, Jones and Bartlett Publishers, Inc., Boston
- Braun, R.: 1995, *Astron. Astrophys. Suppl. Ser.* **114**, 409
- Braun, R.: 1997, *Astrophys. J.* **484**, 637
- Bresolin, F., Kennicutt, Jr., R. C., and Stetson, P. B.: 1996, *Astron. J.* **112**, 1009

- Bronfman, L., Cohen, R. S., Alvarez, H., May, J., and Thaddeus, P.: 1988. *Astrophys. J.* **324**, 248
- Brown, R. L.: 1997. in W. B. Latter, S. J. E. Radford, P. R. Jewell, J. G. Mangum, and J. Bally (eds.), *CO: Twenty-Five Years of Millimeter-wave Spectroscopy. Proceedings of the 170th Symposium of the IAU*, p. 247
- Chantry, G. W.: 1979, *Modern Aspects of Microwave Spectroscopy*, Academic Press Inc., London
- Clemens, D. P., Sanders, D. B., and Scoville, N. Z.: 1988. *Astrophys. J.* **327**, 139
- Cohen, R. S., Dame, T. M., Garay, G., Montani, J., Rubio, M., and Thaddeus, P.: 1988. *Astrophys. J., Lett.* **331**, 95
- Cohen-Tannoudji, C., Diu, B., and Laloe, F.: 1977. *Quantum Mechanics*, Wiley, New York
- Cook, K. H., Aaronson, M., and Illingworth, G.: 1986. *Astrophys. J., Lett.* **301**, 45
- Dame, T. M., Elmegreen, B. G., Cohen, R. S., and Thaddeus, P.: 1986. *Astrophys. J.* **305**, 892
- Dame, T. M., Koper, E., Israel, F., and Thaddeus, P.: 1991. in F. Combes and F. Casoli (eds.), *Dynamics of Galaxies and their Molecular Distributions Proceedings of the 146th Symposium of the International Astronomical Union*, p. 23. Kluwer Academic Publishers, Dordrecht, The Netherlands
- de Vaucouleurs, G.: 1993. *Astrophys. J.* **415**, 10
- Digel, S. W., Hunter, S. D., Mukherjee, R., de Geus, E. J., Grenier, I. A., Heithausen, A., Kanbach, G., and Thaddeus, P.: 1997, in W. B. Latter, S. J. E. Radford, P. R. Jewell, J. G. Mangum, and J. Bally (eds.), *CO: Twenty-Five*

- Years of Millimeter-wave Spectroscopy. Proceedings of the 170th Symposium of the IAU.* p. 22
- Efron, B. and Tibshirani, R. J.: 1993. *An Introduction to the Bootstrap*. Chapman & Hall, New York
- Evans, I. N.: 1986. *Astrophys. J.* **309**, 544
- Fich, M. and Hodge, P.: 1991. *Astrophys. J., Lett.* **374**, 17
- Flower, D. R. and Launay, J. M.: 1985. *Mon. Not. R. Astron. Soc.* **214**, 271
- Garay, G., Rubio, M., Ramirez, S., Johansson, L. E. B., and Thaddeus, P.: 1993. *Astron. Astrophys.* **274**, 743
- Garnett, D. R. and Kennicutt, Jr., R. C.: 1994. *Astrophys. J.* **426**, 123
- Giannakopoulou, J., Mitchell, G. F., Hasegawa, T. I., Matthews, H. E., and Mailard, J.-P.: 1997. *Astrophys. J.* **487**, 346
- Goldreich, P. and Kwan, J.: 1974. *Astrophys. J.* **189**, 441
- Habing, H. J. and Israel, F. P.: 1979. *Annu. Rev. Astron. Astrophys.* **17**, 345
- Harris, S.: 1980. in P. M. Solomon (ed.), *Giant Molecular Clouds in Galaxy: Proceedings of the Third Gregynog Astrophysics Workshop, Cardiff, Wales, August 1977*, p. 201
- Hasegawa, T. I., Rogers, C., and Hayashi, S. S.: 1991. *Astrophys. J.* **374**, 177
- Hodge, P. W., Gurwell, M., Goldader, J. D., and Kennicutt, Jr., R. C.: 1990. *Astrophys. J., Suppl. Ser.* **73**, 661
- Hodge, P. W. and Kennicutt, J. R. C.: 1983. *Astron. J.* **88**, 296
- Huchtmeier, W. K. and Witzer, A.: 1979. *Astron. Astrophys.* **74**, 138
- Hummer, D. G. and Rybicki, G.: 1971. *Annu. Rev. Astron. Astrophys.* **9**, 237

- Humphreys, R. M. and Strom, S. E.: 1983. *Astrophys. J.* **264**, 458
- Israel, F. P.: 1980. *Astron. J.* **85**, 1612
- Israel, F. P., Goss, W. M., and Allen, R. J.: 1975. *Astron. Astrophys.* **40**, 421
- Jefferies, J. T.: 1968. *Spectral Line Formation*. Blaisdell Publishing Company, Waltham, Massachusetts
- Johansson, L. E. B.: 1991, in F. Combes and F. Casoli (eds.), *Dynamics of Galaxies and their Molecular Distributions Proceedings of the 146th Symposium of the International Astronomical Union*, p. 1. Kluwer Academic Publishers, Dordrecht, The Netherlands
- Kamphuis, J., Sancisi, R., and van der Hulst, T.: 1991. *Astron. Astrophys.* **244**, L29
- Kamphuis, J. J.: 1993. *Ph.D. thesis*, Rijksuniversiteit Groningen
- Kelson, D. D., Illingworth, G. D., Freedman, W. F., Graham, J. A., R., H., Madore, B. F., Saha, A., Stetson, P. B., Kennicutt, Jr., R. C., Mould, J. R., Hughes, S. M., Ferrarese, L., Phelps, R., Turner, A., Cook, K. H., Ford, H., Hoessel, J. G., and Huchra, J.: 1996. *Astrophys. J.* **463**, 26
- Kenney, J. D. P., Scoville, N. Z., and Wilson, C. D.: 1991. *Astrophys. J.* **366**, 432
- Kennicutt, Jr., R. C.: 1984. *Astrophys. J.* **287**, 116
- Kennicutt, Jr., R. C.: 1988. *Astrophys. J.* **334**, 144
- Kraus, J. D.: 1986. *Radio Astronomy*, Cygnus-Quasar Books, Powell, Ohio, 2nd edition
- Kutner, M. L. and Ulich, B. L.: 1981, *Astrophys. J.* **250**, 341
- Lada, C. J. and Fich, M.: 1996. *Astrophys. J.* **459**, 638

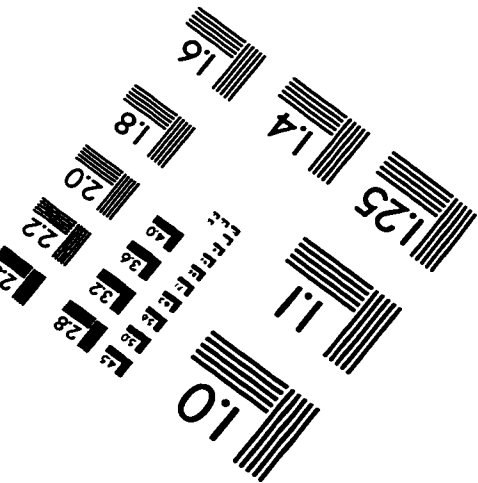
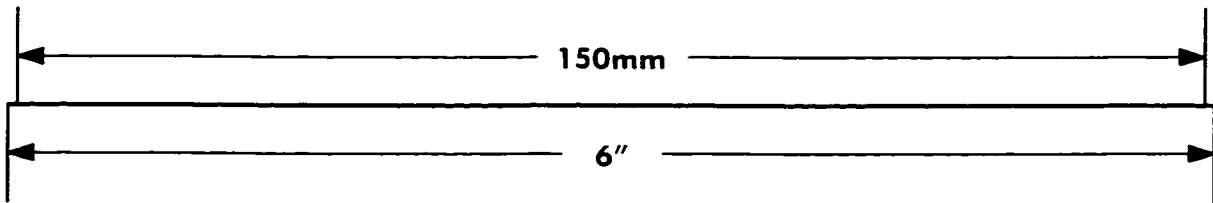
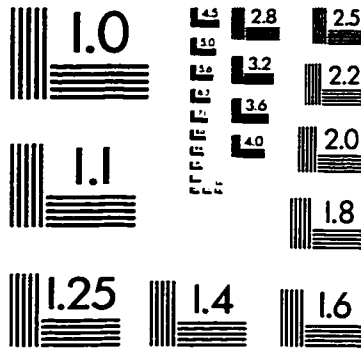
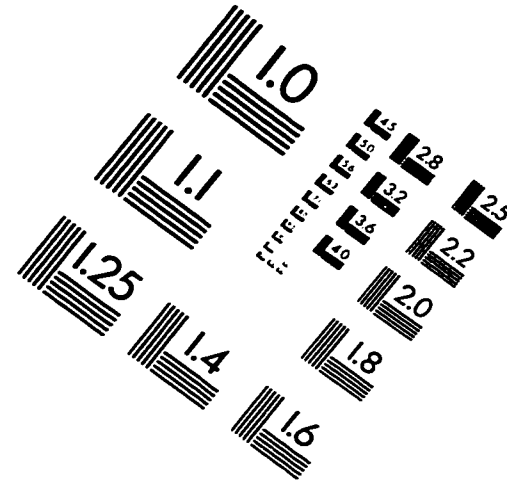
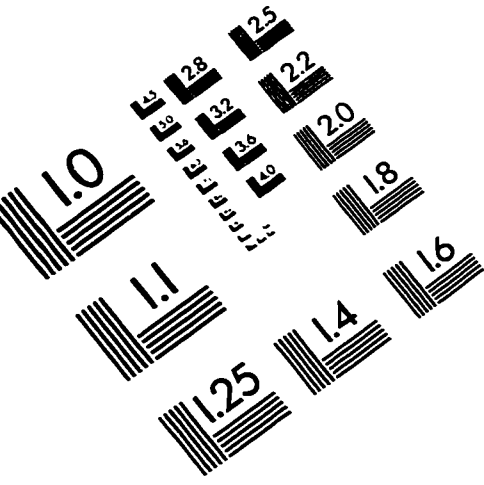
- Lang, K. R.: 1980. *Astrophysical Formulæ*. Springer-Verlag, Heidelberg, second edition
- Langer, W. D. and Penzias, A. A.: 1990. *Astrophys. J.* **357**, 477
- Larson, R. B.: 1981. *Mon. Not. R. Astron. Soc.* **194**, 809
- Lee, S.-W.: 1992. *Master's thesis*, Saint Mary's University
- Maloney, P. and Black, J. H.: 1988. *Astrophys. J.* **325**, 389
- Matteucci, F.: 1986. *Publ. Astron. Soc. Pac.* **98**, 973
- Matthews, H. E.: 1996. *The James Clerk Maxwell Telescope: A Guide for the Prospective User*. Technical report, Hilo, Hawaii
- McCall, M. L., Rybski, P. M., and Shields, G. A.: 1985. *Astrophys. J., Suppl. Ser.* **57**, 1
- McLaughlin, D. E. and Pudritz, R. E.: 1996. *Astrophys. J.* **469**, 194
- Mihalas, D. and Binney, J.: 1981. *Galactic Astronomy*. W. H. Freeman and Company, New York, second edition
- Mitchell, G. F., Lee, S.-W., Maillard, J.-P., Matthews, H., Hasegawa, T. I., and Harris, A. I.: 1995. *Astrophys. J.* **438**, 794
- Pagel, B. E. J.: 1986. *Publ. Astron. Soc. Pac.* **98**, 1009
- Petitpas, G. R. and Wilson, C. D.: 1998. *Astrophys. J.* **496**, 226
- Pierce, M. J.: 1994. *Astrophys. J.* **430**, 53
- Poglitsch, A., Krabbe, A., Madden, S. C., Nikola, T., Geis, N., Johansson, L. E. B., Stacey, G. J., and Sternberg, A.: 1995. *Astrophys. J.* **454**, 293
- Rand, R. J.: 1993. *Astrophys. J.* **404**, 593
- Rand, R. J. and Kulkarni, S. R.: 1990. *Astrophys. J., Lett.* **349**, 43

- Rayo, J. F., Peimbert, M., and Torres-Peimbert, S.: 1982. *Astrophys. J.* **255**, 1
- Rohlfs, K.: 1986. *Tools of Radio Astronomy*, Springer-Verlag, Berlin: New York
- Rosa, M. R. and Benvenuti, P.: 1994. *Astron. Astrophys.* **291**, 1
- Rubio, M.: 1991. in F. Combes and F. Casoli (eds.), *Dynamics of Galaxies and their Molecular Distributions Proceedings of the 146th Symposium of the International Astronomical Union*, p. 9. Kluwer Academic Publishers, Dordrecht, The Netherlands
- Rubio, M.: 1997. in W. B. Latter, S. J. E. Radford, P. R. Jewell, J. G. Mangum, and J. Bally (eds.), *CO: Twenty-Five Years of Millimeter-wave Spectroscopy. Proceedings of the 170th Symposium of the IAU*, p. 265
- Rubio, M., Garay, G., Montani, J., and Thaddeus, P.: 1991. *Astrophys. J.* **368**, 173
- Rubio, M., Lequeux, J., and Boulanger, F.: 1993a. *Astron. Astrophys.* **271**, 9
- Rubio, M., Lequeux, J., Boulanger, F., Booth, R. S., Garay, G., de Graauw, T., Israel, F., Johansson, L. E. B., Kutner, M., and L.-A., N.: 1993b. *Astron. Astrophys.* **271**, 1
- Sandage, A.: 1983. *Astron. J.* **88**, 1569
- Sandage, A. and Tammann, G. A.: 1974. *Astrophys. J.* **190**, 525
- Sandage, A. and Tammann, G. A.: 1976. *Astrophys. J.* **210**, 7
- Sanders, D. B., Scoville, N. Z., and Solomon, P. M.: 1985. *Astrophys. J.* **289**, 373
- Schmidt, B. P., Kirshner, R. P., and Eastman, R. G.: 1992, *Astrophys. J.* **395**, 366
- Scoville, N. and Sanders, D. B.: 1987, in H. D. J. and H. A. Thronson, Jr. (eds.), *Interstellar Processes*, Vol. 134, pp 21-50

- Scoville, N. Z. and Solomon, P. M.: 1974. *Astrophys. J., Lett.* **187**, 67
- Scoville, N. Z., Yun, M. S., Clemens, D. P., Sanders, D. B., and Waller, W. H.:
1987. *Astrophys. J., Suppl. Ser.* **63**, 821
- Shaver, P. A., McGee, R. X., Newton, L. M., Danks, A. C., and Pottasch, S. R.:
1983. *Mon. Not. R. Astron. Soc.* **204**, 53
- Shields, G. A.: 1990. *Annu. Rev. Astron. Astrophys.* **28**, 525
- Skillman, E. D.: 1984. *Ph.D. thesis*, University of Washington
- Skillman, E. D. and Balick, B.: 1984. *Astrophys. J.* **280**, 580
- Snell, R. L.: 1981. *Astrophys. J., Suppl. Ser.* **45**, 121
- Solomon, P. M., Barrett, J., Sanders, D. B., and de Zafra, R.: 1983. *Astrophys. J., Lett.* **266**, 103
- Solomon, P. M., Rivolo, A. R., Barrett, J., and Yahil, A.: 1987. *Astrophys. J.* **319**, 730
- Spitzer, L. J.: 1978. *Physical Processes in the Interstellar Medium*, Wiley, New York
- Stark, A. A. and Blitz, L.: 1978. *Astrophys. J., Lett.* **225**, 15
- Thornley, M. D. and Wilson, C. D.: 1994. *Astrophys. J.* **421**, 458
- Torres-Peimbert, S., Peimbert, M., and Fierro, J.: 1989. *Astrophys. J.* **345**, 186
- Vogel, S. N., Kulkarni, S. R., and Scoville, N. Z.: 1988. *Nature* **334**, 402
- Wang, Y., Jaffe, D. T., Evans, N. J. I., Hayashi, M., Tatematsu, K., and Zhou, S.:
1993. *Astrophys. J.* **419**, 707
- Welch, G. A., Mitchell, G. F., and Yi, S.: 1996. *Astrophys. J.* **470**, 781
- White, R. E.: 1977. *Astrophys. J.* **211**, 744

- Williams, J. P. and McKee, C. F.: 1997. *Astrophys. J.* **476**, 166
- Wilson, C. D.: 1995. *Astrophys. J., Lett.* **448**, 97
- Wilson, C. D. and Matthews, B. C.: 1996. *Astrophys. J.* **455**, 125
- Wilson, C. D. and Rudolph, A. L.: 1993. *Astrophys. J.* **406**, 477
- Wilson, C. D. and Scoville, N.: 1989. *Astrophys. J.* **347**, 743
- Wilson, C. D. and Scoville, N.: 1990. *Astrophys. J.* **363**, 435
- Wilson, C. D. and Scoville, N.: 1992. *Astrophys. J.* **385**, 512
- Wilson, C. D., Scoville, N., Freedman, W. L., Madore, B. F., and Sanders, D. B.:
1988. *Astrophys. J.* **333**, 611
- Wilson, C. D., Walker, C. E., and Thornley, M. D.: 1997. *Astrophys. J.* **483**, 210
- Young, J. S. and Scoville, N. Z.: 1991. *Annu. Rev. Astron. Astrophys.* **29**, 581

IMAGE EVALUATION TEST TARGET (QA-3)



APPLIED IMAGE, Inc
1653 East Main Street
Rochester, NY 14609 USA
Phone: 716/482-0300
Fax: 716/288-5989

© 1993, Applied Image, Inc., All Rights Reserved

